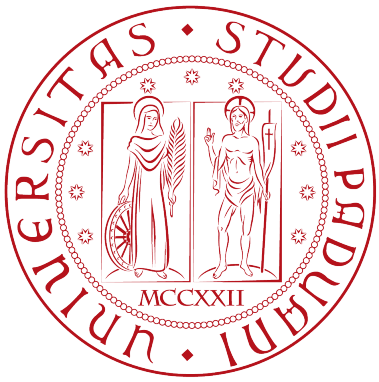


UNIVERSITÀ DEGLI STUDI DI PADOVA

DIPARTIMENTO DI SCIENZE CHIMICHE

**SCUOLA DI DOTTORATO IN SCIENZE MOLECOLARI**

**INDIRIZZO SCIENZE CHIMICHE**

**CICLO XXVIII**

# MOLECULAR DYNAMICS METHODS APPLIED TO FLEXIBLE MACROMOLECULES

**Direttore della Scuola:** Ch.mo Prof. Antonino Polimeno

**Coordinatore d'indirizzo:** Ch.mo Prof. Antonino Polimeno

**Supervisore**: Ch.mo Prof. Antonino Polimeno

**Dottorando:** Nicola Fortunati

# MOLECULAR DYNAMICS METHODS APPLIED TO FLEXIBLE MACROMOLECULES

Nicola Fortunati

Doctorate School in Molecular Sciences
Curriculum Chemical Sciences
Cycle XXVIII

February 2nd, 2016

**Abstract**

Cement-based materials, such as concrete or mortars, are usually considered materials with low technological level. Although they are the most employed human made materials in the world, others such as wood, plastics, metals and even stones are usually more valued in the everyday life: probably the fact that cement is cheap, readily available, common, and has been employed successfully for centuries, contributes to its low technology perception.

However, this vision is far from the reality: the cement paste is a complex multicomponent and heterogeneous composite system, with different structural features at different length scales. The mechanism in which the clinker in contact with water becomes a hardened paste comprises hundreds of chemical reactions and physical processes.

Understanding the molecular details of cement hydration processes is of fundamental importance due to the technological and economical impact of these materials. Several aspects need to be considered, and a realistic approach should be limited to a few specific features.

Many efforts have been devoted over the last 40 years to develop mathematical models for understanding and predicting highly complex cement hydration kinetics, microstructure development and the implications of these for the changing physical-chemical properties of cement paste and concrete. An accurate hydration simulation approach would enable scientists and engineers not only to predict the performance of concrete, but also to design new cementitious materials. Despite significant effort

and progress, the ability to perform such a complete simulation has not yet been developed, mainly because cement hydration is one of the more complex phenomena in engineering/materials science.

The main objective of this PhD thesis is to analyse the influence of superplasticizers on the microevolution of cement suspensions during early hydration based of Molecular Dynamics (MD) approaches. To this purpose we implemented a MD protocol for the study of the behavior of polycarboxylate-ether-based superplasticizers (PCEs) in the presence of selected cement surfaces, tricalcium aluminate ($C_3A$) and tricalcium silicate ($C_3S$), water molecules and calcium hydroxide.

The final goal of the project, which was carried in collaboration with the group of Prof. G. Artioli - *Università degli Studi di Padova*, *Dipartimento di Geoscienze*, was to clarify structure-properties relationships, in order to design new products with enhanced properties. In fact, the rheology of cement pastes can be controlled by the use of superplasticizers that, by adsorbing on the surfaces of cement particles, enhance their workability.

The protocol was made up of the following steps: i) building of the cement surfaces, ii) parameterization of force field, iii) setting of the simulation and evaluation of physical observables.

Some methodological knowledges acquired were employed on side-applications, for example the evaluation of electrostatic interactions of other organic molecules, in particular partial charges of amino acids (AA) and nonstandard amino acids (Non-AA), present in the human Connexin protein.

To be precise, following the earlier approach of Bayly et al [Bayly1993], we obtained the charge set by fitting to the electrostatic potentials of Non-AA calculated using ab-initio methods. This effort was carried out in collaboration with the group of F. Mammano - *Università degli Studi di Padova, Dipartimento di Fisica e Astronomia* [Zonta2014].

Finally, in a joint effort with Dott.ssa L. Orian, Dott. M. Torsello and P. Calligari, of my research group, simulate complete simulation was carried out of the Connexin 26 hemichannel (Cx26) behaviour in the presence of post-translational modifications (PTMs) and $Ca^{2+}$. The contribution to this joint project described in this thesis, was aimed to i) the analysis of the structure of the channel and ii) the preservation of salt bridges between Glu47, Arg75 and γ-Glu47, Arg75 in the presence/asbsence of $Ca^{2+}$.

Lastly, preliminary results based on a collaboration with Stazione Sperimentale del Vetro (SSV) of Murano (Ve) for the project: *"Computational methods for the modeling of equilibrium properties of glassy materials", is presented.* The goal of this work was the elaboration, optimization and validation of a model of the type of ideal solutions for the thermodynamic properties of glasses and the inclusion in integrated software platforms.

This work is organised as follows.

In chapter 1, a brief overview is presented of the atomistic simulation methods used during the Thesis, because several levels of theory were selected depending on their capabilities to solve punctual problems: *ab initio*, Molecular Mechanics, and Molecular Dynamics.

In chapter 2, an introduction to cement chemistry and the necessary basis is given in order to follow the results and discussions of the systems presented in this Thesis. It covers a description of clinker phases, superplasticizers, the hydration process, the cement paste structure and computational methods applied in cement research.

In chapter 3, the results of four MD simulations are discussed for a system consisting of PCE-(23-7-1), a comb-shaped polymer unit model superplasticizer of methyl-polyethylene glycole methacrylate and methacrylic acids (seven back bone units, one side-chain unit and twenty three polyethylene-oxide units in the side chain), the $C_3A$ and $C_3S$ surfaces, explicit molecules of water, $Ca^{2+}$ and $OH^-$ ions (pore solution): from the MD trajectories were calculated conformational properties.

In chapter 4, the results are discussed of partial charges parametrization of Non-AA, the structural channel analysis and salt-bridges analysis of Cx26 protein.

In chapter 5, the thermodynamic model is presented for calculating the composition of glasses, the interpolation for temperature dependence of thermodynamic properties and the validation of model with a simple binary oxide system $Na_2O$-$SiO_2$.

# MOLECULAR DYNAMICS METHODS APPLIED TO FLEXIBLE MACROMOLECULES

Nicola Fortunati

Scuola di Dottorato in Scienze Molecolari
Curriculum Scienze Chimiche
Ciclo XXVIII

2 Febbraio 2016

**Sommario**

Il cemento e i suoi derivati, come calcestruzzo e malte, sono generalmente considerati materiali a basso livello tecnologico. Pur essendo il materiale più prodotto e utilizzato al mondo, altri, come legno, plastica, metalli e anche le pietre sono considerati più importanti nella vita di tutti i giorni: probabilmente il fatto che il cemento è economico, comune, facilmente disponibile ed è stato impiegato con successo per secoli, contribuisce alla sua bassa percezione tecnologia.

Tuttavia, questa visione è lontana dalla realtà: la pasta di cemento è un sistema composito multicomponente eterogeneo e complesso; il meccanismo con cui clinker in contatto con l'acqua diventa una pasta indurita comprende centinaia di processi chimici e fisici.

La comprensione dei dettagli molecolari nel processo d'idratazione del cemento è di fondamentale importanza per l'impatto tecnologico ed economico di questi materiali. Molti aspetti devono essere considerati e un approccio realistico dovrebbe essere limitato a poche caratteristiche specifiche.

Molti sforzi sono stati fatti negli ultimi quarant'anni per sviluppare modelli matematici che consentono la comprensione e la previsione della complessa cinetica d'idratazione, lo sviluppo di microstrutture e le implicazioni nelle proprietà fisico-chimiche del calcestruzzo.

Un approccio accurato nella simulazione del processo d'idratazione consentirebbe a scienziati e ingegneri non solo di prevedere le prestazioni del calcestruzzo, ma anche per progettare nuovi materiali cementizi.

Nonostante i notevoli sforzi fatti e i progressi ottenuti, la capacità di effettuare una simulazione così completa non è stata ancora sviluppata, perché il processo d'idratazione è uno dei fenomeni più complessi nell'ingegneria/scienza dei materiali.
L'obiettivo principale della mia Tesi di Dottorato è l'analisi dell'influenza dei superfluidificanti sulla microevoluzione di sospensioni cementizie durante l'idratazione, usando metodi di Dinamica Molecolare (MD): abbiamo implementato un protocollo MD per studiare il comportamento dei superfluidificanti a basedi eteri policarbossilati (PCEs), in presenza di superfici selezionate cemento, alluminato tricalcico ($C_3A$) e silicato tricalcico ($C_3S$), molecole d'acqua e idrossido di calcio.
L'obiettivo finale del progetto, realizzato in collaborazione con il gruppo del Prof. G. Artioli - *Università degli Studi di Padova, Dipartimento di Geoscienze*, era quello di chiarire le relazioni struttura - proprietà per riuscire a progettare nuovi prodotti con caratteristiche avanzate: infatti, la reologia di paste di cemento può essere controllata mediante l'uso dei superfluidificanti che, legandosi sulle superfici delle particelle di cemento, ne migliorano la lavorabilità.
Il protocollo è costituito dalle seguenti fasi: i) costruzione delle superfici cementizie, ii) parametrizzazione del campo di forza, iii) impostazione della simulazione e valutazione delle osservabili fisiche.
Alcune conoscenze metodologiche acquisite sono impiegate con laterali applicazioni, per esempio la valutazione delle interazioni elettrostatiche di altre molecole organiche, in particolare le cariche parziali di amminoacidi (AA) e amminoacidi non standard (non-AA), presenti nella proteina umana Connessina: per essere precisi, seguendo l'approccio di Bayly [Bayly1993], abbiamo ottenuto il set di cariche dal fitting dei potenziali elettrostatici di Non-AA calcolati con metodi *ab-initio*. Questo lavoro è stato realizzato in collaborazione con il gruppo di F. Mammano - *Università degli Studi di Padova, Dipartimento di Fisica e Astronomia* [Zonta2014].
In collaborazione con la Dott.ssa L. Orian, Dott. M. Torsello e P. Calligari, del mio gruppo di ricerca, mediante Dinamica Molecolare abbiamo simulato la Connessina 26 emicanale (Cx26) in presenza di modificazioni post-traduzionali (PTM) e $Ca^{2+}$: il mio contributo, in sostanza, aveva lo scopo di analizzare i) la struttura del canale e ii) la conservazione dei ponti salini tra Glu47, Arg75 e γ-Glu47, Arg75 in presenza/assenza di $Ca^{2+}$all'interno del canale.
Infine, ho iniziato una collaborazione con la Stazione Sperimentale del Vetro (SSV) di Murano (Ve) in questo progetto: *"Metodi computazionali per la modellazione di*

*proprietà d'equilibrio dei materiali vetrosi"*. L'obiettivo di questo lavoro è stato l'elaborazione, l'ottimizzazione e validazione di un modello del tipo soluzioni ideali per il calcolo di proprietà termodinamiche del vetro e l'inclusione in piattaforme software integrate.

Fino ad ora, abbiamo ottenuto il calcolo della composizione dei vetri silicati considerando la dipendenza dalla temperatura della $\Delta_f G_X^o(T)$, termodinamicamente coerente, di ossidi elementari e misti all'interno del vetro; adesso ci stiamo occupando del calcolo della viscosità, dilatazione termica, proprietà ottiche, ecc.

La tesi è organizzata nel seguente modo.

Nel capitolo 1, una breve panoramica dei metodi di simulazione atomistica utilizzati durante la Tesi, perché diversi livelli di teoria sono stati selezionati in base alle loro capacità di risolvere specifici problemi: *ab-initio*, Meccanica Molecolare e Dinamica Molecolare.

Nel capitolo 2, un'introduzione alla chimica del cemento e i presupposti necessari per comprendere i risultati e discussioni dei sistemi analizzati in questa Tesi: una descrizione delle fasi clinker, dei superfluidificanti, il processo di idratazione, la struttura della pasta di cemento e i metodi computazionali più comuni nello studio dei materiali cementizi.

Nel capitolo 3, i risultati di quattro simulazioni MD di un sistema costituito da PCE-(23-7-1), un polimero superfluidificante modello, a forma di pettine, costituito da metil-polietilen-glicole metacrilato e acido metacrilico (sette unità nel backbone, una catena laterale e ventitré unità poli-etilen-ossido in catena laterale), le superfici $C_3A$ e $C_3S$, le molecole di $H_2O$ e gli ioni $Ca^{2+}$ e $OH^-$ (pore solution): dalle traiettorie MD sono state calcolate le proprietà conformazionali del PCE.

Nel capitolo 4, i risultati della parametrizzazione delle cariche parziali di amminoacidi non naturali, dell'analisi strutturale del canale e dei ponti salini della proteina Cx26.

Nel capitolo 5, il modello fisico-matematico per il calcolo della composizione dei vetri, l'interpolazione per la dipendenza dalla temperatura delle proprietà termodinamiche e la convalida del modello con un semplice vetro costituito da un ossido misto $Na_2O$-$SiO_2$.

# LIST OF ACRONYMS

| | |
|---|---|
| 1D-DP: | One dimensional density profile |
| AA: | Amino acid |
| $C_3A$: | Tricalcium aluminate, Celite, $3CaO \cdot Al_2O_3$ |
| $C_2S$: | Dicalcium silicate, Belite, $2CaO \cdot SiO_2$ |
| $C_3S$: | Tricalcium silicate, Alite, $3CaO \cdot SiO_2$ |
| C-S-H: | Calcium Silicate Hydrated |
| CG: | Coarse Grained |
| CM: | Center of Mass trajectory |
| DFT: | Density Functional Theory |
| ESP: | Electrostatic Surface Potential |
| ETE: | End to End distance |
| FF: | Force Field |
| HF: | Hartree-Fock Methods |
| LJ: | Lennard Jones |
| MC: | Monte Carlo |
| MD: | Molecular Dynamics |
| MM: | Molecular Mechanics |
| MS-EVB: | Multi-state empirical valence bond model |
| PCE: | Polycarboxylate-ether-based polymer |
| PEO: | Polyethylene-oxide |
| PES: | Potential Energy Surface |
| PTM: | Post-translational modifications |
| QM: | Quantum Mechanics |
| RESP: | Restrained Electrostatic Potential procedure |
| RG: | Radius of Gyration |
| SP: | Superplasticizer |
| TIP3P: | Three-site transferrable intermolecular potential |
| VMD: | Visual Molecular Dynamics |

# LIST OF FIGURES

# LIST OF TABLES

# OVERVIEW OF COMPUTATIONAL ATOMISTIC METHODS

**Introduction of Computational Atomistic Methods**

Atom-level computer simulations are carried out to understand the properties of molecular systems, their structure and microscopic interactions.

Molecular modelling makes it possible to compare properties of an experimental system with those calculated in a model system, resembling as much as possible the experimental one. If the model agrees with the experiment, we may surmise to have at least an adequate estimate of the intermolecular interactions in the system, otherwise further improvement of the model is needed. On the other hand, we may consider computer simulations as experiments to test theories before they are applied in the real world, as computer experiments.

In a computer experiment we perform simulations in a model system and compare the results with the theoretical predictions of an approximate analytical theory that is applied to the same model system. If the simulation results disagree with the theory's predictions, the theory is flawed. Molecular modelling also compliments experimental work, enabling one to see what happens at the microscopical (molecular) level instead of just the macroscopical changes. Testing new theories and systems *in silico* is fairly uncomplicated, at least if compared with the difficulties of changing actual experimental conditions in real word. In addition, computer simulations can be used to predict properties of new materials and aid in their development [Frenkel2001; Ercolessi1997; Seppälä2013; Leach2001].

The theories underlying atomistic simulation methods are independent from the existence of computers; however, the mathematical complexity of the algorithms to be solved make computers indispensable in any atomistic simulation.

In the present Thesis different levels of theory were employed, each of them chosen to solve specific questions in view of their capabilities. Thus, the simulation details for each problem are included in the corresponding chapter.

The aim of this first chapter, then, is just to provide idea basic summary of the main tenets and capabilities of the computational methods employed during this research. A more complete and technical description of the formalisms would be too long, and

is beyond the scope of this Thesis. However, the references to get further information are given through the text [Manzano2009].

### *Ab initio* Methods

*Ab initio* methods, or first principles methods, are derived directly from theoretical principles, and do not require, at least in principle, any adjustable parameter during their application to the description of an actual molecular system.

In most structural (i.e. non dynamic) studies of molecular systems, the starting point is the time indipendent Schrödinger equation:

$$\hat{H}\Psi_i(\boldsymbol{r}) = E_i\Psi_i(\boldsymbol{r}) \tag{1.1}$$

Here $\hat{H}$ is the *Hamiltonian operator*, which acts upon the wave function of the system in a determined state *i*, $\Psi_i(\boldsymbol{r})$, and return the system energy at state *i*, $E_i$.

The Hamiltonian is a Hermitian operator corresponding to the total energy. For a general system of *N* electrons and *M* nuclei, in the absence of external fields [Leach2001] it can be written as:

$$\hat{H}=\hat{T}_{ele}+\hat{T}_{nuc}+\hat{V}_{ele-nuc}+\hat{V}_{ele-ele}+\hat{V}_{nuc-nuc} \tag{1.2}$$

The two first terms take into account the kinetic energy of the electrons and nuclei; the remaining terms are the potential energy due to interactions between electrons and nuclei, interaction between electrons and interaction between nuclei.

The wave function $\Psi_i(\boldsymbol{r})$ contains all the information of a system in a determinate state *i*. The wave function is not an observable itself; only its square has physical interpretation as the probability distribution to find the system in a determined state: eg, the square of an electronic wave function give us the electronic density [Levine1991].

The analytical resolution of the Schödinger equation is not possible with few exceptions. The *variational principle*, gives the recipe for a systematic approach to the correct solution: the construction of an acceptable wave function must track the objective of obtaining an energy as low as possible, and thus, closest to the ground state value.

The evaluation of the Schrödinger equation can be further symplified for molecules

according to the *Born-Oppenheimer approximation*. The wave function of a molecular system can be separated in two terms, the electronic $\Phi_{ele}$ and the nuclear $\Phi_{nuc}$, and both can be studied separately:

$$\hat{H}\Phi_{ele}(\boldsymbol{r})\Phi_{nuc}(\boldsymbol{r}) = E_{total}\Phi_{ele}(\boldsymbol{r})\Phi_{nuc}(\boldsymbol{r}) \quad (1.3)$$

The justification is that under typical physical conditions, the nuclei are considerably heavier than the electrons (neutrons and protons are $\sim 2 \cdot 10^3$ times heavier than electrons) and consequently the nuclei move slower than the electrons. In fact, the nuclei can be considered fixed while computing the electronic states.

The kinetic term of fixed nuclei in the Hamiltoniani $\hat{T}_{nuc}$ is equal to zero, and the potential term due to inter-nuclei $\hat{V}_{nuc-nuc}$ interactions is constant.

Then, the Schrödinger equation (1.1) for the electrons is written as:

$$[\hat{T}_{ele} + \hat{V}_{ele-nuc} + \hat{V}_{ele-ele}]\Phi_{ele}(\boldsymbol{r}) = E_{ele}\Phi_{ele}(\boldsymbol{r}) \quad (1.4)$$

The interaction between frozen nuclei and the nuclei kinetic energy are considered. The energy obtained for the electronic part also contributes as a potential term:

$$[\hat{T}_{nuc} + \hat{V}_{nuc-nuc} + E_{ele}]\Phi_{nuc}(\boldsymbol{r}) = E_{total}\Phi_{nuc}(\boldsymbol{r}) \quad (1.5)$$

Due to the Born-Oppenheminer approximation, the *Potential Energy Surface* (PES) of a molecular system can be defined. The PES is the surface defined by the electronic energy over all the possible nuclear coordinates; some concepts such as the local stability and the geometries of equilibrium are defined as critic points of the PES [Cramer2002; Jensen2007].

**The Hartree-Fock Method**

The Schrödinger equation can be solved analytically for hydrogen-like atoms, with a nucleus and one electron: the eigenfunctions are called *hydrogen-like wave functions*. For systems with more than one electron, the electrons are not independent, and the problem cannot be solved analytically (the so called *many-body problem*). The first approximation to overcome the problem is the *Hartree method* or independent particle approximation. In such method, each electron is treated separately, splitting up the wave function as a product of one-electron wave functions. Thus, the Hamiltonian is that which corresponds to one electron, and the electron-electron

interaction is calculated separately, as one electron moving in the average potential of the rest (known as the *mean-field approach*).

The total electronic Hamiltonian is:

$$\hat{H}_{ele} = \hat{T}_{ele} + \hat{V}_{ele-nuc} + \hat{V}_{ele-ele} = \sum_{i}^{N} \hat{h}_1 + \sum_{i,j\neq i}^{N} \hat{J}_{ij} \tag{1.6}$$

where $\hat{h}_1$ is the *One electron* Hamiltonian and $\hat{J}_{ij}$ is th *Coulomb Integral* which represents the classical repulsion between two charge distributions [Levine1991; Leach2001; Cramer2002].

Despite the Hartree method is a useful approximation, the obtained wave function violates the indistinguishability of electrons. Moreover, electrons are fermions, so their wave function must be antisymmetric. They have associated a quantum angular momentum (spin) with values = ±1/2, and must obey the Pauli´s exclusion principle. Therefore, no more than two electrons can be in the same orbital.

The way of representing the antisymmetric electronic wave functions for a system of N electrons is the Slater determinant:

$$\Psi_{ele}(\boldsymbol{r}_1,\boldsymbol{r}_2,\ldots,\boldsymbol{r}_N) = \Psi_{SD} = \frac{1}{\sqrt{N!}} \begin{vmatrix} \chi_1(1) & \chi_2(1) & \cdots & \chi_1(N) \\ \chi_2(1) & \chi_2(2) & \cdots & \chi_2(N) \\ \vdots & \vdots & \ddots & \vdots \\ \chi_1(N) & \chi_2(N) & \cdots & \chi_N(N) \end{vmatrix} \tag{1.7}$$

where are the spin-orbitals, a one electron wave function product of a spatial part and a spin part. The *Hartree-Fock method* (HF) is an extension of the Hartree method, where the electron wave function is described by a Slater determinant. Again, each electron is considered to move independently for the others in the spin orbital space. The kinetic energy and the repulsion between electrons and nuclei is evaluated as in the Hartree method. However, the interaction with other electrons has now a new contribution due to the spin, the *exchange integral* $K_{ij}$ without classical analogy. The *Fock operator* for each electron is:

$$\hat{f}_i = -\hat{T}_{ele} + \hat{T}_{nuc} + \hat{V}_i^{HF}\{j\} = \hat{h}_i + \sum_{j}^{N}(J_j - K_i) \tag{1.8}$$

where is the $\hat{V}_i^{HF}\{j\}$ HF potential, $\hat{h}$ is the Hartree Hamiltonian for one electron and $J_j$ and $K_i$ are the operators defined so as to give the corresponding Coulomb and exchange integrals respectively.

In 1951 Roothaan proposed to represent each one electron orbital $\chi_i$ as a *linear combination of atomic orbitals* (LCAO) [Roothaan1951]:

$$\chi_i = \sum_{j=i}^{N} a_{ij}\varphi_i \tag{1.9}$$

where are $a_{ij}$ the coefficients in the linear combination of the atomic orbitals $\varphi_i$.

Although called atomic orbitals, the functions $\varphi_i$ are usually a set of known functions as those proposed by Slater, Gaussian functions, etc, and commonly called *basis functions* or *basis functions* [Jensen1999].

If the Schrödinger equation is written using the Fock operator and the LCAO approach, integrating over all the space and rearranging the terms, we obtain the Roothaan-Hall secular equation:

$$\sum_{j=1}^{N} a_{ij}(F_{ij} - \varepsilon_i S_{ij}) = 0 \tag{1.10}$$

where $\varepsilon_i$ are the corresponding energies for the orbitals $\chi_i$, $F_{ij}$ and $S_{ij}$ are the *Fock* and *overlap integrals*.

The secular equation is solved by finding the various roots $\varepsilon_i$. Then, the energy is calculated as a sum of the energies for the *N* occupied orbitals, minus a correction term that arises from the double counting of the electron-electron interaction due to the one electron Hamiltonian in the Fock operator:

$$E = \sum_{i=1}^{N} \varepsilon_i - \sum_{i=1}^{N/2}\sum_{j=1}^{N/2}(2J_{ij} - K_{ij}) \tag{1.11}$$

The Hartree-Fock method neglects the electron correlation due to the mean-field approximation. The so called post-HF methods were devised to include electron correlation to the multi electron wave function [Cramer2002; Jensen2007; Manzano2009].

We are now in a position to consider how the HF theory can be used to perform practical QM calculations on molecular systems

The basis sets most commonly used in QM calculations are composed of atomic functions. An obvious choice would be Slater type orbitals. Unfortunately, Slater functions are not particularly amenable to implementation in molecular orbital calculations

It is common to replace the Slater orbitals by function based upon Gaussians: a major advantage of Gaussian functions is that the product of two Gaussians can be expressed as a single Gaussian, located along the line joining the centre of two Gaussians [Leach2001].

**Density Functional Theory**

The wave function plays a key role in HF methods. Although the wave function has not physical meaning itself, its square has the physical interpretation as the probability to find the electrons in a determined volume. To calculate the energy through the electronic density seems to be, therefore, a way to overcome the manipulation of the wave function.

Hohenberg and Kohn established the basis of Density Functional Theory (DFT) with two theorems [Hohenberg1964]. First, the *existence theorem* demonstrates that the wave function of a system in the ground state is a functional of the electronic density, $\Psi_i(\boldsymbol{r}) = f[\rho(\boldsymbol{r})] = f[\rho]$, and therefore, the ground state properties are also density functionals. Second, the *Hohenberg and Kohn variational principle* states that the energy obtained from a wave function constructed from a guess electronic density is always greater than or equal to the real ground state energy. It must be noted that DFT mainly concerns the ground state properties.

In 1965 Kohn and Sham proposed a self-consistent method to solve the variational problem of minimizing the energy [148]. Using the Born-Oppenheimer approximation, the density-dependent energy can be divided in three parts:

$$E[\rho] = T_{ele}[\rho] + V_{ele-nuc}[\rho] + V_{ele-ele}[\rho] \tag{1.12}$$

Parallel to the operators in the HF methods, $T_{ele}[\rho]$, $V_{ele-nuc}[\rho]$ and $V_{ele-ele}[\rho]$ are the density functionals which account respectively for the electron kinetic energy, the potential energy due to the electron-nucleus interactions, and the potential energy due to the interaction between electrons. Kohn and Sham simplify the problem taking as starting point an ideal system of non-interacting electrons with the same

density as the ground state density of the real system. The equation (1.12) is rewritten then as:

$$E[\rho] = T_{n.i.ele}[\rho] + V_{ele-nuc}[\rho] + V_{n.i.ele-ele}[\rho] + \Delta T_{ele}[\rho] + \Delta V_{ele-ele}[\rho] \quad (1.13)$$

The first term in the right hand side of equation (1.13) is the kinetic energy of electrons derived by Thomas and Fermi for an infinite homogeneous gas made of noninteracting electrons. The second term is the potential energy due to the interaction of a charge density (electronic density) and point charges (nucleus). The third term is the potential energy due to repulsion between two densities of charge [Leach2001; Manzano2009].

The last two terms include all non-classical interactions of the electrons. They are collected together as the exchange-correlation energy, $E_{xc}$, and include the correlation and exchange energies, as well as all the corrections to the one electron kinetic energy between the ideal non-interacting system and the interacting one. If orbitals are considered, similar expressions to those of the HF method are achieved, called Kohn-Sham equations:

$$\hat{h}_i^{KS}\chi_i = \varepsilon_i\chi_i \quad (1.14)$$

where $\chi_i$ are the Kohn-Sham set of one electron orbitals that reproduce the ground state electronic density, $\varepsilon_i$ their corresponding energies, and $\hat{h}_i^{KS}$ the one electron *Kohn-Sham operator*:

$$\hat{h}_i^{KS} = \hat{T}_{ele} + \hat{V}_{ele-nuc} + \hat{V}_{ele-ele} + \hat{V}_{xc} \quad (1.15)$$

The one electron orbitals can be expressed as LCAO:

$$\hat{h}_i^{KS}\sum_{j=i}^{N} a_{ij}\varphi_i = \varepsilon_i\sum_{j=i}^{N} a_{ij}\varphi_i \quad (1.16)$$

and as secular equation is obtained. The numerical procedure to solve the secular equation is analogous to that of Hartree methods, with the exception of the exchange-correlation part that depends on the density and therefore must be solved numerically by grid integration methods [Martin2004].

Unfortunately, the $V_{xc}$ functional in equation (1.15) is unknown (with the exception of the free electron gas). Thus, an approximated expression for the $E_{xc}$ that describe reasonably well the expected real value of $E_{xc}$ must be found. The exchange-correlation energy is commonly expressed as:

$$E_{xc}[\rho] = E_{xc}[\rho(\boldsymbol{r})] = \int \rho(\boldsymbol{r})\varepsilon_{xc} d\boldsymbol{r} \tag{1.17}$$

where $\varepsilon_{xc}$ is called energy density. There are different approaches to obtain $\varepsilon_{xc}$, usually as a sum of the different contributions ($\varepsilon_x$ and $\varepsilon_c$).

An useful approach is the *Hybrid Method*, which makes a mixture between HF and DFT to obtain an accurate $E_{xc}$: one of the most commonly used versions is B3LYP, which stands for Becke, 3-parameter, Lee-Yang-Parr.

Hybridization with HF exchange provides a simple scheme for improving many molecular properties, such as atomization energies, bond lengths and vibration frequencies, which tend to be poorly described with simple *ab initio* functionals [Perdew1986].

**Molecular Mechanics Methods**

Molecular mechanics (MM) methods are based on two basic assumptions.

The first one is the Born-Oppenheimer approximation. In *ab initio* methods, nuclei can be assumed frozen during the first step with respect from the electronic motion. Then, the electronic arrangement is studied. In other words, it could be considered that electrons can adjust instantaneously to the nuclei position for any movement. The system energy in a configuration can be, therefore, calculated as a function of the nuclear positions, with the electrons around them in an optimal distribution [Leach2001].

The second assumption is that each nucleus can be studied as a classical particle: the PES of the system can be evaluated according to Newtonian mechanics. The presence of electrons is not taken into account explicitly but it is implicit in the description of the atoms. They are simulated as spheres, with an assigned radius and charge, interacting by means of a collection of two or many body interatomic potentials [Cramer2001; Jensen1999].

The main advantage of molecular mechanics methods is that they can deal with a large number of particles (atoms), with a relative low computational effort. If the employed force field (FF) describes well the system, it could provide accurate information on structures, thermodynamics, and mechanical properties with a low computational cost.

Nevertheless, they present two main drawbacks. On the one hand, there is no guarantee that certain potentials could simulate properly structures different from the originals used to fit them. The potentials are usually built up to describe the interactions of atoms under a given neighbourhood. The same atoms in different environments are expected to interact with each other in different ways. Therefore, before any simulation, the employed sets of potentials must be carefully checked with the experimental data to assess their transferability. On the other hand, molecular mechanics methods cannot provide information of the electronic structure as they omit the electronic nature of the atoms.

A MM FF is a simplified yet accurate enough model to describe the intra-molecular and inter-molecular interactions in a system. It contains the functional form of the potential energy that best describes a system's molecular structure and for each atom type a set of fitted parameters that are used in the energy and force calculation.

A general FF contains the following information: i) a list of atom types (differentiates an element according to its placement, e.g. oxygen in water and oxygen in mineral structure) and charges assigned to each type; ii) atom typing rules linking an atom type to its element type and chemical microenvironment (e.g. number and nature of connected atoms); iii) functional forms of the potential energy components and parameters for the components; iv) rules for generating parameters that were not explicitly defined.

The functional form of the energy expression takes into account both bonded i.e. atoms linked by covalent bonds and non-bonded interaction terms. The total energy in general form can then be written as

$$E_{total} = E_{bonded} + E_{non-bonded} \tag{1.18}$$

where the bonded term takes into account interactions such as

- *Bond stretching* describes the change in energy which occurs due to the change in bond length from its equilibrium value.
- *Angle bending* describes the change in energy due to change in the angle between two sequential covalent bonds from the equilibrium value.
- *Torsion describes* the change in energy of three bonds connected as ij, JK and KL due to change in the dihedral (or torsional) angle between the planes IJK and JKL from the equilibrium value.
- *Inversion describes* the energy of three atoms bonded to one central atom in

the same plane due to an out of plane configuration.

and can then be expressed as a sum of these interactions:

$$E_{bonded} = E_{bond-stretching} + E_{angle-bending} + E_{torsion} + E_{inversion} \quad (1.19)$$

The non-bonded energy takes into account the electrostatic interactions and van der Waals (vdW) interactions;

$$E_{non-bonded} = E_{Coulomb} + E_{vdW} \quad (1.20)$$

Each FF has a set of parameters that are predetermined for all atom combinations in a specific (target) system to mimic with reasonable accuracy the results of experiments or quantum chemical calculations. The more general the target system is, i.e. covering a larger set of elements, the more simplifications these parameters contain and thus the accuracy of the FF is lower. On the other hand, the more accurate the FF is, the more computational resources are needed in the simulation. Therefore, the choice of a FF has great impact on the validity of results [Seppälä2013].

**Molecular Dynamics Methods**

MD methods calculate the equilibrium properties of a system following the atoms over a certain time period.

In a general classical system, any state can be completely described from the position $\boldsymbol{q}$ and momentum $\boldsymbol{p}$ of all the particles that composes the system.

$$\boldsymbol{q} = (q_x^1, q_y^1, q_z^1, q_x^2, q_y^2, q_z^2, \ldots, q_x^N, q_y^N, q_z^N) \quad (1.21)$$

$$\boldsymbol{p} = (p_x^1, p_y^1, p_z^1, p_x^2, p_y^2, p_z^2, \ldots, p_x^N, p_y^N, p_z^N) \quad (1.22)$$

In the phase space each point represents the $\boldsymbol{q}$ and $\boldsymbol{p}$ of the particles in the system, and the evolution of them can be followed as a trajectory. The imaginary collection of the system copies in each state or phase points, considered all at once, is called *ensemble*.

Any system property, lets say $A$, of the system at the equilibrium can be calculated as an average:

$$\langle A \rangle = \int\int A(\boldsymbol{q},\boldsymbol{p}) P(\boldsymbol{q},\boldsymbol{p})\, d\boldsymbol{q}\, d\boldsymbol{p} \quad (1.23)$$

where $A(\boldsymbol{q},\boldsymbol{p})$ is the property value in one phase space point, and $P(\boldsymbol{q},\boldsymbol{p})$ is the system probability to be in that point. The quantity computed from equation (1.14) is an *ensemble average*. However, the probability for a system being in some of the phase

space points is near-zero, and therefore, those points do not contribute to the *A* property expected value. Thus, the $\langle A \rangle$ average value can be calculated checking the most probable configurations of a system, instead all the possible configurations; this methodology is followed by MC methods.

In the case of MD the methodology is different. If a system starts in a phase space configuration close to the equilibrium configuration, and its trajectory is followed at constant energy, it seems likely that the system will evolve sampling the most probable points of the phase space. If the starting point is correct, the *A* property average can be calculated as:

$$\langle A \rangle = \frac{1}{N} \sum_{i}^{N} A(\boldsymbol{q}, \boldsymbol{p}, t_i) \tag{1.24}$$

where *N* is the number of measurements at different times $t_i$.

In the limit of continuous sampling and during an indefinitely time, the equation (1.15) becomes:

$$\langle A \rangle = \lim_{t \to \infty} \frac{1}{t} \int_{t_0}^{t_0+t} A(t)\, dt \tag{1.25}$$

The *ergodic hypothesis* states that, for an isolated system at the equilibrium, all the accessible states are equally probable over a long time period, independently from the starting time, initial positions ***q***, and momenta ***p*** for a given number of *N* atoms in a volume *V* and at constant energy *E*.

Thus, the property average over time and the average over all the states (*ensemble average*) at equilibrium are equal [Frenkel1996; Leach2001; Cramer2002; Rapaport 1995; Manzano2009].

In MD simulations, the desired property must be computed from the particles position and momentum in the system.

The particles in the system evolve following the classic Newton's motion equation:

$$\boldsymbol{F}_i = -\nabla_{\boldsymbol{q}_i} V(\boldsymbol{q}_1, \ldots, \boldsymbol{q}_i, \ldots, \boldsymbol{q}_N) \tag{1.26}$$

for the *N*-body system under the influence of specified forces; to integrate these equations, the forces acting on every particle must be known.

Usually the same functional forms as in the MM methods mentioned in the previous section are employed in MD simulations. They allow the study of large systems during long time periods.

However, the use of a FF implies some disadvantages, such as their transferability.

There are many algorithms to integrate Newton's equation (1.16) and all of them present advantages and disadvantages: problems in the energy conservation, energy drifts, irreversibility, high dependences of the starting point, or the need of short time steps are some of them [Frenkel1996]. The most employed due to its simplicity and performance is the Verlet algorithm [Verlet1967]. The initial velocities are usually adjusted to a desired value of the (kinetic) energy, conserving the total momentum equal to zero. The coordinates of each particle are first expanded in Taylor series around the time up to the fourth term, in both "directions", backward $(t\text{-}\Delta t)$ and $(t+\Delta t)$ forward. Summing both equations we obtain:

$$q(t+\Delta t) \approx 2q(t) - q(t\text{-}\Delta t) + \frac{F(t)}{m}\Delta t^2 \pm O(\Delta t^4) \tag{1.27}$$

where $q$ is the particle position, $F$ are the forces acting on the particle, $m$ is the mass of the particle, $t$ is the current time, and $\Delta t$ is the time step. The velocities are not needed to calculate the next positions, only the forces together with the current and past positions. However, the velocities can be derived from the rest of the Taylor series, forward and backward:

$$v(t) = \frac{q(t+\Delta t) - q(t\text{-}\Delta t)}{2\Delta t} + O(\Delta t^2) \tag{1.28}$$

Other algorithms are alternatives to the Verlet scheme, such as the Euler, the Leap Frog, and the velocity Verlet algorithms. Higher-Order schemes as the predictor correction algorithm employ information from higher order derivatives of the Taylor expansion [Frenkel1996; Rapaport1995; Hoover1986].

The ergodic hypothesis states that the time average in MD is equal to the ensemble average in MC methods. In MD simulations the time average properties of a system of $N$ particles, are calculated while keeping constant the volume and the energy are measured. Those are the conditions of a microcanonical ensemble (NVE).

However, in many cases it is convenient to perform calculations at constant pressure or temperature. For that purpose there are some alternatives that will be explained in the following.

One way to carry out MD simulation in the canonical ensemble (NVT), is by coupling the system to an imaginary heath bath [Andersen1980]. The temperature is preserved constant by exchanging energy with this bath. The energy exchange is done applying impulsive forces on randomly selected atoms at a certain frequency. This process can be considered as a MC step which varies the energy between the

usual MD steps in the NVE ensemble. The coupling strength between the system and the bath is controlled by the frequency of the energy exchange steps.

Under constant pressure and temperature, in the so-called isobaric-isothermal ensemble (NPT) the pressure can be maintained constant at each time step varying the size and the shape of the simulation box [Hoover1986].

Special considerations must be made for the evaluation of electrostatic interactions and vdW terms because their calculation determines the time length necessary to complete a MD simulation.

For non-bonding energy is customary introducing a radius of *cut-off* that determines a sphere around the atom of the out of which interactions are ignored: this is an approximation reasonable for vdW interaction, which decay rapidly to great distance, but not enough for the electrostatic interactions that decay like $1/r$.

The calculation methods most commonly used for electrostatic interactions are Ewald Summation (ES) and Particle-Mesh-Ewald (PME). ES is a special case of the summation of the Poisson in which energy of interaction it is calculated in Fourier space and not in the real [Frenkel1986]. PME is an improvement and consists to apply ES at fixed locations of a grid rather than in the positions of atoms. Both methods are very fast, in fact, for $N$ particles ES scale as $N^{3/2}$ and PME like $Nln(N)$ [Frenkel1996].

A MD simulation consists of the following steps: initialization, minimization, equilibration and dynamics run. The simulation is initiated by assigning atoms with initial positions (compatible with the structure one wishes to simulate) and velocities (usually set according to the desired system temperature). The next step is equilibrating the system i.e. finding the system in its free energy minimum. This can be done by simply performing a preliminary MD run long enough so the system's thermodynamic quantities (e.g. temperature and potential energy) fluctuate around constant average values. When this is achieved the actual calculation run can be done. The time scale of these simulations generally ranges from dozens picoseconds to hundreds of nanoseconds: MD simulations are made under conditions in which the limits time and space become important. A simulation is "safe", from the point of view of time, if its duration is much greater compared to the relaxation times of the quantity which one is interested in study; from the spatial point of view, it is useful to compare the size MD cell with those of the system studied, using functions correlation [Frenkel2001; Seppälä2013].

# INTRODUCTION TO CEMENT CHEMISTRY

**Introduction to cement-based materials**

The meaning of the word “cement” is binder, a substance that sets and hardens and can bind other materials together.

In the building industry with the term cement, or more properly hydraulic cement, it means a variety of construction materials, known as hydraulic binders, which mixed with water develop adhesive properties.

The cement paste, cement and water, is employed as a binder in mixture with inert materials such as sand, gravel or crushed stone: i) in case of the cement paste is mixed with sand you get the cement mortar; ii) in case of the cement paste is mixed with aggregates of different sizes (sand, gravel and gravel) you get the concrete; iii) in case of concrete is coupled with a reinforcement constituted by steel rods, appropriately positioned, you have the reinforced concrete.

Concrete comprises in quantity the largest of all man-made materials; although aggregates make up the three fourths of the volume of concrete, the active constituent of concrete is cement paste, and the properties and performance of concrete are largerly determined by the properties of the cement paste. Admixtures in concrete confer some beneficial effects such as acceleration, retardation, air entrainment, water reduction, plasticity, etc., and these effects are due to their action on cement [Ramachandran1997].

There are different types of cements, different for the composition, by the properties of strength and durability and therefore for the intended use.

One classification is done by looking if they need water to set, hydraulic cements, or not, non-hydraulic cements. The first grop is the one employed in construction, due its better performance. Some examples of hydraulic cements are Portland, pozzolan-lime, calcium sulphoaluminate and geopolymeric cements.

Portland cement is by far the most common type of cement in general use around the world: it’s produced by pulverizing clinker consisting essentially of calcium silicates. Different classifications of Portland cement depend on the exact composition and additives employed (Type I, II, II, IV and V), as well as the final compressive

strength. The raw materials for manufacture of Portland cement contain, in suitable proportions, silica, aluminum oxide, calcium oxide and ferric oxide, magnesia, alkalis, phosphates, fluorine compounds, zinc oxide and sulfides. The cement clinker is produced by feeding the crushed, ground and screened raw mix into a rotary kiln and heating to a temperature of about 1300-1450°C.

At this temperature, the mixture melts and several chemical processes take place: lose of free water, decarbonation, and formation of the clinker. Finally, the clinker nodules are milled to get the desired particle size, and additives such as gypsum are added.

Today cement-base materials are leaders in the construction sector, in terms of investments and production. In 2010, the world production of hydraulic cement was 3300 million tonnes; the economic impact of cement industry is in general positive, especially for developing countries: the top three producers were China with 1800 million of tonnes (Mt), India with 220 Mt and USA with 63.5 Mt for a combined total of over half the world total by the world's three most populated states [vanOss2011].

Cement manufacture causes environmental impacts at all stages of the process. These include emissions of airborne pollution in the form of dust, gases, noise and vibration when operating machinery and during blasting in quarries, and damage to countryside from quarrying: the Cement Industry is responsible for approximately 5% of global anthropogenic carbon dioxide emissions. Atmospheric concentrations of greenhouse gases cannot be stabilized without addressing this important emissions source. The industry emits ~900 kg of $CO_2$ for every 1000 kg of cement produced [Mahasenan2002].

Due to the large economic and environmental impact of cement, there is an increasing interest in both basic and applied research of cement-based materials; the number of cement-related papers published in scientific journals till now is more than two hundred thousand: the resul was obtained searching the word “cement” in titles, keywords and abstracts employing ISI ScienceDirect and as search engine.

Despite its ubiquity, and contrary to most people belief, cement is a very complex and not fully understood material; cement research is a multidisciplinary field where many aspects are under study, covering from the intrinsic nature of the material, to the manufacture and performance of the manufacturing product, and going through the improvement of its characteristics or development of innovative cements.

In the specialized bibliography, the term cement strictly refers to the clinker including additives. When cement is mixed with water, the correct term to name it is *cement paste* or *cement matrix* if speaking of the pure material, or *mortar* and *concrete* if aggregates are incorporated. The hydration process is a very complex transformation, during which a myriad of chemical reactions take place, and the powder transforms progressively in a grey paste which sets and hardens. In few words, cement paste can be described as a multiphase matrix, where crystalline agglomerates of different sizes are bound by an amorphous hydration product of variable stoichiometry, the *Calcium Silicate Hydrated* (C-S-H) gel. The crystalline agglomerates could be either hydration products such as portlandite and ettringite, or unreacted clinker grains which persist after the hydration process. The C-S-H gel is the most important hydration product, accounting for the 70% of the cement paste volume, and it is the principal responsible for the cement paste cohesion and properties. It is heterogeneous in morphology and composition, depending on the local environment [Taylor1986; Richardson1992; Richardson1993; Richardson2000; Richardson2004]. Hydrated cement pastes have associated a pore structure with different hierarchical levels depending on the size. Macropores (100 μm - 5 mm) are associated to air inclusions during the setting process, capillary pores (10 nm - 5 μm) to empty space shaped during the hydration, and nanopores (<10 nm) are an intrinsic characteristic of the C-S-H gel due to the spatially random packing of its particles [Manzano2009].

**Clinker phases**

Portland cement clinker is the result of heating process of clays and limestone ($CaCO_3$) up to 1450°C. As the temperature progressively increases, a series of reactions take place. At a temperature of about 100°C (drying zone), free water is expelled. In the preheating zone (100-750°C), firmly bound water from the clay is lost. In the calcing zone (750-1000°C), calcium carbonate is dissociated. In the burning zone (1000-1450°C), partial fusion of the mix occurs, with the formation of $C_3S$, $C_2S$ and clinker. In the cooling zone (1450-1300°C), crystalization of melt occurs with the formation of calcium aluminate and calcium ferrite. After firing the raw materials for the required period, the resultant clinker is cooled and ground qith about 4-5% gypsum to a specified degree of fineness.

The final composition of a typical Portland cement clinker is given in **Table 2.1**. It can be seen that the most abundant oxides are CaO and $SiO_2$, the main components of the predominant phases, alite ($C_3S$) and to a minor extend belite ($C_2S$). Other oxides ($Al_2O_3$, $Fe_2O_3$ and MgO) are present in smaller but not negligible quantities, corresponding to mineral phases like $C_3A$, and ferrite ($C_2A_xF_{1-x}$ with $0 < x < 0.7$).

| | $Na_2O$ | MgO | $Al_2O_3$ | $SiO_2$ | $P_2O_5$ | $SO_3$ | $K_2O$ | CaO | $TiO_2$ | $MnO_3$ | $Fe_2O_3$ |
|---|---|---|---|---|---|---|---|---|---|---|---|
| **Alite** | 0.1 | 1.1 | 1.0 | 25.2 | 0.2 | 0.0 | 0.1 | 71.6 | 0.0 | 0.0 | 0.7 |
| **Belite** | 0.1 | 0.5 | 2.1 | 31.5 | 0.2 | 0.1 | 0.9 | 63.5 | 0.2 | 0.0 | 0.9 |
| **Alluminate** | 1.0 | 1.4 | 31.3 | 3.7 | 0.0 | 0.0 | 0.7 | 56.6 | 0.2 | 0.0 | 5.1 |
| **Ferrite** | 0.1 | 2.8 | 15.2 | 3.5 | 0.0 | 0.0 | 0.2 | 46.0 | 1.7 | 0.7 | 29.8 |

**Table 2.1**: Composition of a typical Portland cement clinker, expressed by %wt [Taylor1990].

A general description of these four main phases is in the following.

### Alite, $C_3S$

It is the major, and characteristic, mineral phase of Portland cement, ~70-80%. The alite found in Portland cement differs in composition from simple $C_3S$; it is a solid solution and contains minor amounts of other oxides besides CaO and $SiO_2$: a typical composition is 71.6% of CaO, 25.2% of $SiO_2$, 1.0% of $Al_2O_3$, 1.1% of MgO, 0.7 % of $Fe_2O_3$, 0.1% of $Na_2O$, 0.1% of $K_2O$ and 0.2% of $P_2O_5$.

Pure $C_3S$ exhibits the following set of reversible phase transitions upon heating

$$T_1 \xleftrightarrow{620°C} T_2 \xleftrightarrow{920°C} T_3 \xleftrightarrow{980°C} M_1 \xleftrightarrow{990°C} M_2 \xleftrightarrow{1060°C} M_3 \xleftrightarrow{1070°C} R$$

The letters indicate the crystal simmetry of the polymorph (T=triclinic, M=monoclinic and R=rhombohedral) and the subscript variants in the structure for a particular symmetry. The pure compound, when cooled to room temperature, is thus $T_1$. In production clinkers, due to the incorporation of foreign ions, the form present at room temperature is normally $M_1$ or $M_3$, or a mixture of these; rarely, $T_2$ is found ($M_1$-$M_5$, $T_1$).

The impurities play also a key role stabilizing alite from decomposing into $C_2S$ and lime at temperatures below 1250ºC. The common substitutions are those of $Mg^{2+}$ for $Ca^{2+}$, $2Al^{3+}$ or $2Fe^{3+}$ for $Ca^{2+} + Si^{4+}$, and partly $4Al^{3+}$ for $3Si^{4+}$.

The crystal structure of the different alite polymorphs is similar, all of them closely related to the R phase [Moranville1992; DeLaTorre2002; Nishi1984; Nishi1985;

Jeffery1952]. The structure, wich consists in $SiO_4^{4-}$ tetrahedra and $Ca^{2+}$ and $O^{2-}$ ions, is given in **Figure 2.1**.

The polymorphs differ in the orientation of the $SiO_4^{4-}$ tetrahedra, which affects to the symmetry and the coordination of the Ca and O atoms. Even for a given polymorph, the high disorder in the orientation of those $SiO_4^{4-}$ groups causes also different Ca-O coordination [Manzano2009; Taylor1990].

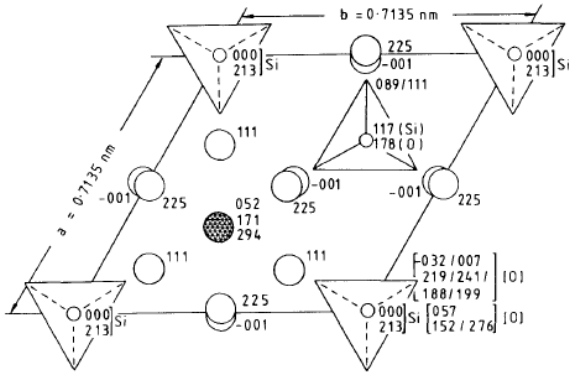


**Figure 2.1**: Crystal structure of the R modification of $C_3S$, based on the results of Nishi and Takeuchi (N2) and showing calcium atoms (large open circles). silicon atoms (small, open circles), oxide ions (large. hatched circle) and oxygen tetrahedra (triangles) [Taylor1990].

### Belite, $C_3S$

Belite is the second phase of importance in ordinary Portland cement. Similar to alite, is chemically modified respect $C_2S$ pure and presents a sequence of reversible polymorphs with the temperature

$$\gamma \xleftrightarrow{500°C} \beta \xleftrightarrow{630\text{-}680°C} \alpha_L' \xleftrightarrow{1160°C} \alpha_H' \xleftrightarrow{1425°C} \alpha$$

The greek letters represent different phases of the structure, and the L and H subscripts denote a low temperature and high temperature variants respectively. The $\alpha$, $\alpha_H'$, $\alpha_L'$ and $\beta$ polymorphs have very similar structures, belonging all of them to the family of glaserite, while the $\gamma$ phase is different and belongs to the family of olivine.

The crystal structure of belite is composed by $SiO_4^{4-}$ tetrahedra and $Ca^{2+}$ ions, differing from alite in the absence of $O^{2-}$ ions, see **Figure 2.2**. The $\alpha_H'$, $\alpha_L'$ and $\beta$ polymorphs are derived from the $\alpha$ form by a decrease of the symmetry due to the disorder of $SiO_4^{4-}$ groups and slight changes in the position of cacium atoms

[Barbier1985; Feng1994; Smith1965].

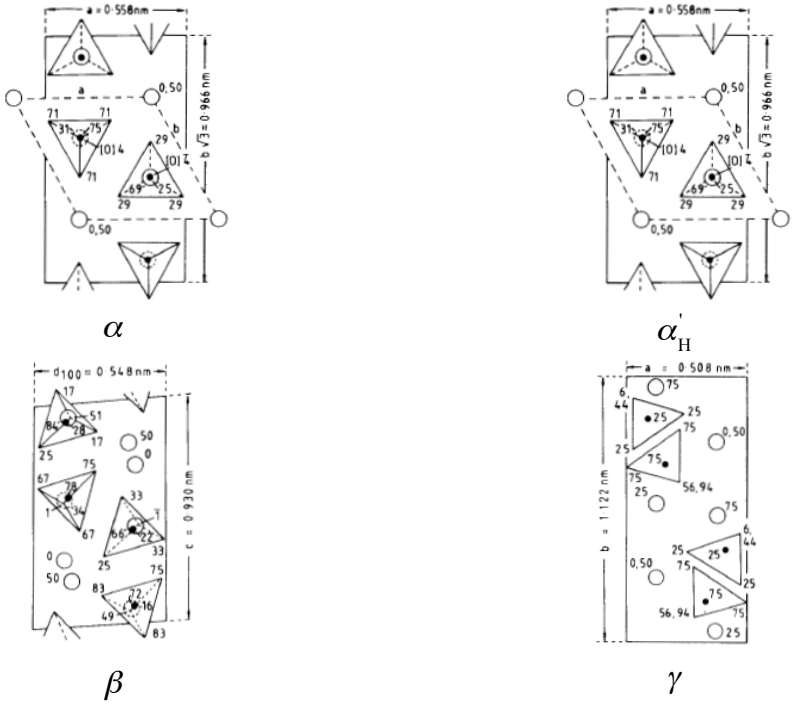


**Figure 2.2**: Crystal structure of $C_2S$ polymorphs. Large, open circles represent calcium atoms, small full circles, silicon atoms and triangles, tetrahedra oxygen atoms [Taylor1990].

Although the $\gamma$ form is the most stable at room temperature, it is not present in the clinker due to stabilization of other phases by guest ions, as in the alite case. The most important incorporation of guest ions is that of Al and Fe atoms. Furthermore, the transition between the similar polymorphs $\alpha$, $\alpha'_H$, $\alpha'_L$ and $\beta$ requires little energy and is completely reversible, while the rearrangement from $\beta$ to $\gamma$ is more sluggish. Consequently, when cooling the clinker, the $\beta$ form persists in metastable equilibrium. This implies an advantage, due to the higher reactivity of the $\beta$ variant with respect to the $\gamma$ form. At the laboratory conditions, where the cooling can be slow enough, the transformation involves cracking of the $\beta$ crystals when some zones transform to the $\gamma$ form. This phenomenon is know as *dusting*, and it is caused by the lower density of the $\gamma$ polymorph [Taylor1990].

**Celite, $C_3A$**

It is the third significant component in Portland cement. Pure $C_3A$ has a cubic symmetry and is stable in all the range of temperatures until melting. Its unit cell is composed of $Al_6O_{18}^{18-}$ rings, with their charge

counterbalanced by $Ca^{2+}$ ions located in the space between rings, as can be seen in **Figure 2.3** [Mondal1975; Stephan2006; Takeuchi1980]. However, the substitution of 2 $Na^{+}$ for $Ca^{2+}$ induces a decrease in the symmetry, and orthorhombic and monoclinic polymorphs appear. For $Na_2O$ contents < 2%, the cubic symmetry is kept, and over it the orthorhombic variant persists until ~4.5%. Substitutions of $Al^{3+}$ by $Fe^{3+}$ or $Si^{4+}$ could also take place. The former is the most significant, though it has little effect in the phase transition, still controlled by the amount of Na [Lee1982; Manzano2009].

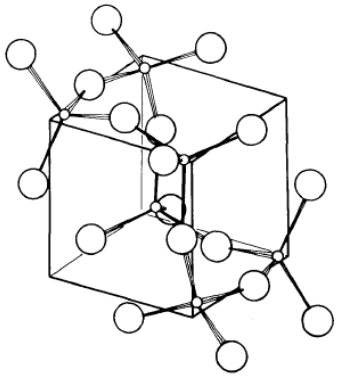

**Figure 2.3**: $Al_6O_{18}^{18-}$ ring in the structure of $C_3A$, showing the situations of the aluminium atoms near to the corners of a cube [Taylor1990].

In the ordinary Portland cement clinkers at room temperature the cubic and orthorhombic polymorphs appear, alone or in combination, while the monoclinic form has not been detected. The cubic form usually is mixed with dendritic crystals of ferrite phases [Taylor1990].

**Aluminoferrite, $C_4AF$**

The aluminoferrite phase is a modification of ferrite ($C_2F$), in which aluminium atoms enter to the structure. The stoichiometry of the solid solution is $Ca_6(Al_{(1-x)}Fe_x)_2O_5$ or $C_2A_{(1-x)}F_x$ in cement chemistry notation. At room temperature and pressure, the composition of the solid solution can vary from x=1 to ~0.3, although x = 0 can be achieved at high pressure [Aggarwal1972].

In the unit cell of pure $C_2F$, there are two different positions occupied by iron ions, one with tetrahedral coordination and the other one with octahedral coordination, being the number of the latter twice the number of the former. Aluminium has a preference for the tetrahedral sites, which are completely occupied for x ~0.67. When

the aluminium substitution starts to take place in the octahedral sites, both the unit cell parameters and the symmetry change [Taylor1990].

For composition in the range x=0.3-0.7, the structure is similar to that of perovskite, $Ca_2TiO_3$ [Colville1972]. It is composed of layers of octahedrally coordinated atoms alternated by tetrahedrally coordinated ones, together with $Ca^{2+}$ ions in the remaining space, see **Figure 2.3**. Probably owing to this structural similarity, the most relevant guest atom which takes part in ferrite is titanium. When high amount of titanium enters the structure, perovskite-like zones appear mixed with ferrite [Marinho1984].

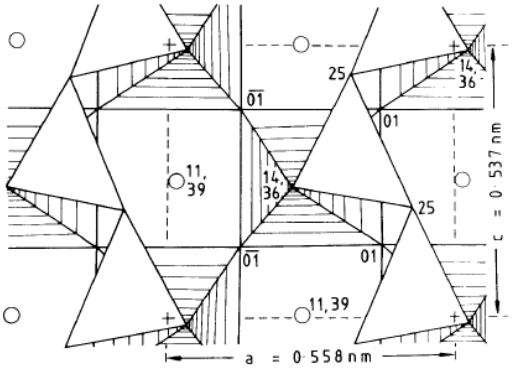


**Figure 2.4**: Crystal structure of $C_4AF$, showing calcium atoms (open circles), $(Fe,Al)O_4$ tetrahedra (triangles), and $(Fe,Al)O_6$ octahedra (hatched squares) [Taylor1990].

### The hydration process

In cement chemistry, the term *hydration* comprises many chemical and physical processes that take place when the clinker is in contact with water [Taylor1990].

During the hydration, the system evolves to form an amorphous paste which sets and hardens. It is a process of enormous complexity due to the great number of involved variables. Cement powder contains a wide variety of components, clinker phases and additives, each of them with impurities and random particle sizes and shapes, distributed heterogeneously among the cement, and with different reaction rates. Other external factors, such as the water to cement ratio (w/c, in %wt) and curing temperature, play also a key role in the final properties.

The process has been studied from a scientific point of view since the early 1900´s [LeChatelier1904] and it is continuously object of many investigations [Fujii1974; Thomas1981; Sujata1992; Peterson2006]. The hydration process is frequently studied independently for each component of the clinker: the most important reactions are those of the main phases, discussed below [Manzano2009].

**Alite, $C_3S$**

Alite hydration is the main responsible for the strength development during the first days. It reacts fast with water. After 28 days ~70% of the alite has reacted, while the process is virtually complete after ~1 year.

The reaction of the pure $C_3S$ is

$$2C_3S+7H_2O \rightarrow C_3S_2H_4\left(\text{C-S-H gel}\right)+3Ca\left(OH\right)_2 \quad (2.1)$$

Portlandite $Ca(OH)_2$ and especially C-S-H gel are the main components ofthe cement paste and the principal responsible for the material properties. When the previous reaction is analysed, it must be noted that the stoichiometry of the C-S-H gel is not fixed [Richardson2004], and the proposed reaction has to be taken as an approximation.

For a given particle size and water to cement ratio, the $C_3S$ hydration is similar to that of the clinker itself [Manzano2009].

**Belite, $C_2S$**

The hydration reaction of $\beta$-$C_2S$ is comparable to that of $C_3S$ in terms of final products and stoichiometry, with the difference that less portlandite is formed

$$2C_2S+5H_2O \rightarrow C_3S_2H_4\left(\text{C-S-H gel}\right)+Ca\left(OH\right)_2 \quad (2.2)$$

A striking difference is that the reaction rate of belite is much slower than that of alite. Only ~30% of belite reacts after ~28 days, and the process is still incomplete after ~1 year, when ~90% has reacted. There are not large differences between the hydration kinetics of the $\beta$ and $\alpha$ forms, while the $\gamma$ phase presents an almost negligible hydraulic activity [Taylor1990].

**Tricalcium Aluminate, $C_3A$**

The average $C_3A$ content in Portland cement is about 4-11% but it influences significantly the early reactions; it reacts very fast with water. This process, known as *flash setting*, is not desired, since it affects the rheology of the paste at early ages. It reduces the workability of the paste and hinders the homogeneous mixing of cement with water. The first hydration products are the thermodynamically unstable calcium hydroaluminates, $C_2AH_8$ and $C_4AH_{13}$ (hexagonal phase), which evolve

rapidly to, without stabilizers and admixtures, to the $C_3AH_6$ phase (cubic phase) [Ramachandran1997; Manzano2009; Taylor1990]:

$$2C_3A+21H \rightarrow C_4AH_{13}+C_2AH_8 \quad (2.3)$$

$$C_4AH_{13}+C_2AH_8 \rightarrow 2C_3AH_6+9H \quad (2.4)$$

To avoid the *flash-setting*, retardants such as gypsum are added to the clinker. In the presence of gypsum, the products are calcium sulphoaluminates, mainly ettringite $C_6A\bar{S}H_{32}$:

$$C_3A+3C\bar{S}H_2+26H \rightarrow C_6A\bar{S}H_{32} \quad (2.5)$$

When there is no more gypsum available in solution, $C_3A$ starts to consume the created ettringite, and forms monosulphoaluminate, $C_4A\bar{S}H_{12}$, a crystalline phase richer in aluminium:

$$2C_3A+C_6A\bar{S}H_{32}+4H \rightarrow 3C_4A\bar{S}H_{12} \quad (2.6)$$

There is a controversy in the nature of the retardation mechanism. Some authors propose that the sulphoaluminate phases cover the $C_3A$ surface with a more or less impermeable layer that prevents the contact with the solution [Holly2006; Havlica1993; Collepardi1978], while others suggest that sulphate groups block the reactive points in the crystal surface [Brown1984; Minard2007].

**Aluminoferrite, $C_4AF$**

Hydration of the ferrite phase is very similar to the aluminate one. The main product is $C_4(A,F)H_{19}$, but evidences of amorphous iron oxides or hydroxides are found. In the presence of gypsum, the reaction products follow the same sequence as the one of $C_3A$, with the only difference that the hydration products (ettringite and monosulphoaluminate) present a partial substitution of aluminium by iron [Taylor1990].

The hydration process has been followed by many different techniques, like conductimetry, thermogravimetry, microscopies, NMR, X-Ray diffraction, etc [Ramachandran1997].

The recorder evidences from those studies agree that in the hydration of ordinary Portland cement, five different periods or stages can be distinguished [Kondo1969]. Those stages are easily differentiated monitoring the heat rate evolution during the

hydration, as can be seen in **Figure 2.5**. In this figure, the $Ca^{2+}$ ion concentration in solution is also shown.

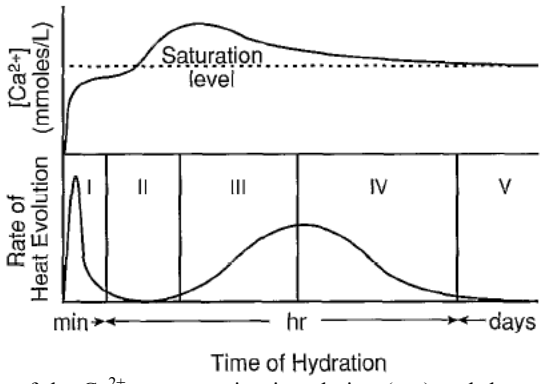


**Figure 2.5**: Idealized curves of the $Ca^{2+}$ concentration in solution (top) and the rate of heat evolution (bottom) versus the hydration time of ordinary Portland cement pastes. The stages are explained in the text. Time scale is logarithmic.

### I. Preinduction Period

When cement powder is put in contact with water, there is an initial fast dissolution of the clinker grains releasing $Si^{4+}$, $Ca^{2+}$ and $OH^-$ ions to solution. This stage lasts for a few minutes and is characterized by an elevated heat production. The concentration of $Si^{4+}$ ions reaches a maximum value and begins to reduce as the first C-S-H gel is formed. On the contrary, the concentration of $Ca^{2+}$ and $OH^-$ increases continuously, as the formed gel has a lower Ca/Si ratio than the clinker phases. As the saturation level of $Ca^{2+}$ and $OH^-$ ions in solution is not reached, portlandite does not precipitate. Therefore, the pH of solution increases. During this stage the first ettringite crystals appear due to $C_3A$ dissolution, or, if gypsum is not present, flash setting occurs [Manzano2009; Nelson1990].

### II. Induction Period

The reactions slow down and the paste remains plastic-workable for a few hours. There are different theories which attribute the decrease in the hydration rate to different reasons. Some authors suggest that the main cause is formation of an impermeable layer [Brown1984; Jennings1986], for others the slow nucleation of portlandite [Wu1984] and the C-S-H gel [Odler1979] due to the low concentration of ions in solution controls this stage. $[Ca^{2+}]$ and $[OH^-]$ increase over the saturation level, when portlandite begins to

precipitate. At the end of this stage the pH is ~12-13 [Manzano2009; Nelson1990].

**III. Acceleration Period**

The precipitation of portlandite decreases the concentration of $Ca^{2+}$ and $OH^-$ in the liquid phase. Thus, the dissolution of calcium silicates and aluminates is accelerated again, with the consequent increase in the released heat. A second stage C-S-H gel is formed, while portlandite and ettringite continue growing. The C-S-H gel formed on the surface of adjacent clinker particles coalesces. This point, known as the cohesion point, matches with the maximum heat release, and corresponds to the setting period end [Nelson1990].

**IV. Deceleration Period**

After several hours of reaction, the hydration products cover the cement grain surfaces, and the kinetics is no longer controlled by the dissolution rate or crystal nucleation and growth, but rather by the diffusion of calcium and silicate ions through the already formed produtcs. Therefore, the reaction slows down as more hydration products are formed. Due to the consumption of sulphate ions, ettringite evolves to monosulphoaluminate, what can produce a shoulder on the heat evolution curve [Manzano2009; Nelson1990].

**V. Diffusion Period**

In this stage the microstructure of the C-S-H gel is developed, and the gel becomes denser. Other crystalline species, especially portlandite and monosulphoaluminate, could keep growing. As a consequence, the diffusion of the solution becomes smaller and reactions slow down as the paste becomes stronger. It is considered that the hydration is virtually finished after one year, though the process could continue over years, as well as the evolution of the C-S-H gel and cement paste microstructure [Manzano2009; Nelson1990].

**Superplasticizers**

In cement chemistry are frequently used chemical admixtures: an admixture, defined as a material other than water, aggregate, hydraulic cement, and fiber reinforcement, is used as an ingredient of concrete or mortar, and added to the batch immediately before or during its mixing. Chemical admixtures are water soluble or emulsified systems and include accelerators, retarders, water reducers, superplasticizers, etc.

Significant advances have particularly been made in the production and application of superplasticizers.

Superplasticizers (SPs) belong to a class of water reducers chemically different from the normal water reducers and capable of reducing water contents by about 30%. They were first introduced in Japan in the late 60's and in Germany in early 70's. In North America they were used from 1974.

The advantages derived by the use of SPs include production of concrete having high workability for easy placement, and production of high strength concrete with normal workability but with a lower water content

The most important property of a SPs is its ability of dispersing the cement particles. Electron microscopic examination reveals that in water suspensions of cement, large irregular agglomerates of cement particles form. By the addition of a SPs, the material is dispersed into small particles.

The fluidizing effect on cement is illustrated in **Figure 2.6**.

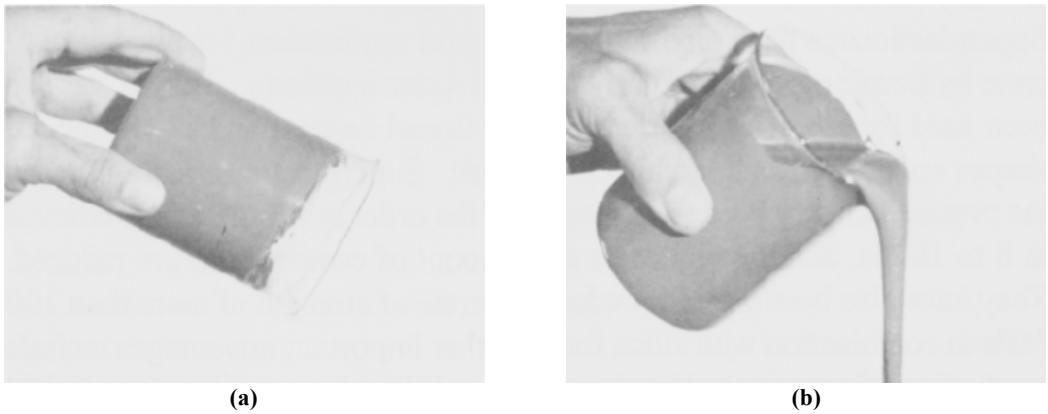

**(a)** **(b)**

**Figure 2.6**: Effect of SP on cement: **(a)** cement + water, **(b)** cement + water + SP [Ramachandran1997].

The fluidifying effect of the SP may be envisaged as follows. Portland cement in contact with water has a tendency to flocculate due to van der Waals' forces, electrostatic interactions between the opposite charges and surface chemical interactions between the hydrating particles.

This will result in the formation of an agglomeration of particles with open structure with spaces that entrain water molecules. These water molecules are not immediately available for hydration and do not have a lubricating effect. In the presence of a SP, deflocculation or dispersion of cement particles occurs due to adsorption and electrostatic repulsion. This process does not allow the formation of entrapped water and discourages surface interaction of the particles. Some stearic hindrance is possible especially when high molecular weight SPs are used. Such a phenomenon would also prevent particle-particle interactions [Ramachandran1997; Zingg2008].

Superplasticized concrete enables placement in congested reinforcement and in not easily accessible areas. Easy and quick placement characteristics of flowing concrete and the need for only very nominal vibration makes it suitable for placement in bay areas, floors, foundation slabs, bridges, pavements, roof decks, etc. Pumping of concrete is very much facilitated by incorporation of SPs.

SPs have also found successful applications for placing concrete by tremie pipe, particularly in underwater locations; they have been used also for spray applications, for tunnel linings and where special shapes are desired as in architectural work.

Other important advantages include production of concrete with reduced permeability, improved surface finish, reduced shrinkage, and overall cost savings.

In addition to producing high strengths and flowable concretes, SPs offer other possible benefits. There is a great need to use marginal quality cements and aggregates for production of concrete. In such instances, the use of superplasticizers permits production of concrete at low w/c ratios and with good durability characteristics. SPs can be used advantageously in the production of fly ash concrete, blast furnace slag cement concrete, composites with various types of fibers and lightweight concrete [Ramachandran1997].

Among the first generation SPs are sulphonated naphthalene–formaldehyde condensates, sulphonated melamin–formaldehyde condensates and modified lignosulphonates; the new generation products with enhanced properties are based on comb-shaped polycarboxylate-ether-based polymers (PCEs) [Winnefeld2007].

Their dispersing effect is due to the adsorption of polymers on particle surfaces and evocation of electrostatic and/or steric repulsive forces; those mechanisms can be derived from theories of colloidal sciences.

The addition of superplasticizers impacts the interface between particle surface and the pore solution and influences physical properties such as viscosity and yield stress of the cement paste. The structure is illustrated in **Figure 2.7**.

The adsorption behaviour depends on the PCE architectures. The molecules are comb-shaped, consisting of methacrylic acid copolymer (backbone) with hydrophilic polyethylene-oxide copolymers (PEO) side chains. Both parameters, side chain length and density, can be varied in order to take control of the adsorption behaviour and dispersion ability. By changing PCE architecture and dosage, workability properties and prolongation of the dormant period can be controlled [Zingg2009].

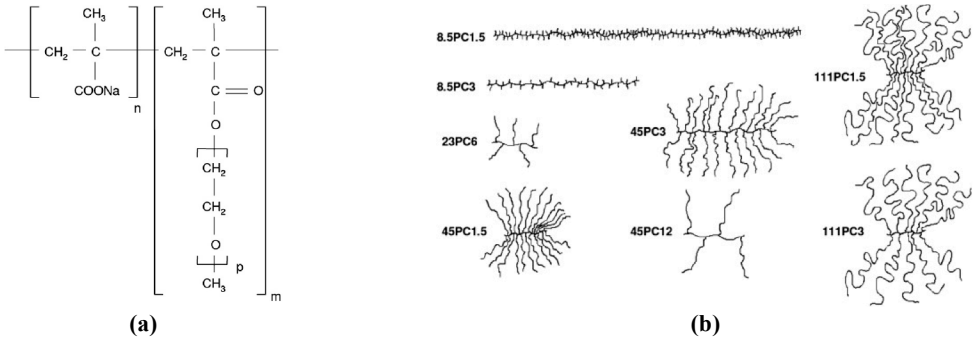


**Figure 2.7**: **(a)** Chemical structure of a general PCE; **(b)** schematic representation of *n*PCE*p* architecture. The first number in the name of SP, here called *p*, refers to the number of PEO units (side chain length), while the second one, *n*, refers to the number of anionic functional groups [Ferrari2011].

Although the influence of PCE on cementitious systems has been extensively investigated many questions remain unsolved concerning the influence on the early microstructural development, the nucleation and growth of hydrate phases, the dissolution of clinker phases, the admixture adsorption behaviour, and the interparticle forces. Due to the complexity of this multimineral system, the influence of superplasticizers has been increasingly investigated on simplified systems (pure clinker and hydrate phases) over the last decades. However, the possibility of simplification is limited if one wants to obtain relevant results, because of the complex chemical processes involved in cement suspensions. [Winnefeld2007; Zingg2008; Zingg2009].

It is of fundamental importance to understand the dynamics of these polymers in proximity of cement particles, because their conformation can affect the rheology: in particular, how these polymers are arranged in contact with the surface of cement particles, how does it change the flexibility of the pendant near the surface and what types of cement surfaces interact better with the PCEs [Lange2012].

**Computational simulation in cement research**

Many efforts have been devoted, over the last decades, to develop mathematical models for understanding and predicting cement hydration kinetics and microstructure development and how they are influenced by the action of PCEs [Thomas2011]. An accurate approach to the simulation of cement hydration would provide a tool for predicting the performance of concrete and designing novel cementitious materials. Despite significant effort and progress, the degree of accuracy of such simulations is still limited, mainly because of the underlying complexity and multi-scale nature of cement hydration and microstructural development.

In particular, atomistic simulations are the only reliable computational methods for describing the details of the interaction between cement and PCE. In principle, any chemical reaction or physical-chemical property of a material can be modeled in terms of modification in the atomic configuration of the system. These methods can provide important information regarding spectroscopic and mechanical properties, diffusion and transport related properties, conformational and energy analysis.

The application of molecular models to the study of cementitious systems is a relatively new field, which complement numerical models performed at larger scales [Parrot1984; vanBreugel1995; Bentz1997; Bullard2007; Bishnoi2009; Valentini2014] or based on nucleation and growth kinetic models [Thomas2007; Ridi2012; Scherer2012] or CG approaches [Lee1998, Anderson2005, Knouert2007, Suter2009].

The above methods, in fact, require, to varying degrees, input consisting of thermochemical data and kinetic parameters, as well as physical and structural properties of the constituent materials; these quantities can be obtained either from experiments or by evaluation using molecular-scale techniques: QM simulations, e.g. *ab initio* methods, and classical molecular mechanics simulations (MM), e.g. MC and MD simulations.

Molecular Modeling studies to date have been primarily focused on the structural properties of the cementitious phases, rather than on the intrinsic kinetic aspects of cement hydration: accurate structural information generated from these studies can be a valuable input for the kinetic models [Dolado2011, Thomas2011].

Most of previous MD computational studies, on cement components and hydration processes were focused on a small part of the system. Sanchez (2008) reported about

MD simulations of the interfacial interaction between surfaces functionalized graphitic structures and 9 Å tobermorite, a common model for C–S–H phases [Sanchez2008]. Pellenq proposed a molecular model of C-S-H based on a bottom-up atomistic simulation approach that considers the chemical specificity of the systems [Pellenq2009]. Wu and his collaborators proposed a molecular dynamics approach to calculate elastic properties (specifically bulk, shear, Young's moduli, and Poisson's ratios) of cement constituents alite, belite, aluminate mineral crystal [Wu2011].

In 2011, Manzano and coworkers used a combination of classical and quantum mechanical simulation methods to study the detailed physicochemical changes of the clinker phases alite and belite [Manzano2011].

In 2012, Durgun [Durgun2012] used DFT calculations to understand the reactivity of calcium silicate phases, but his system was very far from the real phases involved in the cement hydration process. Combining DFT calculations and experimental data, Liu set up [Liu2012] a reactive force field for ettringite and studied its properties from reactive dynamics simulations. Yoon and Monteiro studied the molecular structure and dynamics of interlayer water of 14 Å tobermorite via MD simulations [Yoon2013]. More recently, Hou used molecular simulations to study the mechanical properties of C-S-H gels under tensile loading [Hou2014] and Durgun and coworkers made an extensive surface analysis of synthetic calcium silicate phases ($C_3S$ and $C_2S$) using first-principles computational methods [Durgun2014].

Our main objective in this PhD work is to address the feasibility of *in silico* studies of the influence of PCE superplasticizers on the evolution of cement suspensions during early hydration, based on MD approaches: pratically, we want to understand the dynamics of these polymers in proximity of cement surfaces, because nowadays there is still no clear idea of the conformation after adsorption.

To clarify the dynamic of these systems, some theoretical models were proposed. De Gennes quantitatively described the interactions between polymers and generic surfaces; Gay and Raphael (2001) developed a novel method for the characterization of comb-polymers based on the free energy approach of Flory; Flatt et al. (2009) adapted the approach of Gay-Raphael to the description of the adsorption of PCEs on C-S-H in terms of hydrodynamic radius surface coating thickness, obtaining an excellent agreement with atomic force microscopy measurements [DeGennes1987; Gay2001; Flatt2009].

All these methods provide a quantitative description of the conformations of polymers in solution or at particle interfaces. However, these models could not be expected to provide very accurate numerical predictions, because they were derived using a scaling law approach. An alternative to the use of approaches based on parameters determined by experimental data is the use of *ab initio* molecular simulations, but in this case the number of atoms involved would be too small.

# MD PROTOCOL APPLIED TO THE SYSTEMS PCE-$C_3A$/PCE-$C_3S$

**Objective**

In this paper I present the results of four MD simulations of a system consisting of the PCE-(23-7-1), a comb-shaped polymer unit model SP, the $C_3A$ and $C_3S$ surfaces, explicit water, $Ca^{2+}$ and $OH^-$ ions (pore solution); the polymer, with an elongated shape had the backbone perpendicular to the surface and the polymer with folded shape had the backbone parallel to the surface.

From MD trajectories we calculated conformational properties, radius of gyration (RG), end to end distance (ETE), the Center of mass trajectory (CM) and the structure and dynamics of Al/Ca/O/Si atoms layers present in the surfaces considered, computing the mobility of these atoms along the principal spatial directions by one-dimensional density profile (1D-DP).

**Simulation Setup**

We set up and validated a MD protocol, composed by several steps, for the following four systems:

MD1: $C_3A$+ PCE-(23-7-1) (elongated conformation) + $7Ca^{2+}$ + $14OH^-$ + $H_2O$.

MD2: $C_3A$ + PCE-(23-7-1) (folded conformation) + $7Ca^{2+}$ + $14OH^-$ + $H_2O$.

MD3: $C_3S$ + PCE-(23-7-1) (elongated conformation) + $22Ca^{2+}$ + $44OH^-$ + $H_2O$.

MD4: $C_3S$ + PCE-(23-7-1) (folded conformation) + $22Ca^{2+}$ + $44OH^-$ + $H_2O$.

These systems were constructed so as to maintain electroneutrality.

The protocol is described for MD1, in details, in the following.

Initially was built the PCE-(23-7-1), in **Figure 3.1 (c)**, a comb-shaped system consisting of six methacrylic acid copolymers (backbone) with twenty three grafted methyl-polyethylene-glycole copolymers (one side chain). To determine the structural stability, the system was optimized *in vacuo* by the *steepest descent algorithm* [Plimpton1995]; this technique is robust and is used generally when the structure is far from the minimum configuration.

A 6***a***×6***b***×4***c*** molecular supercell crystal model was built from the crystal structure determined by Steele [Steele1929], in **Figure 3.2**. The experimental cubic unit cell $C_3A$ parameters for ***a***, ***b*** and ***c*** are 7.624 Å. The experimental monoclinic unit cell $C_3S$ parameters for ***a***, ***b***, ***c*** are 12.235 Å, 7.073 Å, 9.298 Å; the height ***h*** of unit cell is 8.335 Å [Mumme1995].

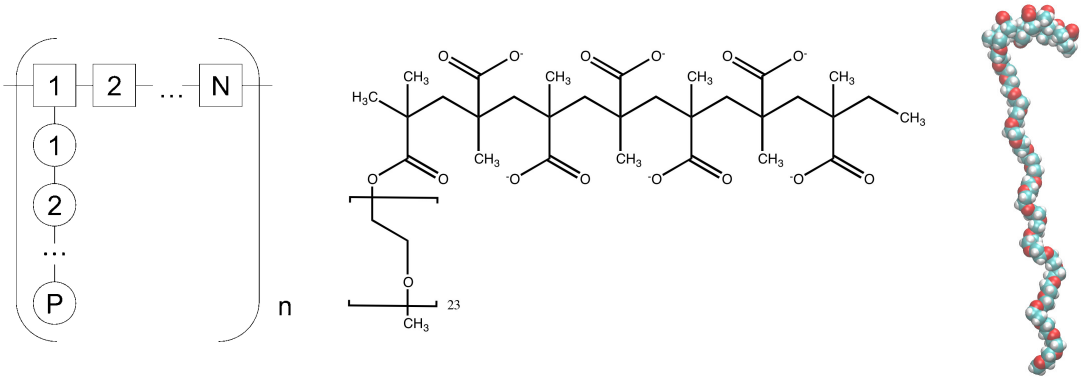


**(a)** **(b)** **(c)**

**Figure 3.1**: **(a)** Schematic representation of the comb-shaped polymer PCE-(P-N-n) considered. The polymer contains *n* segments, each with *N* back bone units, one side chain, and each side chain contains *P* monomers. **(b)** Chemical structure of PCE-(23-7-1). **(c)** vdW representation of the polymerstudied via MD simulations. Backbone length: 16 Å; side chain length: 54 Å. The different colors correspond to different atom types: H=white, O=red, C=cyan.

The supercell was contained in a box of dimensions 6***a***×6***b***×4***c*** $Å^3$. In analogy to the case of the PCE polymer, structural stability *in vacuo* was determined by a pre-optimization via *steepest descent method* [Plimpton1995].

Water molecules (in order to obtain a water density equal to 1g/ml) and $Na^+$, PCE counterions, at the correct concentrations, were added to the polymer structure obtained at the end of step (1) and the supercell obtained at the end of step (2), resulting in a large box with volume 6***a***×6***b***×(4***c***+*l*) $Å^3$, where *l* was determined by the amount of water added to the system. These operations were carried out using the Packmol software [Martínez2009]. The values used of the ionic concentrations for the pore solution are $[Ca^{2+}]$=50 mmol/L and $[OH^-]$=100 mmol/L, which are close to the maximum concentrations, in normal hydration conditions, at the transition between the induction period and acceleration [Bullard2008].

The MD simulation was performed in the NVT conditions (constant number of particles, volume and temperature), enforcing three-dimensional periodic boundary conditions (PBC) and using a Nosé-Hoover Thermostat, pair list distance of 2 Å (pair list updated every 0.01 ps), time step of 1 fs, PME treatment of electrostatics

(accuracy of $1.0 \cdot 10^{-4}$), cutoff for vdW interactions at 10.5 Å [Ding1992]. The simulations consisted of two steps: i) Equilibration of the system, at 298.15 K, for 60 ns. ii) Run of the system, at 298.15 K, for 25 ns.

The Shake algorithm was used to constrain bonds and angles of water molecules during the simulation [Ryckaert1977]: no others kind of constrains were used inside the MD simulations.

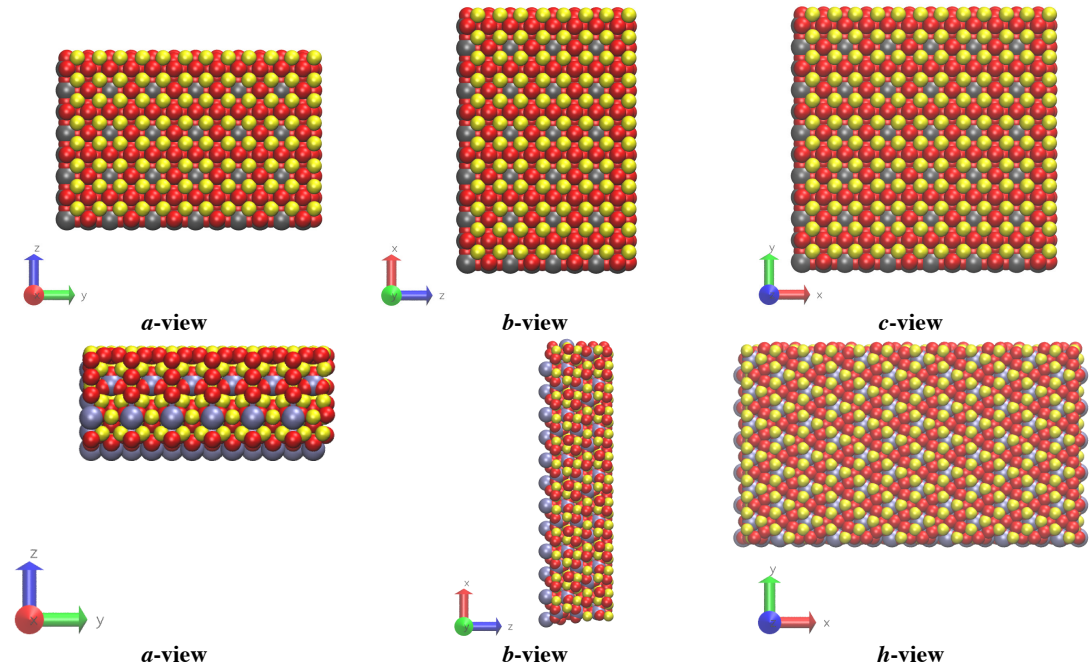


**Figure 3.2**: ***a***-, ***b***- and ***c***-view of the $C_3A$ and $C_3S$ supercells (vdW representation). On top MD1, MD2 surfaces (6***a***x6***b***x4***c***) and on the bottom MD3 and MD4 surfaces (6***a***x6***b***x4***h***). The different colors correspond to different atom types: O=red, Ca=yellow, Al=gray, Si=ice blue. The arrows indicate the axes of the inertial reference system.

All simulations were done using the LAMMPS software package [Plimpton1995], with over 2 hybrid computer nodes, allocating 16 CPU (AMD Opteron 6128 1.6 GHz) cores and 2 GPU (nVidia Tesla M2050) boards and they were run on the C3P high performance computing facility ("Comunità di Chimica Computazionale di Padova", http://www.chimica.unipd.it/c3p).

The initial configurations of the systems are the following in **Figure 3.3**.

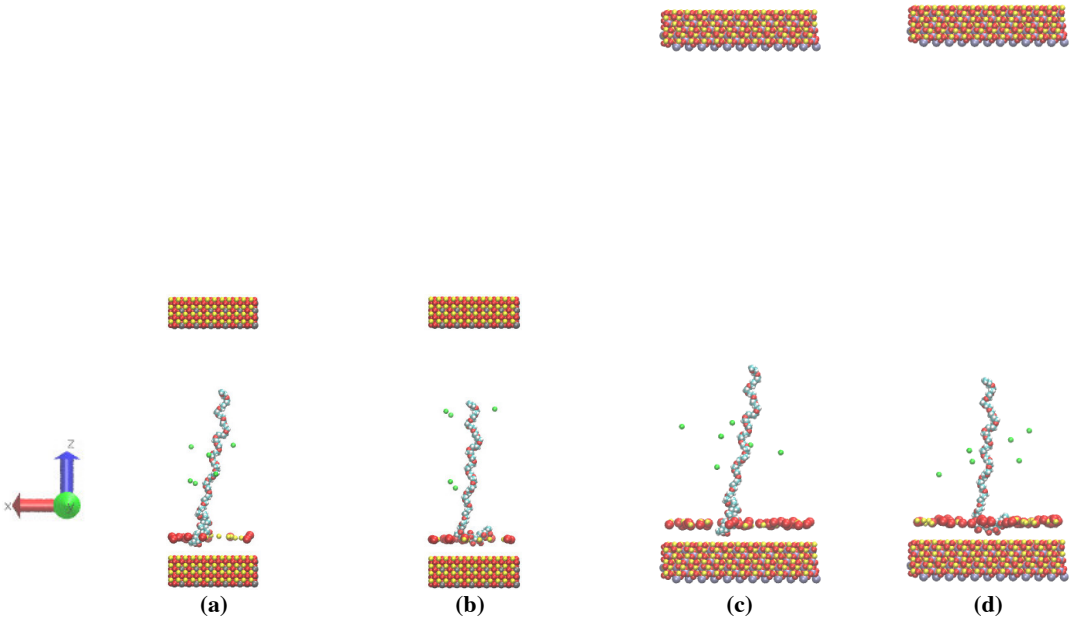


**Figure 3.3**: Initial configuration of **(a)** MD1, **(c)** MD3: polymer with side-chain and backbone perpendicular to the surface. **(b)** MD2, **(d)** MD4: side-chain perpendicular and backbone parallel to the surface. The different colors correspond to different atom types: H=white, O=red, C=cyan, Ca=yellow, Al=grey, Si=ice blue, Na=green, $OH^-$ ions=red balls (vdW representation).

The simulations data are listed in the following in **Table 3.2.**

| **System** | **MD1** | **MD2** | **MD3** | **MD4** |
|---|---|---|---|---|
| | PCE-(23-7-1) + 14 $Ca(OH)_2$ + $H_2O$ + $C_3A$ | | PCE-(23-7-1) + 22 $Ca(OH)_2$ + $H_2O$ + $C_3S$ | |
| **MD Box ($nm^3$)** | 6***a***x6***b***x(4***c***+$l_1$) | | 6***a***x6***b***x(4***h***+$l_2$) | |
| **PBC** | x, y, z axis | | | |
| **Ensemble** | NVT | | | |
| **Number of atoms** | 30211 | | 83077 | |
| **T (K)** | 298.15 | | | |
| **Thermostat** | Nosé-Hoover | | | |
| **Cut-Off (Å)** | 10.5 | | | |
| **PCE charge (e)** | -6 | | | |
| **System charge (e)** | 0 | | | |
| **Number of $H_2O$** | 8394 | | 24993 | |
| **Number of $Ca(OH)_2$** | 7 | | 22 | |
| **Number of $Na^+$** | 6 | | | |
| **Optimization** | Steepest Descent Method | | | |
| **Time step (fs)** | 1 | | | |
| **Dumping (ps)** | 1 | | | |
| **Equilibration time (ns)** | 60 | | | |
| **Production time (ns)** | 25 | | | |

**Table 3.2**: MD data: $l_1$=120 Å and $l_2$=240 Å are the height of water box of MD1, MD2 and MD3, MD4.

The FF parameters of the atoms simulated are in **Table 3.3** and **Table 3.4**.

**Force Field parametrization**

The interactions between the PCE polymer, water, atoms of surfaces, inorganic and hydroxyl ions were modeled using the Dreiding force field [Mayo1990], in combination with the ClayFF force field [Cygan2004], the TIP3P model for water molecules [Jorgensen1983] and the polarizable multi-state empirical valence bond model (MS-EVB) [Wick2009].

The Dreiding FF is a reasonable choice for predicting the structures of poorly characterized molecules, although it may lead to low accuracy for specialized subsets of molecules. Due to its general applicability, it is currently employed to predict or rationalize structures and dynamical properties of a variety of organic and inorganic molecules. This FF uses general force constants and geometry parameters based on simple hybridization rather than on individual force constants and geometric parameters that depend on the particular combination of atoms involved in the bond, angle or torsion terms. It follows that all bond distances are derived from atomic radii, and there is only one force constant for each bond, angle, and inversion. The vdW interactions are described by atomic monopoles and a screened (distance dependent) Coulomb interaction.

The potential energy is expressed as:

$$E_{total}^{Dreiding} = \frac{1}{2}k_e(R-R_0)^2 + \frac{1}{2}k_{i,j,k}(\theta_{i,j,k}-\theta_{0,j})^2 + \frac{1}{2}V_{j,k}\{1-cos[n_{j,k}(\varphi-\varphi_{0,jk})]\} + \\ + k_{inv}[1-cos(\psi)] + D_0[\rho^{-12}-\rho^{-6}] + 332.0637\left(\frac{Q_iQ_j}{\varepsilon R_{ij}}\right) \quad (3.1)$$

where $k_e$, $k_{i,j,k}$, $k_{inv}$ are the force constants for stretching, bending and inversion; $V_{j,k}$ is the barrier of rotation for dihedral angle torsion (always positive); $R_0$, $\theta_{0,j}$, $\varphi_{0,jk}$ and $\psi$ are, respectively, the equilibrium bond length, angle bend, dihedral angle and improper angle; $D_0$ is the vdW well depth; $\rho = R/R_0$ is the scaled distance; $R_0$ is the van der Waals bond length; $Q_i$ and $Q_j$ are charges in electron unit; ε is the dielectric permittivity; 332.0637 is a numeric constant which converts electrostatic energy, expressed as to kcal/mol [Mayo1990, Wu2011]. The partial charges derivation is explained in the next section.

The interaction parameters between unlike atoms were calculated, based on the arithmetic mean rule for the distance parameter $R_{0,ij}$ and the geometric mean rule for the energy parameter $D_{0,ij}$, as:

$$R_{0,ij} = (R_{0,ii} - R_{0,jj})/2 \tag{3.2}$$

$$D_{0,ij} = \sqrt{D_{0,ii} \cdot D_{0,jj}} \tag{3.3}$$

The atom type energy and distance parameters are given in **Table 3.3**.

| **Non bond Parameters** | | | | |
|---|---|---|---|---|
| **Species** | **Symbol** | $Q_i$ **(e)** | $D_{0,ii}$ **(Kcal/mol)** | $R_0$ **(Å)** |
| Hydrogen | H_ | RESP procedure | 0.0152 | 3.1950 |
| Carbon $sp^3$ | C_3 | | 0.0951 | 3.8983 |
| Carbon $sp^2$ | C_2 | | 0.0951 | 3.8983 |
| Oxygen $sp^3$ | O_3 | | 0.0957 | 3.4046 |
| Oxygen $sp^2$ | O_2 | | 0.0957 | 3.4046 |

| **Bond Parameters** | | | |
|---|---|---|---|
| **Bond stretch** | | | |
| **Species *i*** | **Species *j*** | $k_e$ **(Kcal/mol Å$^2$)** | $R_0$ **(Å)** |
| H_ | C_3 | 700 | 1.0900 |
| C_3 | C_3 | | 1.5300 |
| C_3 | C_2 | | 1.4300 |
| C_3 | O_3 | | 1.4200 |
| C_2 | O_3 | | 1.3200 |
| C_2 | O_2 | | 1.2200 |

| **Angle Bend** | | | | |
|---|---|---|---|---|
| **Species *i*** | **Species *j*** | **Species *k*** | $k_{i,j,k}$ **(Kcal/mol Å$^2$)/rad$^2$** | $\theta_0$ **(deg)** |
| X | C_3 | X | 100 | 109.47 |
| X | C_2 | X | | 120.00 |
| X | O_3 | X | | 104.51 |

| **Dihedral Angle** | | | | | | |
|---|---|---|---|---|---|---|
| **Species *i*** | **Species *j*** | **Species *i*** | **Species *k*** | $V_{i,k}$ **(Kcal/mol)** | ***d*** | ***N*** |
| X | C_3 | C_3 | X | 2.0 | -1 | 3 |
| X | C_3 | C_2 | X | 1.0 | -1 | 6 |
| X | C_2 | O_3 | X | 1.0 | -1 | 6 |
| X | C_2 | O_2 | X | 5.0 | -1 | 2 |
| X | C_3 | O_3 | X | 2.0 | -1 | 3 |

| **Improper Angle** | | | | | |
|---|---|---|---|---|---|
| **Species *i*** | **Species *j*** | **Species *i*** | **Species *j*** | $k_{inv}$ **(Kcal/mol)/rad$^2$** | $\omega_0$ **(rad)** |
| C_2 | X | C_2 | X | C_2 | X |

**Table 3.3**: Parameters of Dreiding FF [Mayo1991].

ClayFF is a suitable force field for MD simulations of hydrated and multicomponent mineral systems and their interfaces with aqueous solutions. The molecular modeling of real interfaces requires the description of complex and incompletely or poorly characterized crystal structures, low symmetries, large unit cells, variable compositions, complex and variable interlayers and interfaces. The numerous parameters of a bonded FF are not easily transferred from relatively simple and well-known structures to systems with complex and ill defined bond structures. For such systems, the application of a bonded force field is problematic because it can easily lead to significant over-parameterization, due to lack of experimental data needed to univocally determine all the force field parameters necessary to describe bonded interactions [Cygan2004].

ClayFF is based on an ionic-covalent description of metal-oxygen interactions associated with hydrated phases. All the atoms are represented as point charges with complete unconstrained translational motion within this force field framework. Metal-oxygen interactions are based on a simple 12-6 Lennard Jones (LJ) potential combined with Coulomb interactions. The empirical parameters are optimized using known mineral structures. Partial atomic charges are obtained from cluster and periodic density functional theory, quantum chemical calculations of simple oxide, hydroxide and oxy-hydroxide model compounds with well-defined structures. Oxygen and hydroxyl charges vary depending on their occurrence in water molecules, hydroxyl groups, bridges and substitution environments. Harmonic terms are included to describe the bond stretch and bond angle (three-body) bend terms associated with hydroxyls [Shahsavari2011].

The potential energy is expressed as:

$$E_{total}^{ClayFF} = \frac{e^2}{4\pi\varepsilon_0}\sum_{i\neq j}\frac{q_i q_j}{r_{ij}} + \sum_{i\neq j} D_{0,ij}\left[\left(\frac{R_{0,ij}}{r_{ij}}\right)^{12} - 2\left(\frac{R_{0,ij}}{r_{ij}}\right)^{6}\right] \quad (3.4)$$

where $q_i$ and $q_j$ are partial charges derived from quantum mechanics calculations, $e$ is the charge of the electron, $\varepsilon_0$ is the dielectric permittivity of vacuum; $D_{0,ij}$ and $R_{0,ij}$ are empirical parameters derived from fitting the model to observed structural and physical properties [Cygan2004]. The partial charges, the atom type energy and distance parameters are given in **Table 3.4**.

| **Nonbond Parameters** | | | | |
|---|---|---|---|---|
| **Species** | **Symbol** | $q_i$ **(e)** | $D_{0,ii}$ **(Kcal/mol)** | $R_0$ **(Å)** |
| Bridging oxygen | ob | -1.0500 | 0.1554 | 3.5532 |
| Octahedral aluminium | ao | 1.5750 | 0.0000013298 | 4.7943 |
| Tetrahedral silicon | st | 2.0000 | 0.0000018405 | 3.7064 |
| Hydroxide calcium | cah | 1.0500 | 0.0000050298 | 6.2484 |
| Aqueous sodium ion | Na | 1.0000 | 0.1301 | 2.6378 |
| Aqueous calcium ion | Ca | 2.0000 | 0.1000 | 3.2237 |

**Table 3.4**: Parameters of ClayFF [Cygan2004].

The interaction parameters between unlike atoms were calculated, based on the arithmetic mean rule for the distance parameter $R_0$ and the geometric mean rule for the energy parameter $D_0$ like in equations (3.2) and (3.3).

The three-site transferrable intermolecular potential (TIP3P) model have three interaction points corresponding to the three atoms of the water molecule. Each site

has a point charge, and the site corresponding to the oxygen atom also has the LJ parameters.

The potential energy is expressed as:

$$E_{total}^{TIP3P} = \sum_{i \neq j} \frac{q_i q_j e^2}{r_{ij}} + \frac{A}{r_{OO}^{12}} - \frac{B}{r_{OO}^{6}} \tag{3.5}$$

where the parameter are chosen to yield reasonable structural and energetic results for gas phase complexes of water and alcohols and for liquid water; in particular $q_H$=+0.417, $q_O$=-0.834, $A$=0.582 Kcal Å$^{12}$/mol, $B$=595 Kcal Å$^6$/mol, $r_{OH}$=0.9572 Å, angle HOH 104.52 deg [Jorgensen1983].

The $OH^-$ anions were modeled by creating a new sphere-like atom type in which the diameter equals the distance between oxygen and hydrogen, the charge is set to -1.0 and the LJ parameters are those described in the MS-EVB potential: the energy parameter is equal to 0.185 Kcal/mol an the distance parameter is 3.52 Å [Wick2009].

**Partial charges parametrization**

MM methods are a standard tool for the study of the structure and conformational energy and of non-covalent molecular interactions. The accurate calculation of these properties requires an adequate FF model. An optimal FF is characterized by accurate and sufficiently specific parameters, especially torsional parameters that are important for describing the geometry and conformational energy. Other relevant factors include parameter transferability and, especially, accurate treatment of electrostatic interactions for correctly describing the intermolecular energies.

Different FF are characterized by different methods for handling electrostatic interactions, based e.g. on the calculation of atomic charges by heuristic algorithms that are based on electronegativity (e.g., MMFF), or on the empirical determination of charge based on fitting to liquid properties (structure, vaporization and sublimation enthalpy) [Wang2000].

An optimal methodology for the calculation of electrostatic interactions, at least for FF relevant to organic molecules, is the Restrained Electrostatic Potential procedure (RESP) introduced by Bayly et al. [Bayly1993], which has an excellent performance in reproducing interaction energies and energies of solvation. The RESP model is based on a least-squares fit of the charges to the electrostatic surface potential (ESP),

with the addition of hyperbolic constraints on charges on non-hydrogen atoms. These constraints allow the reduction of charges on atoms that are poorly defined by the electrostatic potential, such as buried carbons. The final RESP model requires a two-stage fit, with the second stage needed to fit methyl- and methylene- groups, which in turn require equivalent charges on geminal hydrogen atoms that are not equivalent [Cornell1993, Cornell1995, Duan2003, Stendardo2010]. The RESP procedure is given in **Figure 3.4**.

An essential component of this procedure is that these pairwise charges are generated from gas phase *ab initio* calculations, but are designed to reproduce solution phase charge interactions. The charge derivation is also designed around the concept that a molecule is expected to have an integer charge. Moreover, this method is only applicable to small molecules (e.g. amino acids, monomers) due to poor convergence in larger system.

Therefore, we applied the RESP method to the monomers, ensuring that the total charge of the polymer was integer. Ideally, monomers should be reasonably small so as to reduce the chances of artifacts related to the QM calculations, to avoid that the RESP fits remained blocked in high energy minima.

We fully optimized all monomers geometries *in vacuo* at B3LYP/6-311G(D,P) level of theory as implemented in the software Gaussian [Gaussian]; to generate the electrostatic potential we made HF/6-31G* QM calculations: conveniently the errors in these calculations were close to the difference between the charge distributions in the gas phase and in solution [Kollman2006].

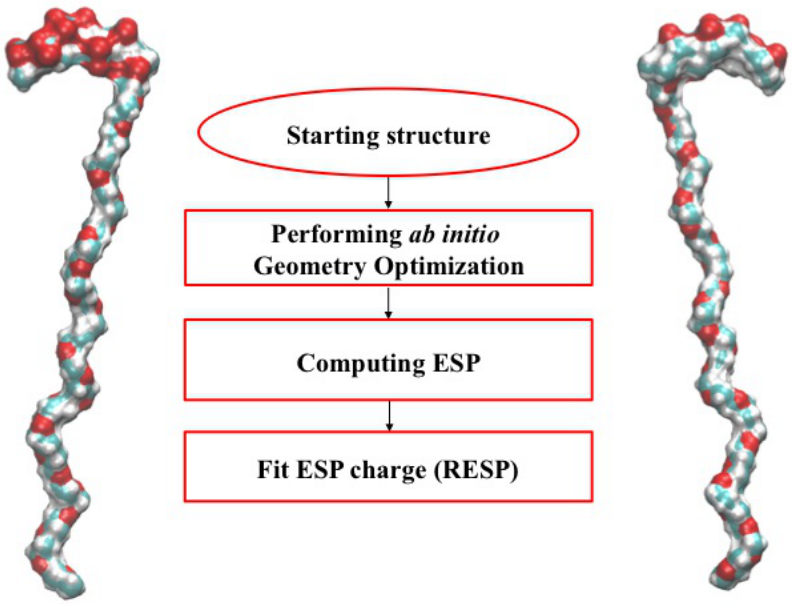


**Figure 3.4**: Protocol to calculate partial charges.

**Analysis, results and discussions**

The trajectories were analyzed with the VMD software [Humphrey1996], by determining the instantaneous RG and the ETE of the polymer, with the aim of understanding the structure flexibility and conformation in the presence of ions in solution and of a $C_3A$ or $C_3S$ surface. The RG of the polymer was computed, in **Figure 3.5 (a)**, along the entire simulation, by the following equation:

$$RG = \sqrt{\sum_{i}^{N} m_i (r_i - r_{cm})^2 \Big/ M} \qquad (3.6)$$

where $N$ is the number of C $sp^3$ of the backbone and side-chain, $r_i$ and $m_i$ are respectively the position and the mass of *i-th* C atom, $M$ is the total mass of the group, $r_{cm}$ is the center of mass position of the polymer, in **Figure 3.6 (a)**; we also calculated the RG graph distribution, in **Figure 3.6 (b)**, to show the most likely values.

**(a)** **(b)** **(c)** **(d)**

**Figure 3.5**: vdW representation of atoms considered to analyze the conformation of PCE-(23-7-1): RG **(a)**, ETE **(b)**, ETE of backbone **(c)** and ETE of pendant **(d)**, along the four MD simulations.

The ETE of the polymer, corresponding to the vector that points from one end of the polymer to the other end, was computed, in **Figure 3.7 (a)**, along the entire simulation, by the following equation:

$$ETE = \sqrt{(x_{first} - x_{last})^2 + (y_{first} - y_{last})^2 + (z_{first} - z_{last})^2} \qquad (3.7)$$

where $x_{first}$, $y_{first}$, $z_{first}$ were the cartesian coordinates of the first C atom of the polymer backbone considered and where $x_{last}$, $y_{last}$, $z_{last}$ were the cartesian coordinates

of the last C atom of the polymer side-chain considered, as shown in **Figure 3.5 (b)**. The distribution graph relative to the ETE distance is displayed in **Figure 3.7 (b)**.

It was computed the ETE of the polymer backbone and side-chain, as shown in **Figure 3.8 (a)** and **Figure 3.9 (a)**, to quantitatively determine what was the component more or less flexible; the atoms considered are showed on **Figure 3.5 (c)** and **(d).** The graph distributions are in **Figure 3.8 (b)** and **Figure 3.9 (b).**

From the analysis of RG and ETE, it was observed that in MD1 simulation, the polymer was more flexible compared to the others. This could be attributed to the fact that PCE-(23-7-1) did not remain attached to the surface and therefore had a higher mobility; furthermore the mobility of the polymer was due primarily to the dynamics of the side-chain.

It was calculated the average value of ETE for MD1, MD2, MD3, from 60 to 85 ns. The data are listed in **Table 3.5**: when the polymer remained attached to the surface, had a more compressed confomation. The PCE, in MD1, was the longest and the most flexible: it did not stay close to the surface and therefore had higher mobility.

| | **MD1** | **MD2** | **MD3** | **MD4** |
|---|---|---|---|---|
| **<ETE> (Å)** | 31.1±8.6 | 17.6±3.8 | 18.3±3.9 | 14.1±4.6 |
| **$<ETE_{backbone}>$ (Å)** | 14.8±0.8 | 13.8±0.7 | 13.6±0.4 | 11.1±0.7 |
| **$<ETE_{pendant}>$ (Å)** | 17.8±8.4 | 13.3±2.7 | 10.8±3.8 | 9.9±5.5 |

**Table 3.5**: Average value of ETE for MD1, MD2, MD3 and MD4.

It was calculated the trajectory of the CM of the polymer, in **Figure 3.10**, to understand its mobility away from the surface.

From the analysis of CM dynamics, after the equilibration, it was observed that only the polymer in MD1 moved away from the surface; in all others situations the polymer was close to the surface. The reasons may be the combination of two factors: starting configuration of the PCE and most attractive force of $C_3S$ respectly $C_3A$.

In MD1 (the backbone was perpendicular to the $C_3A$ surface), just one methacrylate unit was close to the surface and the electrostatic interaction attractive polymer-surface was smaller. In MD2 (the backbone was parallel to the $C_3A$ surface), all six methacrylate units were close to the surface and the electrostatic interaction attractive polymer-surface was bigger. In MD3 (the backbone was perpendicular to the $C_3S$ surface), just one methacrylate unit was close to the surface and the electrostatic interaction attractive polymer-surface was bigger. In MD4 (the

backbone was parallel to the $C_3S$ surface), all six methacrylate units were close to the surface and the electrostatic interaction attractive polymer-surface was bigger.
The starting configurations of backbones are given in Figure 3.11.

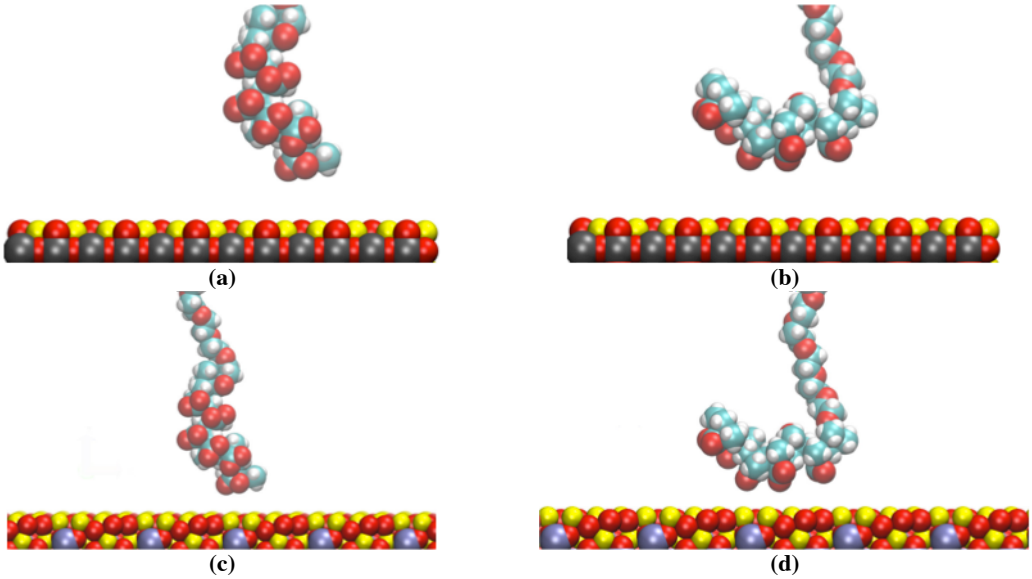


**Figure 3.11**: Starting configurations of backbones of (a) MD1, (b) MD2, (c) MD3 and (d) MD4.

It was determined the mobility of surface atoms Ca/Al/O and Ca/Si/O along the spatial directions (x-, y- and z-axis) with the aim of understanding whether ClayFF correctly modeled the dynamics of $C_3A$ and $C_3S$ atoms: it was calculated the one-dimensional density profile (1D-DP) of these atoms, i.e. the number of atoms per unit volume computed for the axial directions. The origin (z = 0) was defined as the plane where the surface was placed.
In **Figure 3.12**, the details of how it was calculated 1D-DP along z-axis.

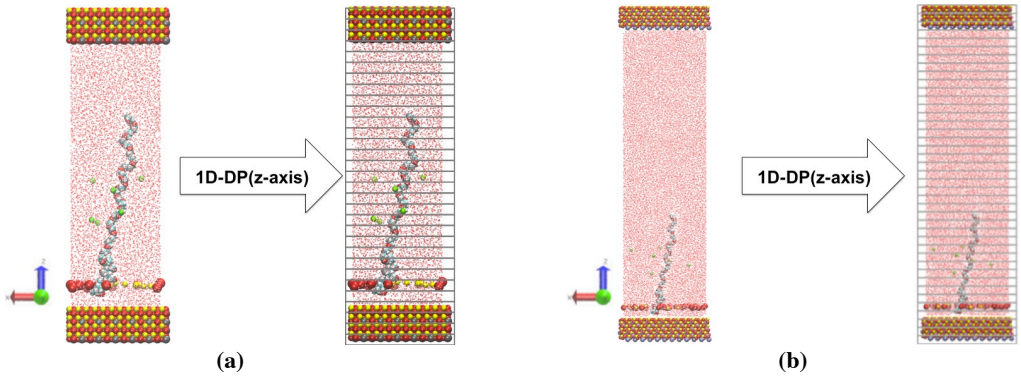


**Figure 3.12**: Example of how it was calculated the one-dimensional density profile along the z-axis, for **(a)** $C_3A$ and for **(b)** $C_3S$.

The results are in **Figure 3.13** to **3.15,** MD1 on the left and MD3 on the right; analogous results are valid for MD2 and MD4. From the analysis of the graphs, it

was noted which the densities of atoms in the various layers, after an initial relaxation phase of the systems, caused by the force field, even at long times remained approximately constant: both at the end of equilibration that at the end of the dynamics, the density profiles of the different types of atoms were approximately constant

Although some atoms moved into the solution, most of them possessed a vibrational motion isostropic along the three spatial directions.

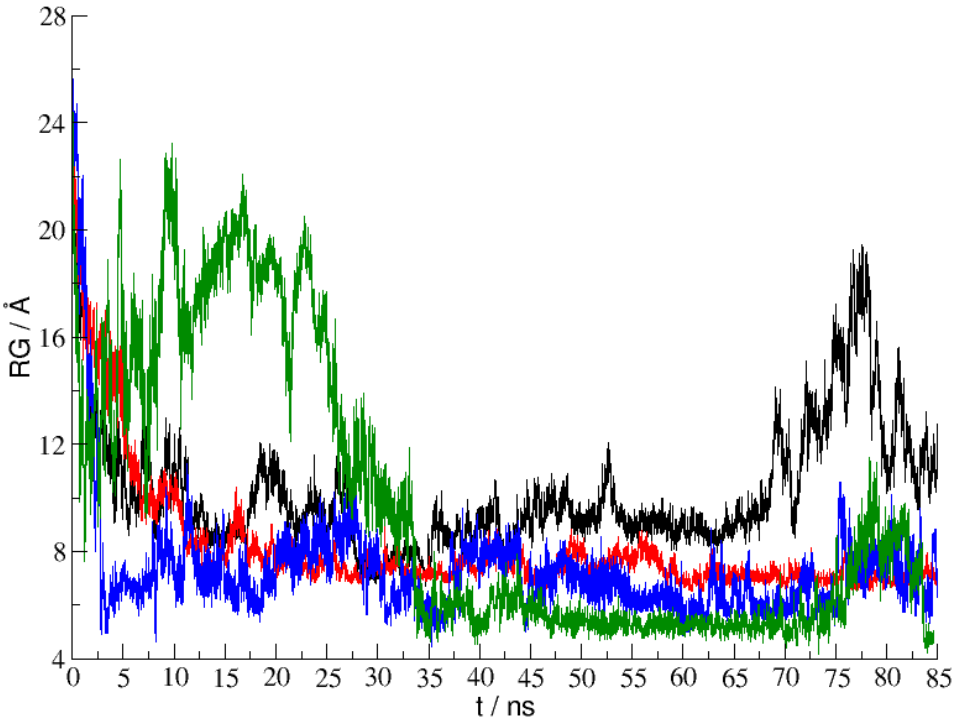


**(a)**

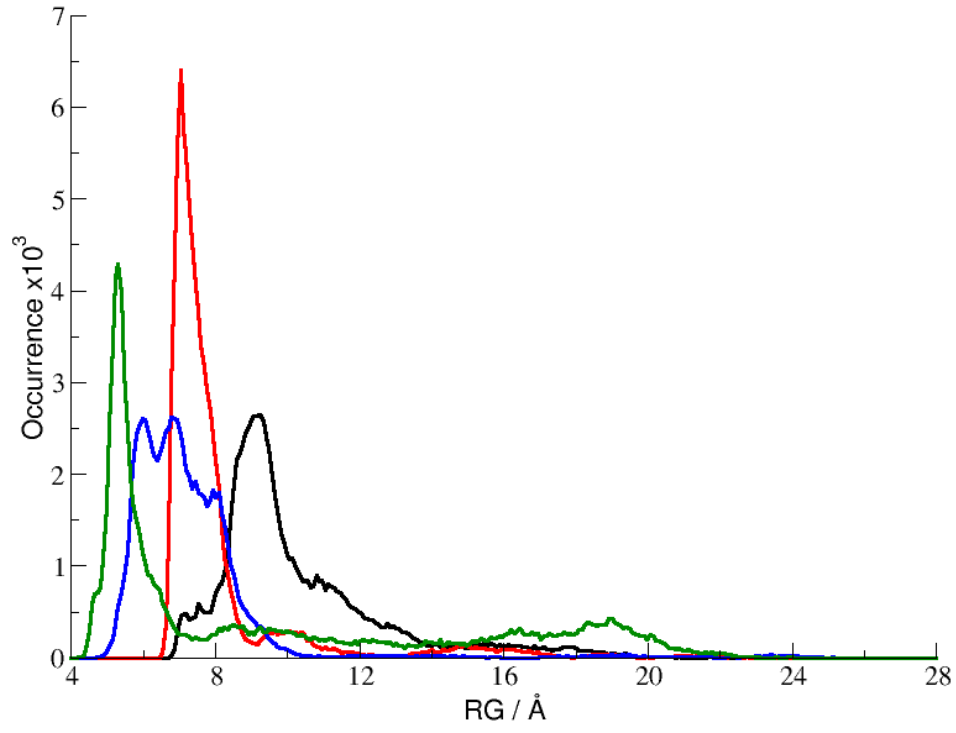


**(b)**

**Figure 3.6**: **(a)** Time series and **(b)** distributions relative to the radius of gyration of the PCE-(23-7-1), computed along the simulations, for MD1 (black line), MD2 (red line), MD3 (blue line) and MD4 (green line).

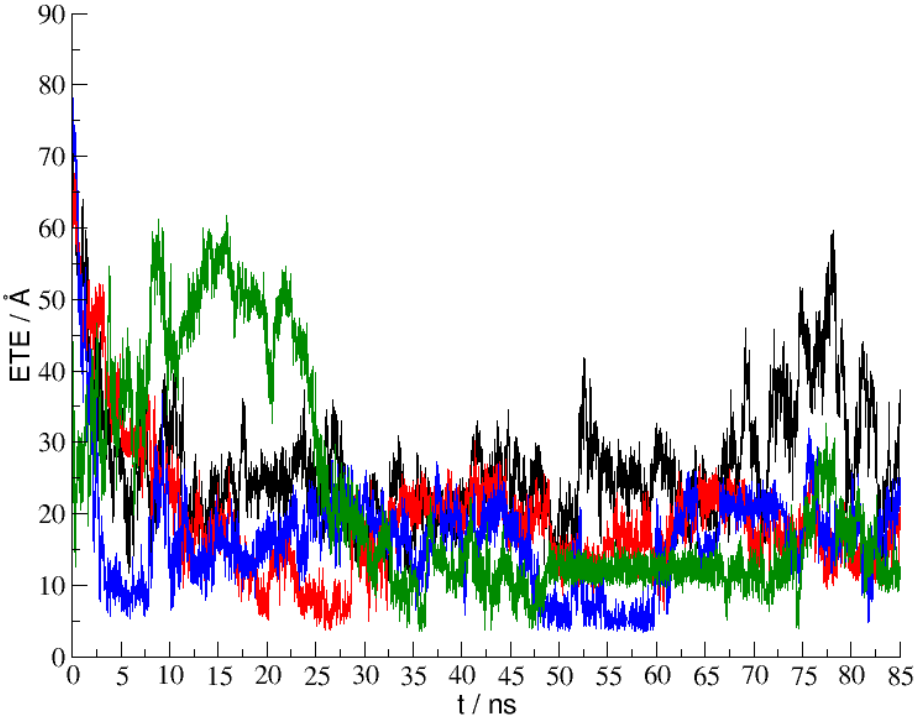


**(a)**

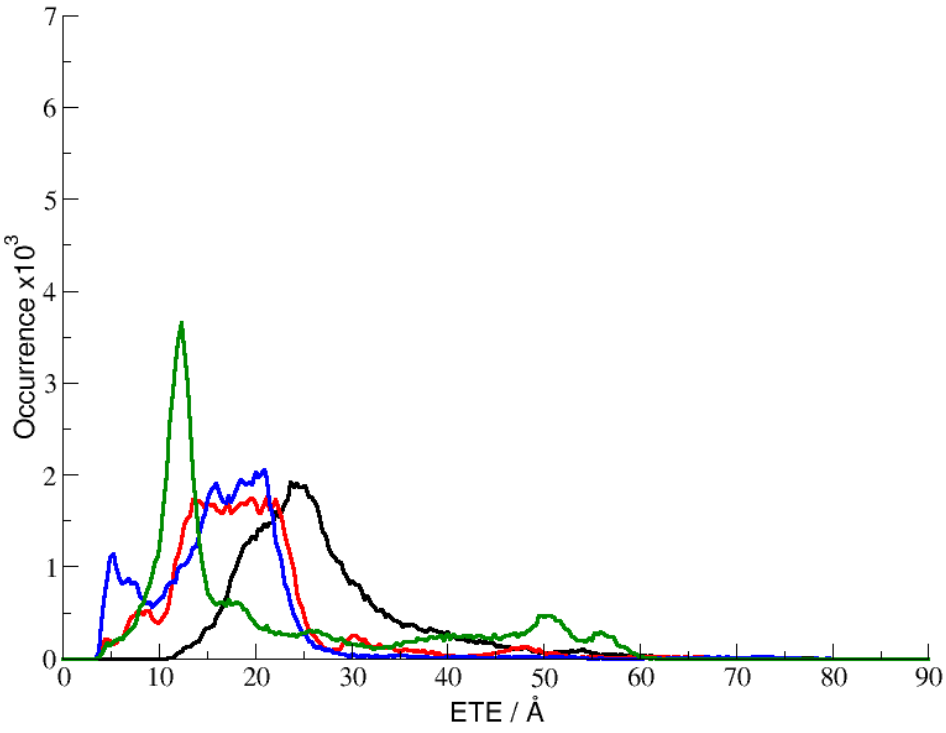


**(b)**

**Figure 3.7**: **(a)** Time series and **(b)** distributions relative to the end to end distance of the PCE-(23-7-1), computed along the simulations, for MD1 (black line), MD2 (red line), MD3 (blue line) and MD4 (green line).

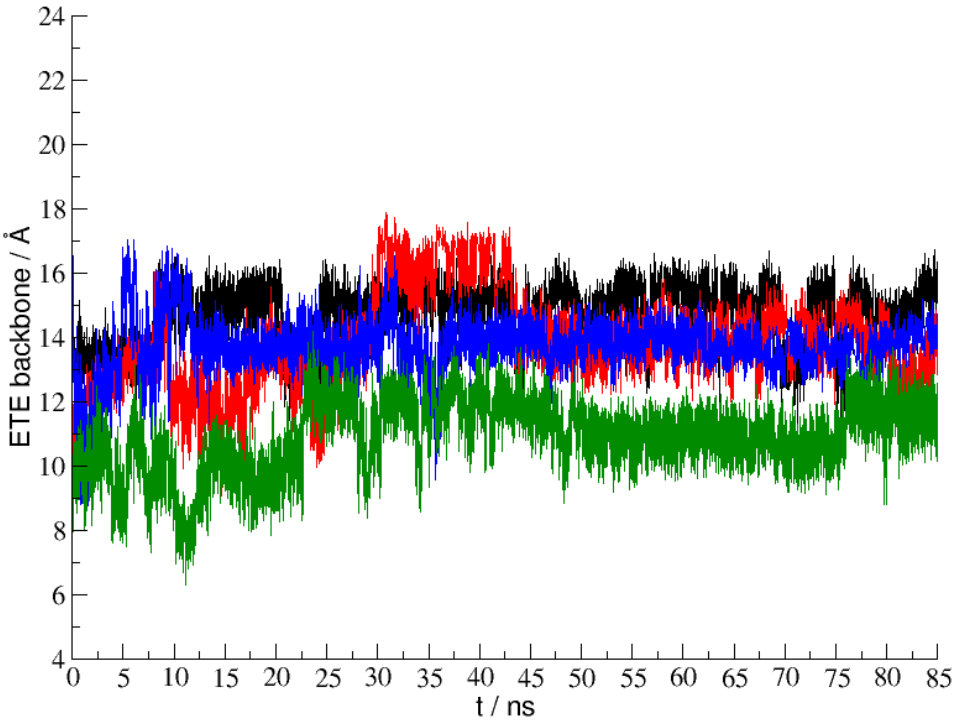


**(a)**

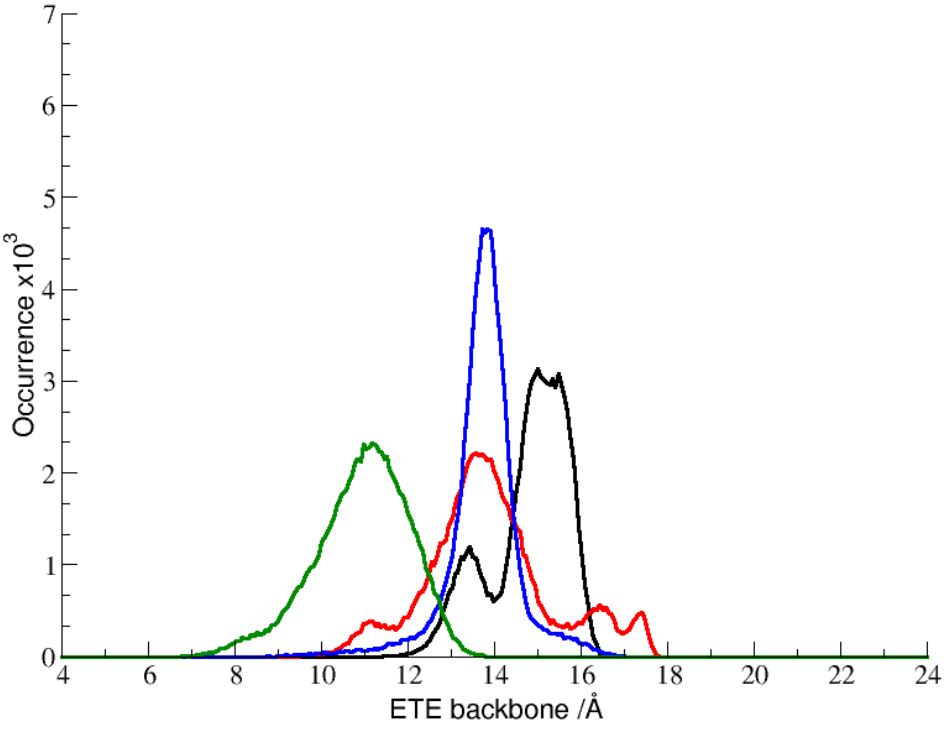


**(b)**

**Figure 3.8**: **(a)** Time series and **(b)** distributions relative to the end to end distance of the backbone, computed along the simulations, for MD1 (black line), MD2 (red line), MD3 (blue line) and MD4 (green line).

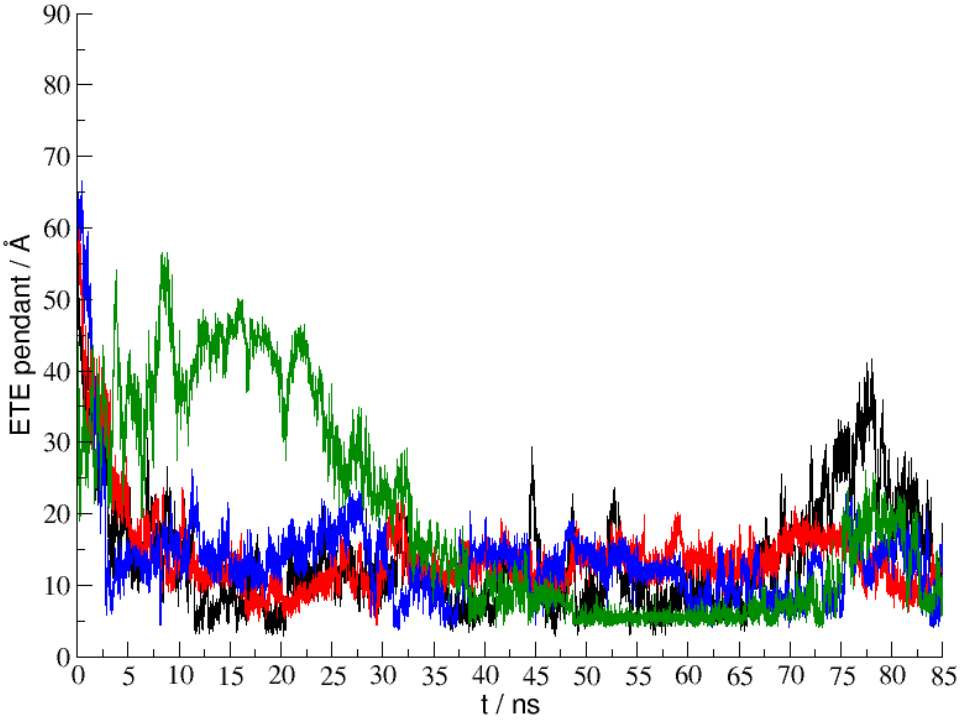


**(a)**

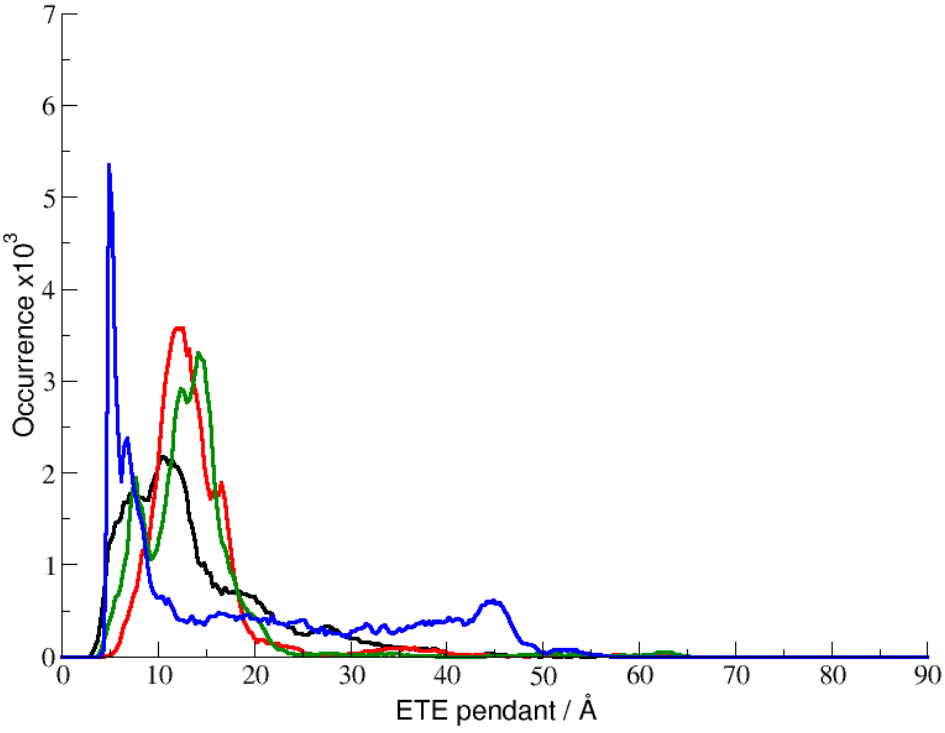


**(b)**

**Figure 3.9**: **(a)** Time series and **(b)** distributions relative to the end to end distance of the pendant, computed along the simulations, for MD1 (black line), MD2 (red line), MD3 (blue line) and MD4 (green line).

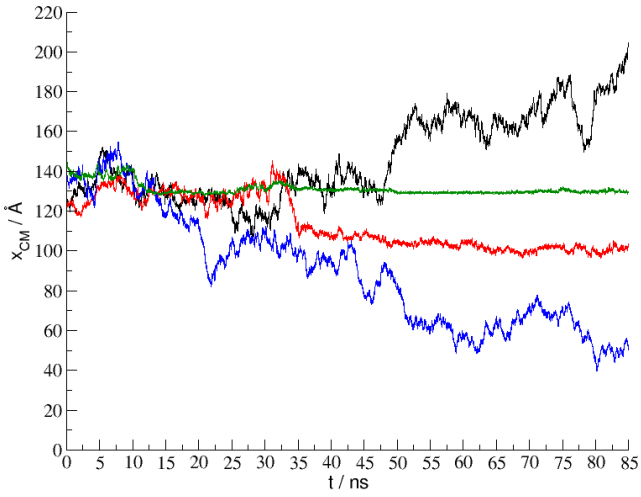


**(a)**

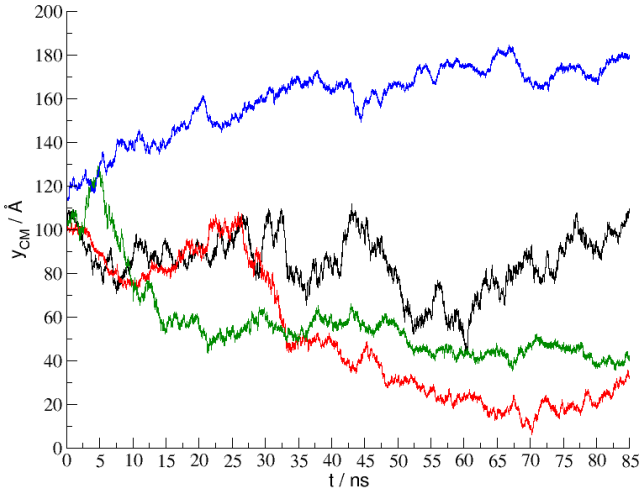


**(b)**

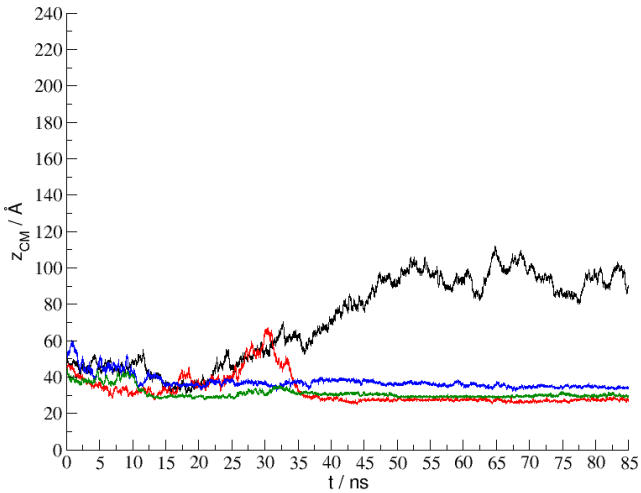


**(c)**

**Figure 3.10**: Time series relative of **(a)** *x*-component, **(b)** *y*-component, **(c)** *z*-component of dynamic of center of mass of the polymer, computed along the simulations, for MD1 (black line), MD2 (red line), MD3 (blue line) and MD4 (green line).

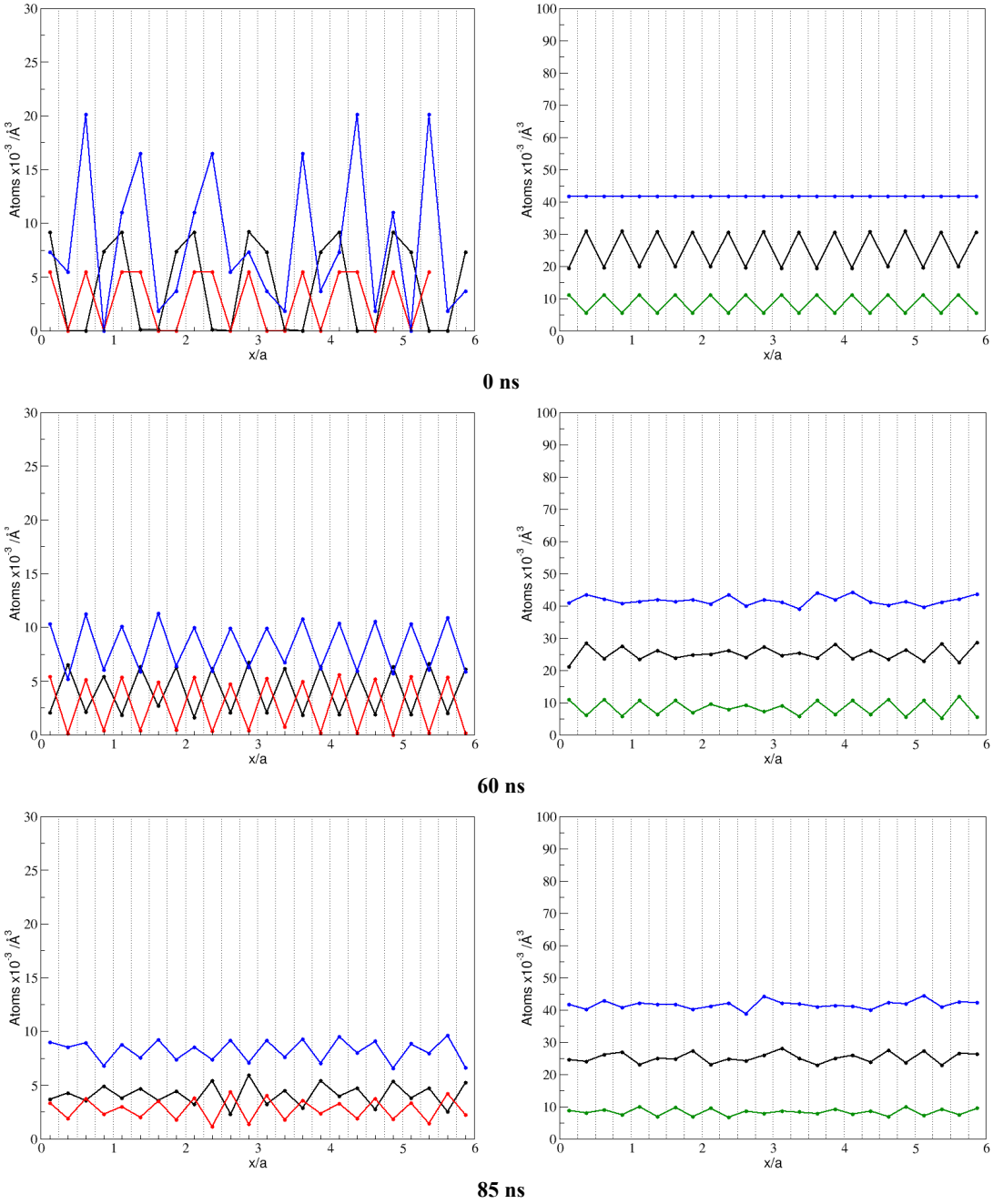


**Figure 3.13**: 1D-DP *x*-axis, for $C_3A$ (left) and $C_3S$ (right). Squares are referred to the number of atoms, per unit volume, in a given layer of calcium (black), aluminum (red), silicon (green) and oxygen (blue) atoms. ***a***=7.624 Å is the length of the unit cell of $C_3A$, ***a***=12.235 Å for $C_3S$.

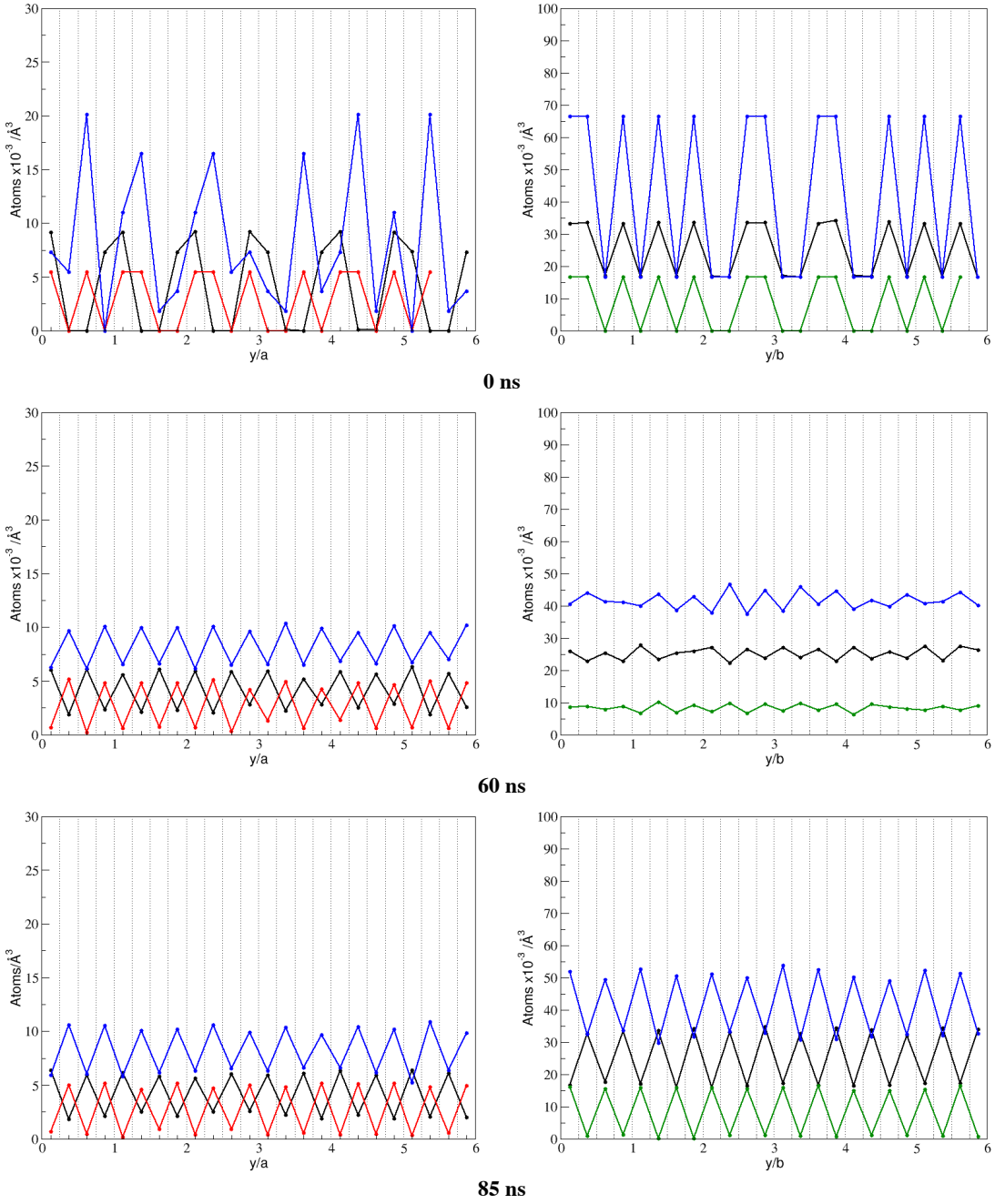


**Figure 3.14**: 1D-DP *y*-axis, for $C_3A$ (left) and $C_3S$ (right). Squares are referred to the number of atoms, per unit volume, in a given layer of calcium (black), aluminum (red), silicon (green) and oxygen (blue) atoms. ***a***=7.624 Å is the length of the unit cell of $C_3A$, ***b***=12.235 Å for $C_3S$.

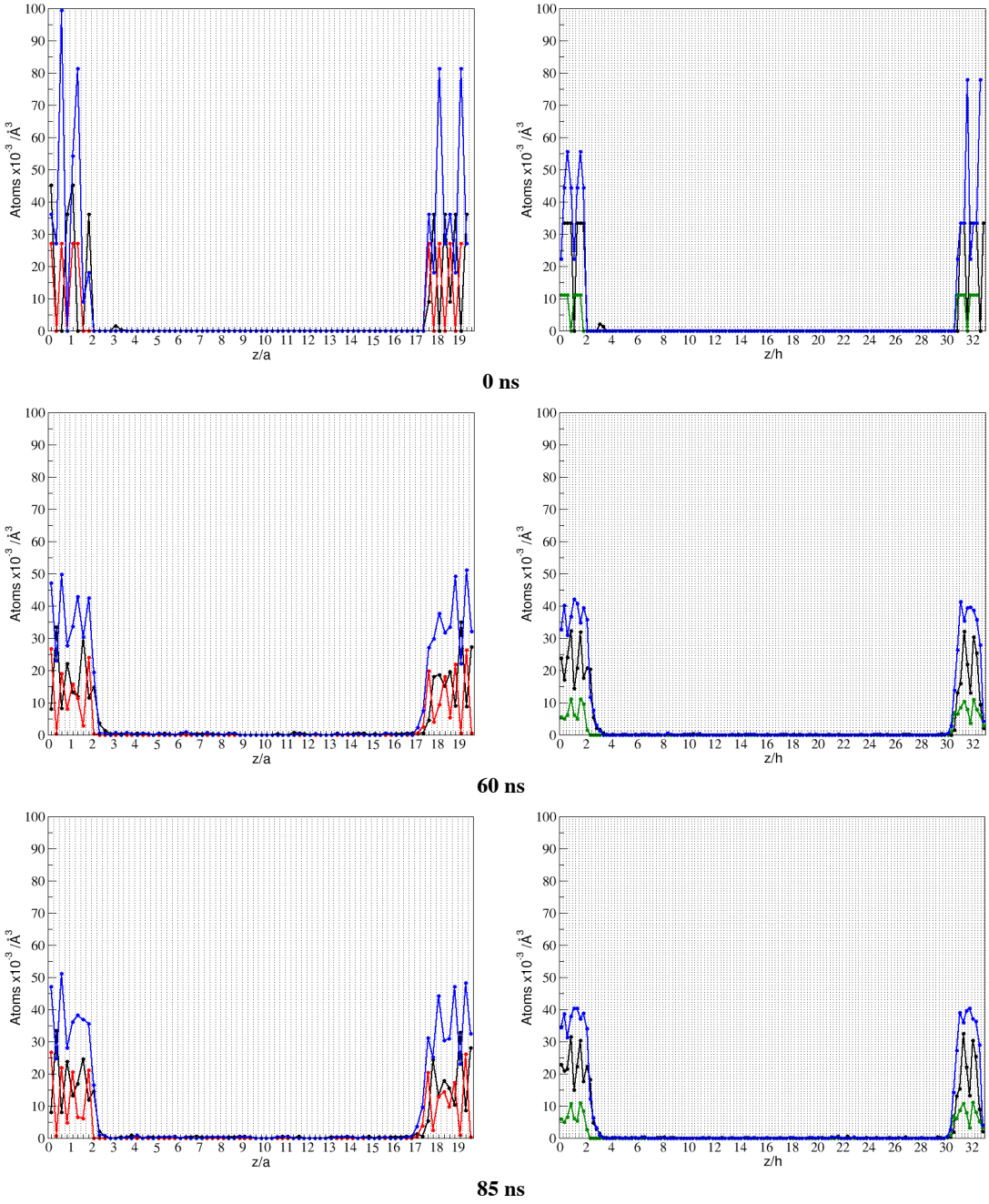


**Figure 3.15**: 1D-DP *z*-axis, for $C_3A$ (left) and $C_3S$ (right). Squares are referred to the number of atoms, per unit volume, in a given layer of calcium (black), aluminum (red), silicon (green) and oxygen (blue). ***a***=7.624 Å is the length of the unit cell of $C_3A$, ***h***=8.335 Å for $C_3S$.

# MOLECULAR MODELLING of Cx26

**Introduction**

Gap junction channels mediate communication between adjacent cells by allowing the passage of a variety of cytoplasmatic molecules: they are formed by the head-to-head docking of two connexins (Cx), tetraspan transmembrane proteins, that form examers in the plasma membrane, known as hemichannels or connexons, located in two adiacent cells [Maeda2009].

The four transmembrane (TM) helices are connected by two extracellular (EC) loops and a cytoplasmatic loop (CL).

The wide aqueous pores of connexons are permeable to a variety of cytoplasmic molecules, including amino acids, nucleotides, calcium ions, glucose and its metabolites, and this property underlies the widespread interest in the biological functions of connexin channels [Zonta2012].

Gap junctions play important roles in auditory function and skin biology; mutations in the Connexin 26 (Cx26, 26 KDa protomer) gene are the predominant cause of inherited non-syndromic deafness and cause disfiguring skin disorders.

These mutations are found in all topological domains of Cx26: they disrupt the intercellular molecular/ionic signalling pathway by affecting Cx channel function, assembly and/or trafficking.

These processes could be modulated or controlled by post-translational modifications (PTMs); the potential role of PTMs in Cx26 pathologies is unexplore, but many sites of this protein subject to PTMs have been identified and analyzed with mass spectrometry techniques [Locke2009].

The found PTMs include hydroxylation, methylation, phosphorylation, acetylation and γ-carboxyglutamation.

The publication of the 3.5 Å human Cx26 crystal data [Maeda2009] has been a long awaited result that shed light, elucidating the previous lower resolution structures [Unger1999; Fleishman2004; Oshima2007] and provided an essential starting point for deepened future investigations.

Each of the six connexins composing the hemichannel, has a particular tertiary structure that crosses the membrane four times. The main topology of a single connexin may be grouped in the transmembrane helices (TM1-4), the cytoplasmic

N/C-terminal (NT, CT) domains, the cytoplasmic loop (CL) that links TM2-TM3, an extracellular loop (E1) between TM1-TM2 and a second extracellular loop (E2) between TM3-TM4 (**Figure 4.1**). The TM1-4 helices span the following residue range: 21-40, 76-98, 132-154 and 193-215; the cytoplasmic NT domains, composed by residues 1-20, are located in the pore channel, while the cytosolic CT domain, going from residue 216 to 226, is located at the external portion of the connexon.

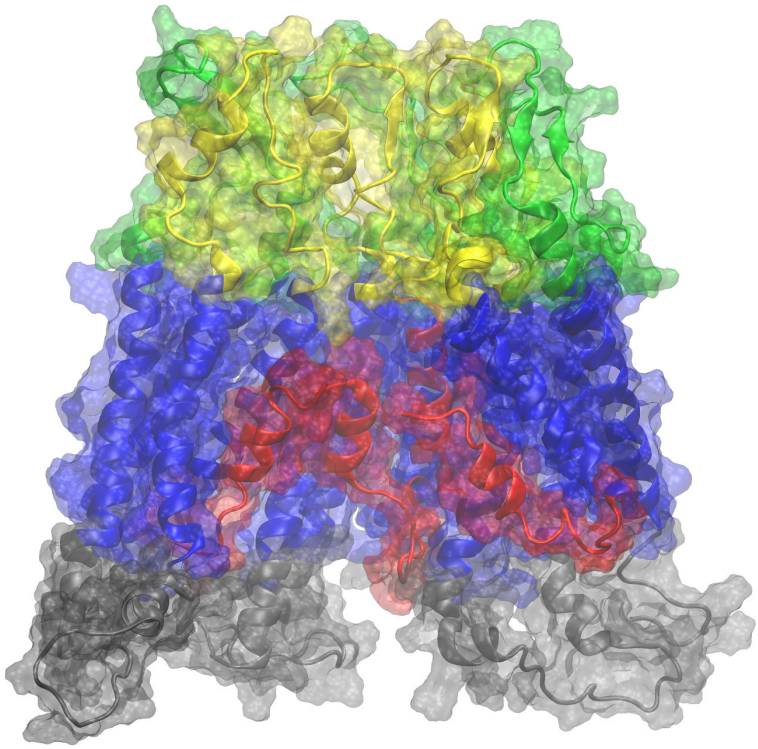

**Figure 4.1**: Cross-section of the protein. Colour code in the right panel according to [Maeda2009]: red, NT; blue, TM1-TM4; green, E1; yellow, E2; black, CL and CT.

The CL domain, which goes from residue 99 to 131, links TM2 and TM3 helices and, how we will see, is the most mobile portion of the whole system. The extracellular loop E1, goes from residue 41 to 75, while E2 has the following residue range 155-192 (Figure [Prot_view]). In the primary sequence there are 226 total amino acids, from which a portion of NT, CL and CT, i.e. residues 1, 110-124 and 216-226, were not located in the crystal data together with a some atoms of the side chain of residues 15, 17 and 19 [Maeda2009]. Although the absence of these amino acids may not influence the pore size directly (except for Met1 which falls at the center of the channel), they may assume an important structural role with consequences on the overall quaternary structure, thus they were included in all the simulations performed in this work.

A first attempt to describe structure-functions relation after PTMs was done (without explicitly including the charges of the modified residues) where after relaxing the protein structure with MD simulations, the pore diameter was larger with respect to the cryistallographic data, expecially near the N-terminal residues (i.e. Met1). Moreover acetylation of the Met1 residue did not show significant changes to the pore size and together with γ-carboxyglutamation switched the channel selectivity to cations [Maeda2009]. Other MD simulations highlighted that the open channel had a barrier due to the presence of Lys41 residue, that, in absence of an electrochemical gradient, obstructed ion diffusion through the pore [Zonta2012]; another work, instead, focused on permeation of calcein molecule through the channel, observing that electrostatic properties of the pore did not allow the penetration of the molecule corroborating two hypothesis: the 3.5 Å structure of the protein is not related to an open channel, because of the crystallization and dehydratation procedures; the PMTs in living cells transform profoundly the permeation properties thanks to the modification of the charge in the side chain of many residues [Zonta2013]. In addition two mutants of the Cx26 were studied by the same authors [Zonta2014*; Zonta2015] and, in particular, in case of M34T mutation, the subtitution of an apolar amino acid with a polar, did change the pore bottleneck and the NT domain was separated more easily from the inner wall of the channel, increasing the ions permeation barrier; instead the C169Y mutation located spatially near the extracellular portion, disrupted the disulfide bond with Cys64, compromising the protein structure. So the Cx26C169Y instead of being a polymorphism as previously identified, it was found both experimentally and computationally to be a dysfunctional channel with conseguent hearing loss due to problems in the intercellular head-to-head docking of two connexons. Dr. Mauro Torsello also characterized a simplified model of this system, using QM/QM calculations on a specific portion of the Cx26 to depict the $Ca^{2+}$ binding process to the Glu42 and Glu47 residues. We observed that calcium binding, after modification of the salt bridges with Arg75 and Arg184, may be responsible for the rearrangement of the quaternary structure of the system, with a possible following closure of the channel [Zonta2014].

In this work we tried to simulate the hemichannel behaviour in the presence of PTMs and $Ca^{2+}$. In particular we focused only on the γ-carboxylation of Glu42 and Glu47, which we believed to be responsible for the modification of the hemichannel

structure. To do so we derived new partial charges and missing FF parameters of the γ-carboxylated glutamate residue which we substituted in the protein sequence. Finally the system was analyzed from many different point of view, highlighting rigidity/flexibility, structure and energetics; my contribution essentially was aimed initially to the i) partial charges parametrization of Non-AA, secondly ii) the analysis of the structure of the channel and the analysis of iii) the preservation of salt bridges between Glu47, Arg75 and γ-Glu47, Arg75 in the presence and asbsence of $Ca^{2+}$.

**Partial charges parametrization of Non-AA**

As part of an on-going collaboration with prof. F. Mammano and Dr. Francesco Zonta of the Department of Physics and Astronomy of Padova, we calculated the partial charges of some Non-AA, present in the human Cx26 (Cx26_WT), using RESP method [Bayly1993].

Several charged residues of Cx26_WT can be modified by post translational modifications, which may also depend on cell condition such metabolic stress. In particular it was shown that Met1 and seven lysines are acetylated, whereas three glutamic acids are γ-carboxilated [Zonta2013].

Due to the difficulties of testing these very important sites, it was necessary to obtain accurate partial charges to describe, in the best way, the interaction of ions with these Non-AA: for this reason we employed the RESP methodology.

The RESP charge fit consisted of three stages. First, the geometry was fully optimized. Then, an electrostatic potential wass generated; and finally the RESP procedure was carried out.

The AA needed to be end-capped before the geometry optimization. In theory one could use any form of cap: the important thing was that the charges on the non-cap atoms had to sum to the correct integer charge. The cap procedure developed as part of the FF design for protein consisted in using ACE or NME residues, given in **Figure 4.2**.

We calculated the RESP charges of three Non-AA, Acetyl-Methionine (Acetyl-Met), Acetyl-Lysine (Acetyl-Lys) and γ-Glutamate-Carboxylate (γ-Glu) in mono anion form as well as dianion form.

In **Figure 4.3** the optimized geometry of Non-AA.

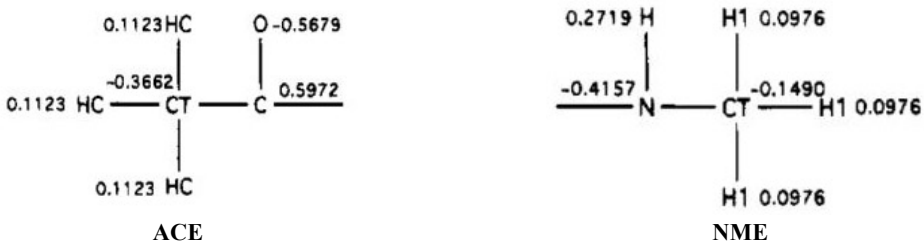


**Figure 4.2**: two capping groups with the charges that they are assigned in the AMBER FF9X force fields. These charges sum to zero in each case. We cap the broken covalent bond of the Non-AA with NME (CO side) and ACE (NH side). When we later carry out the RESP procedure, we constrain the NME and ACE atoms to have the same charges as they would in the FF9X force field [Cornell1995].

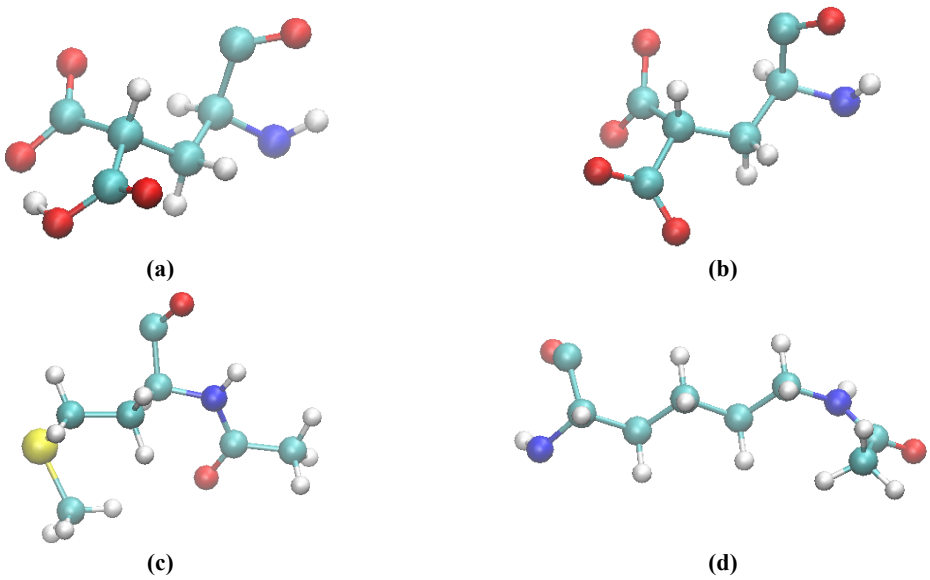

**(a)** **(b)**

**(c)** **(d)**

**Figure 4.3**: Ball & Stick representation of Non-AA structures optimized at level B3LYP/6-311G(D,P). **(a)** γ-Glu mono anion, **(b)** γ-Glu mono dianion, **(c)** Acetyl-Met, **(d)** Acetyl-Lys. The different colors correspond to different atom types: H atoms are white, O atoms are red, C atoms are cyan, S atom is yellow, N atoms are blue.

The results are summarized in the **Table 4.1**.

| Non-AA | $q_{tot}$ (C) | QM Method | Basis Set |
|---|---|---|---|
| γ-Glu mono anion | -1 | B3LYP | 6-311G(D,P) |
| γ-Glu dianion | -2 | | |
| Acetyl-Met | 0 | | |
| Acetyl-Lys | 0 | | |

**Table 4.1**: partial charges parametrization data.

**Channel analysis**

We obtained three different simulations for both the wild type (Cx26_WT) and the PTM Connexin 26 (Cx26_GG), in the absence ($[Ca^{2+}]$ = 0 mM) and in the presence of 2 (fisiological condition, $[Ca^{2+}]$ = 2 mM) and 4 $Ca^{2+}$ ions (saturated condition, $[Ca^{2+}]$ = 4 mM).

The analysis of the simulations was carried on the 100 ns of production dynamics.

The tool used for analysis of Cx26 was HOLE: this method allows the analysis of the dimensions of the channel using the Metropolis Monte Carlo simulated annealing procedure.

The channel was sliced into parallel planes perpendicular to the user-defined vector (*z*-axis), which approximated the general direction of the channel. The search started on a plane, containing the initial point located inside the channel, which was selected by the user (the zero point of the inertial reference system, **Figure 4.4 (c)**). The position of the point was randomly adjusted by the Monte Carlo procedure to maximize the radius of the sphere centered at this point which did not intersect the vdW surface of surrounding atoms [Weiner1984]. When the maximal sphere was found, its center was transferred along the channel vector into the next plane, and the whole process was repeated. The algorithm could be viewed as a process of squeezing a flexible sphere through the center of the channel [Smart1996; Brezovsky2013].

We analyzed the channel by sampling the structure every four ns, and by doing the calculations using HOLE; then, we averaged along the whole simulation. The results are given in **Figure 4.5**. The γ-carboxylation tended to further open the channel and made it insensitive to changes due to the presence of $Ca^{2+}$ ions: Cx26_GG was wider and did not seem sensible to $Ca^{2+}$ ions while Cx26_WT was narrower and calcium-sensing.

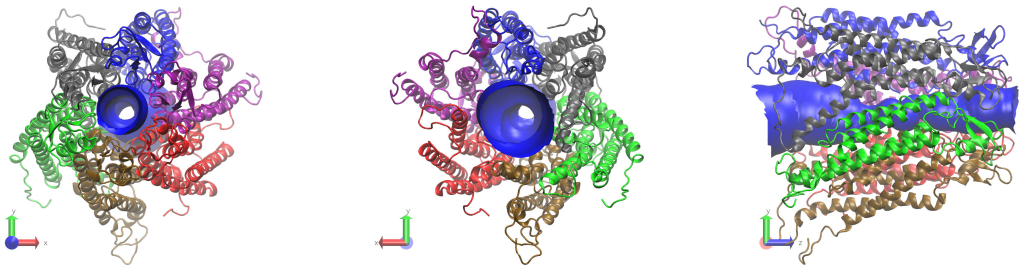

**(a)** **(b)** **(c)**

**Figure 4.4**: **(a)** Cx26 Top view. **(b)** Cx26 Down view. **(c)** Cx26 Side view. In all pictures, the blue solid surface computed by HOLE wich represents the channel simulated by the Metropolis Monte Carlo annealing procedure.

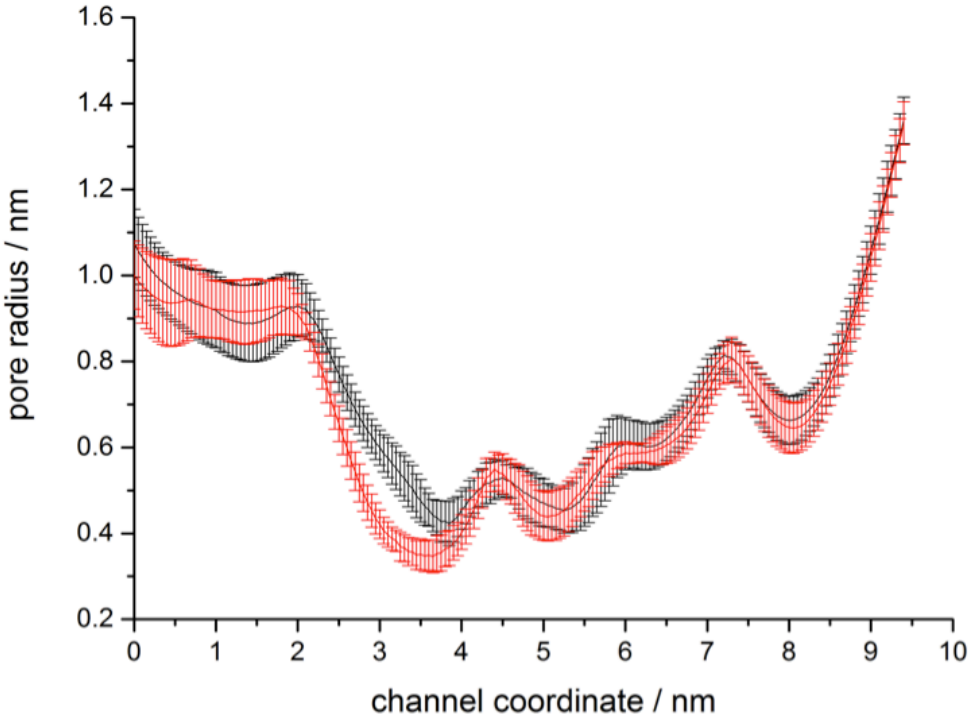


**(a)**

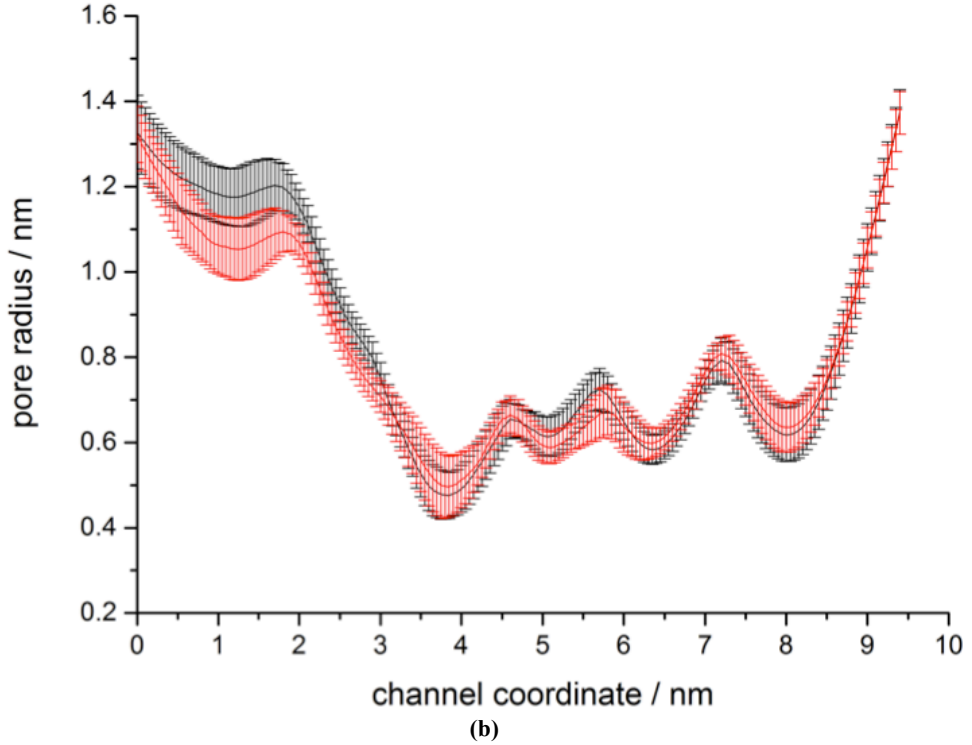


**(b)**

**Figure 4.5**: 2D graph of pore radius vs channel coordinate of **(a)** Cx26_WT and **(b)** Cx26_GG, at different concentrations of $Ca^{2+}$, 0 mM (black line) and 2 mM (red line). The values where averaged along the whole simulation.

**Salt bridges analysis**

The salt bridge arises from the anionic carboxylate (RCOO−) of Glu and the cationic guanidinium (RNHC(NH2)2+) of Arg.

The requirements to obtain a salt bridge are the same as defined by Kumar and collaborators [Kumar2002]: i) the side-chain charged group centroids are within a 4.0 Å, ii) at least one pair of side-chain carbonyl oxygen and side-chain nitrogen atoms is within a 4.0 Å distance.

Our order parameter was the ratio of N-O distance and centroid distance.

The centroids were defined considering the atoms of carboxyl groups of Glu47 and γ-Glu47 and the atoms of guanidinium group of Arg75.

On **Figure 4.6**, all possible pairs H-O considered.

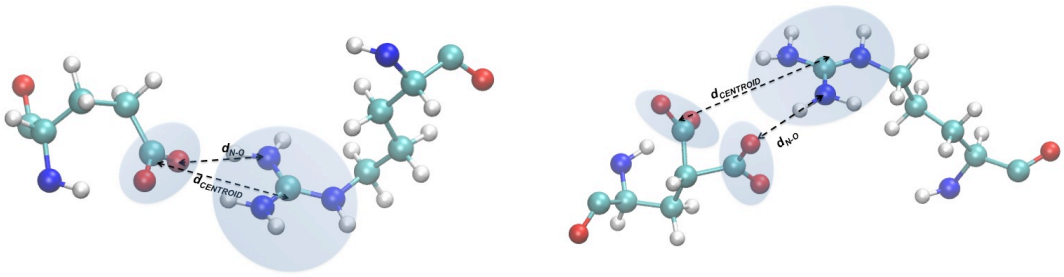


**(a)** **(b)**

**Figure 4.6**: Salt bridge between Glu47-Arg75 **(a)** and for **(b)** γ-Glu47-Arg75.

In Cx26 the AA residues were 1355: for simplicity, we defined in the all six connexin the pair Glu47-Arg75 as: Glu47-Arg75, Glu273-Arg301, Glu499-Arg527, Glu725-Arg753, Glu951-Arg979, Glu1177-Arg1205.

On the basis of calculations carried out, in general the presence of $Ca^{2+}$ did not interfere with salt bridges; in both case, Cx26_WT and Cx26_GG, the salt bridges were maintained. We are doing further investigations to verify this phenomenon.

The results in **Figure 4.7-4.8**.

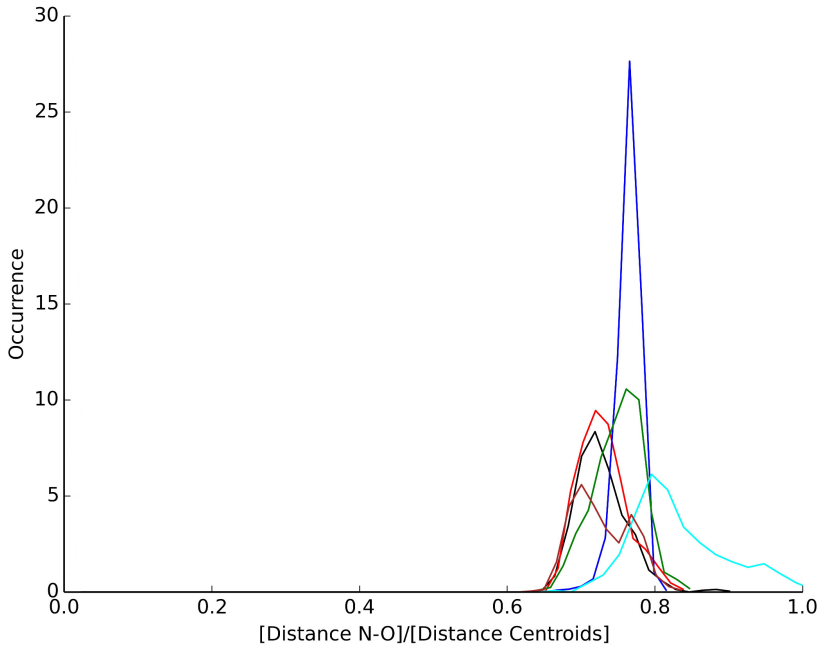


**(a)**

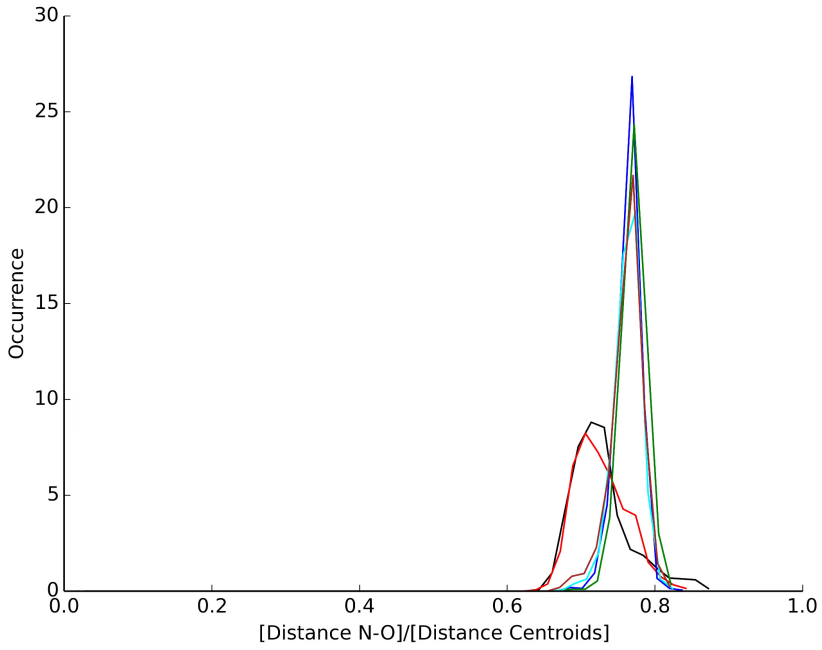


**(b)**

**Figure 4.7**: **(a)** Cx26_WT at [$Ca^{2+}$] = 0 mM. **(b)** Cx26_WT at [$Ca^{2+}$] = 2 mM. Colour code corresponds to different connexin units.

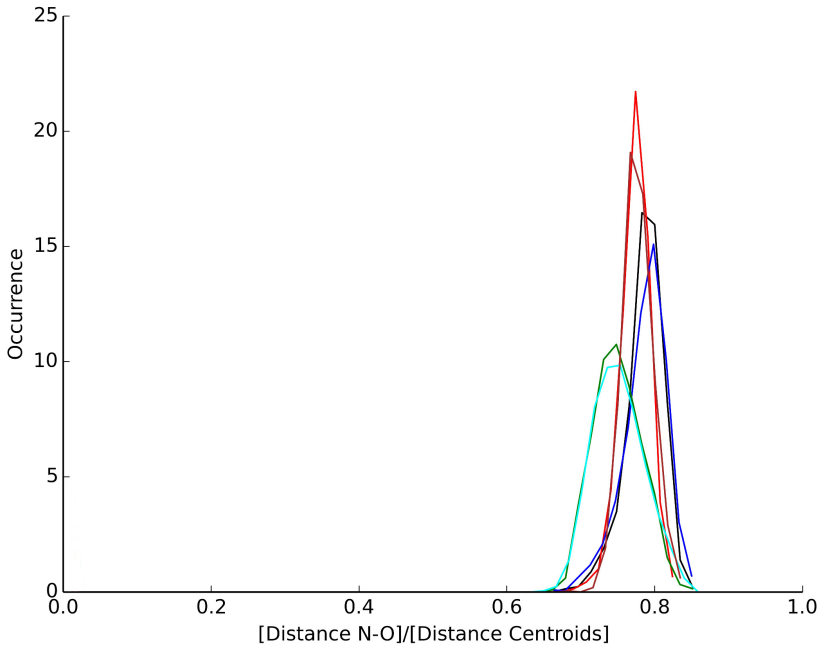


**(a)**

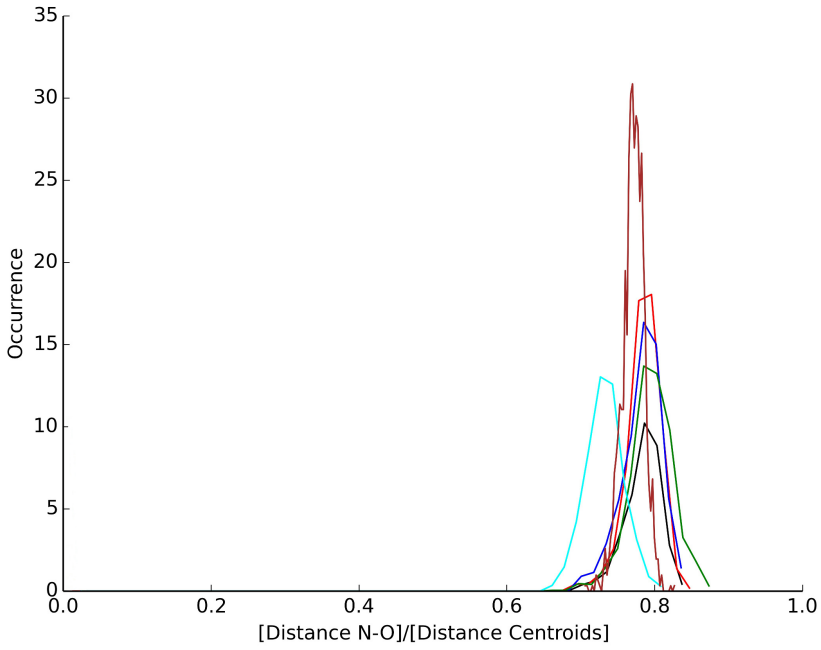


**(b)**

**Figure 4.8**: **(a)** Cx26_GG at [$Ca^{2+}$] = 0 mM. **(b)** Cx26_GG at [$Ca^{2+}$] = 2 mM. Colour code corresponds to different connexin units.

# THERMODYNAMIC MODEL OF EQUILIBRIUM PROPERTIES OF GLASSY MATERIALS

**Introduction**

In glass research and technology, it is often necessary to reduce the costs of raw materials, to improve specific properties, or to design a glass composition for new applications.

In recent years, the creation of large glass property databases has facilitated systematic glass property modelling and property measurement evaluation.

Commercially available systems (e.g. SciGlass and Interglad) combine hundreds of thousands of experimental findings from the majority of glass research papers from over a century, including the associated references.

Despite the recent progress, there are several shortcomings in these commercial tools: 1) Numerous experimental data from various investigators differ significantly, even within simple glass systems and for well investigated properties. 2) Many predictive glass property models exist in the literature, and it is sometimes difficult to decide which model is the most appropriate. 3) Industrial glasses have complex compositions, and it is not always possible to predict properties through commonly used linear property–composition relations. 4) Some of the published models are based on scientific principles or derived assumptions about the details of chemical bonding within a glass. Therefore, experiments need to be interpreted before some models can be established. This can be a source of error based on the accuracy of this interpretation. 5) Some models consider the experimental findings of a few or only one single investigator, i.e. systematic errors of a few investigators easily can lead to incorrect conclusions. The prediction errors for models based on one investigator reflect the measurement precision in her/his laboratory, but it is not possible to conclude how such prediction errors will relate to those based on data from other laboratories [Fluegel2009].

In this work, the goal was the elaboration, optimization and validation of a simple model of the type of ideal solutions for the thermodynamic properties of glass.

The achievements of this first part were i) the application of the model of ideal solutions for the calculation of the composition of silicate glasses at different temperatures; ii) the cubic interpolation, for the temperature dependence, of these thermodynamic data $\Delta_f^{\circ} G(T)$ (thermodynamically consistent) of elementary oxides and mixed oxides inside the glass.

**Thermodynamic model**

Since we wanted to evaluate the thermodynamic properties of the glass in the liquid phase, for simplicity we described it as an *ideal solution*.

We defined

$$OE:=\{A,B,\ldots\} \tag{5.1}$$

the set of elementary oxides inside the glassy material.

We defined

$$OM:=\{A_{\nu_A}B_{\nu_B},\ldots\} \tag{5.2}$$

the set of mixed oxides inside the glassy material.

Both for *OE* that for *OM* we supposed to be known thermodynamic properties both in solid phase or liquid.

We defined

$$C:=OE\cup OM \tag{5.3}$$

the set of all the components present inside the liquid phase (glassy).

We defined $N_{OE}$ (number of elementary oxides)

$$i=1\div N_{OE} \tag{5.4}$$

where *i* was the index on the elementary oxides.

We defined $N_{OM}$ (number of mixed oxides) and

$$j=1\div N_{OM} \tag{5.5}$$

$$\nu_i(j) \tag{5.6}$$

where *j* was the index on the mixed oxides and (8) was the *i*-th stoichiometric coefficient of the *j*-th mixed oxide.

We defined

$$N_C:=N_{OE}+N_{OM} \tag{5.7}$$

About composition of the liquid phase equilibrium, we defined

$$i=1\div N_{OE},\quad n_i \tag{5.8}$$

$$j=1\div N_{OM},\quad m_i \tag{5.9}$$

$$n=\sum_{i=1}^{N_{OE}} n_i+\sum_{j=1}^{N_{OM}} m_j \tag{5.10}$$

$$x_i=n_i/n\quad ;\quad y_j=m_j/n \tag{5.11}$$

where $n_i$ was the number of moles of elementary oxide, $m_j$ was the number of moles of mixed oxide, $n$ was the total number of moles, $x_i$ was the molar fraction of elementary oxide, $y_j$ was the molar fraction of mixed oxide.

About chemical equilibria in the liquid phase at the temperature $T$: for every $j$-th mixed oxide, with composition $A_{\nu_A}B_{\nu_B}$, we defined

$$\nu_A A+\nu_B B=A_{\nu_A}B_{\nu_B} \tag{5.12}$$

$$K_j^{(l)}(T)=\frac{y_{A_{\nu_A}B_{\nu_B}}}{x_A^{\nu_A}x_B^{\nu_B}} \tag{5.13}$$

$$-RTlnK_j^{(l)}(T)=\Delta_r G^{\circ}_{A_{n_A}B_{n_B}(l)}(T)=\Delta_f G^{\circ}_{A_{n_A}B_{n_B}(l)}(T)-\nu_A\Delta_f G^{\circ}_{A(l)}(T)-\nu_B\Delta_f G^{\circ}_{B(l)}(T) \tag{5.14}$$

About the stoichiometric constraints we defined

$$i=1\div N_{OE},\ n_i^0=n_i+\sum_{j=1}^{N_{OM}}\nu_i(j)m_j \tag{5.15}$$

$$\sum_{i=1}^{N_{OE}} n_i^0=1 \tag{5.16}$$

and (5.16) was the normalization of stoichiometric constraints.

Therefore, if we fixed $n_i^0\ \left(i=1\div N_{OE}\right)$, $K_j^{(l)}\ \left(j=1\div N_{OM}\right)$, we could calculate the composition of species oxides, looking the zeros of the $N_C:=N_{OE}+N_{OM}$ equations

$$\begin{aligned} &i=1\div N_{OE}: f_i(z):=n_i+\sum_{j=1}^{N_{OM}}\nu_i(j)m_j-n_i^0=0\\ &j=1\div N_{OM}: g_i(z):=K_j^{(l)}\left[\prod_{i=1}^{N_{OE}} n_i^{\nu_i(j)}\right]-m_j\left[\sum_{j=1}^{N_{OE}} n_i+\sum_{j=1}^{N_{OM}} m_i\right]^{\sum_i \nu_i(j)-1}=0 \end{aligned} \tag{5.17}$$

in the $N_C$ unknown quantities $z:=(n_1,\ldots,n_{N_{OE}},m_1,\ldots,m_{N_{OM}})$.

**Interpolation for the temperature dependence of $\Delta_f G_X^\circ(T)$**

From NIST-JANAF data (http://kinetics.nist.gov/janaf/) of $\Delta_f G_X^\circ(T_p)$ and $\Delta_f H_X^\circ(T_p)$, with $T_p = p \times 100K$, $p=0,1,2\ldots$, where $X$ could be elementary or mixed oxides in solid or liquid phase, we made a cubic interpolation for the temperature dependence of $\Delta_f G_X^\circ(T)$ thermodynamically consistent, using Gibbs-Helmotz equation.

We proceeded in this way:

$$\frac{d\Delta_f G_X^\circ(T)/T}{d1/T} = \Delta_f H_X^\circ(T) \tag{5.18}$$

$$T_p \le T \le T_{p+1} \quad ; \quad x := \frac{1}{T} - \frac{1}{T_p} \quad ; \quad \Delta x := \frac{1}{T_{p+1}} - \frac{1}{T_p} \tag{5.19}$$

$$\frac{\Delta_f G_X^\circ(T)}{T} = \frac{\Delta_f G_X^\circ(T_p)}{T_p} + ax + bx^2 + cx^3 \tag{5.20}$$

$$\Delta_f H_X^\circ(T) = a + 2bx + 3cx^2 \quad ; \quad a = \Delta_f H_X^\circ(T_p) \tag{5.21}$$

$$\begin{cases} A := \dfrac{\Delta_f G_X^\circ(T_{p+1})}{T_{p+1}} - \dfrac{\Delta_f G_X^\circ(T_p)}{T_p} - \Delta x \Delta_f H_X^\circ(T_p) = b\Delta x^2 + c\Delta x^3 \\ B := \Delta_f H_X^\circ(T_{p+1}) - \Delta_f H_X^\circ(T_p) = 2b\Delta x + 3c\Delta x^2 \end{cases} \tag{5.22}$$

$$b = \frac{3A - B\Delta x}{\Delta x^2} \quad ; \quad c = \frac{B\Delta x - 2A}{\Delta x^3} \tag{5.23}$$

**Application: bynary system $Na_2O$-$SiO_2$**

We applied our model to a simple binary system $Na_2O$-$SiO_2$ because we could compare our results with those of the scientific literature [Conradt2004].

$$\begin{aligned} OE &= \{A, B\} \equiv \{Na_2O, SiO_2\} \\ OM &= \{AB, AB_2, A_2B\} \equiv \{Na_2OSiO_2, Na_2O(SiO_2)_2, (Na_2O)_2 SiO_2\} = \\ &= \{Na_2SiO_3, Na_2SiO_5, Na_4SiO_4\} \\ C &= \{A, B, AB, AB_2, A_2B\} \end{aligned} \tag{5.24}$$

Given the values of $n_A^0, n_B^0$ and $K_{AB}^{(l)}, K_{A_2B}^{(l)}, K_{AB_2}^{(l)}$, then the calculation of the equilibrium composition was done by searching for the zeros of these equations

$$\begin{cases} n_A^0 = n_A + m_{AB} + 2m_{A_2B} + m_{AB_2} \\ K_{AB}^{(l)}(T) = \left(n_A + n_B + m_{AB} + m_{A_2B} + m_{AB_2}\right) \cdot \dfrac{m_{AB}}{n_A n_B} \\ K_{A_2B}^{(l)}(T) = \left(n_A + n_B + m_{AB} + m_{A_2B} + m_{AB_2}\right)^2 \cdot \dfrac{m_{A_2B}}{n_A^2 n_B} \\ K_{AB_2}^{(l)}(T) = \left(n_A + n_B + m_{AB} + m_{A_2B} + m_{AB_2}\right)^2 \cdot \dfrac{m_{AB_2}}{n_A n_B^2} \\ n_B^0 = n_B + m_{AB} + m_{A_2B} + 2m_{AB_2} \end{cases} \tag{5.25}$$

in the five unknown quantities $n_A, n_B, m_{AB}, n_{A_2B}, m_{AB_2}$.

We computed the relative distribution of components in melts from the binary $Na_2O$–$SiO_2$ at 1400 °C as a function of composition: the graph that we obtained was virtually identical to that of the work of Conradt et al [Conradt2004]; the results in **Figure 5.1**.

Lastly we tested our model, for the same binary system $Na_2O$-$SiO_2$, changing the initial concentration of elementary oxides, to derive le composition of glass, whose species are at thermodynamic equilibrium each other.

In particular

- Test1: $x_0(Na_2O) = 0.5$; $x_0(SiO_2) = 0.5$.
- Test2: $x_0(Na_2O) = 0.2$; $x_0(SiO_2) = 0.8$.
- Test1: $x_0(Na_2O) = 0.8$; $x_0(SiO_2) = 0.2$.

where $x_0$ is the initial molar fraction of the elementary oxide.

We obtained temperature dependence of free energy of formation and temperature dependence of free energy of reaction for all mixed oxides inside the glassy material

and the temperature dependence of composition of glass expressed by molar fration. The results in **Figure 5.2-5.3**.

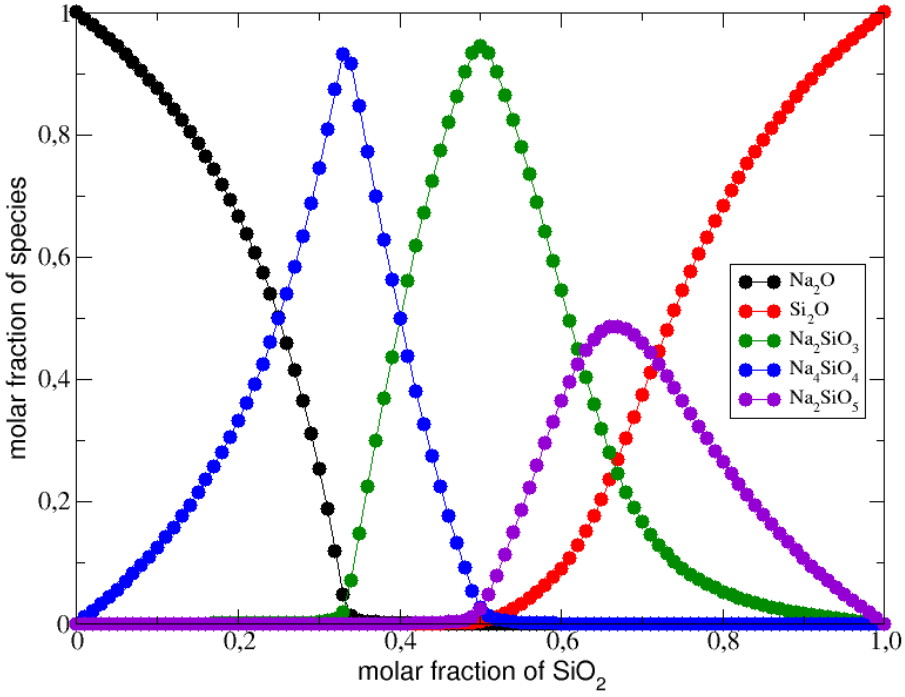


**(a)**

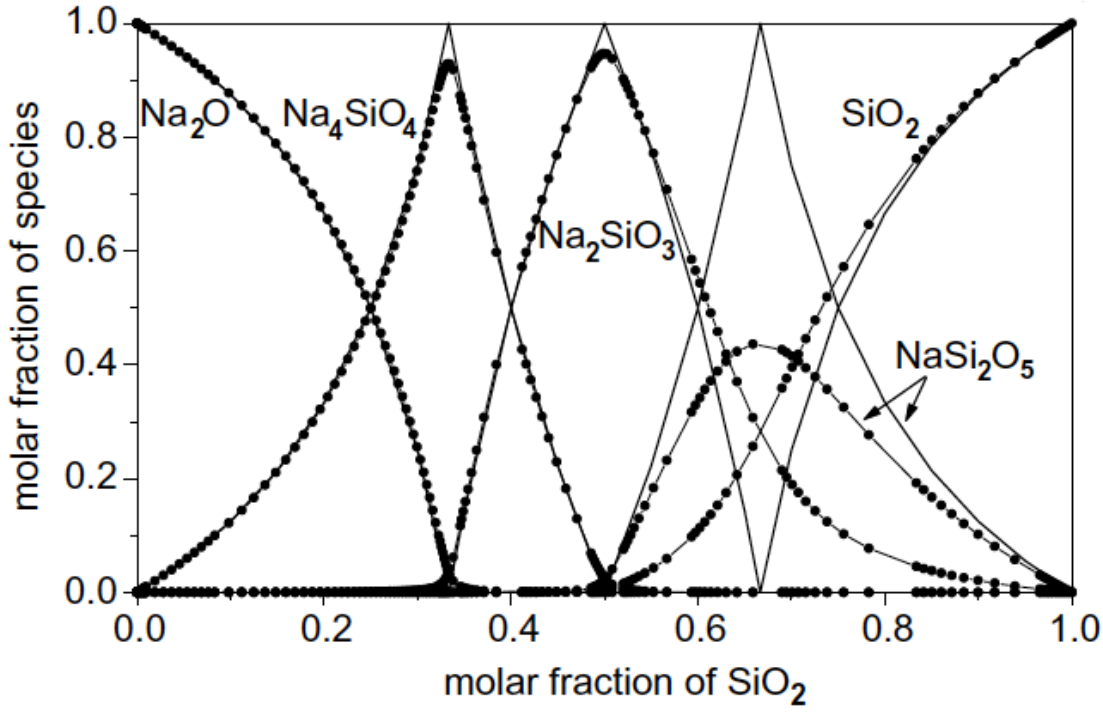


**(b)**

**Figure 5.1**: Relative distribution of components in melts from the binary $Na_2O$–$SiO_2$ at 1400 °C as a function of composition computed **(a)** with our Themordynamic Model and in the work of **(b)** Conradt [Conradt2001].

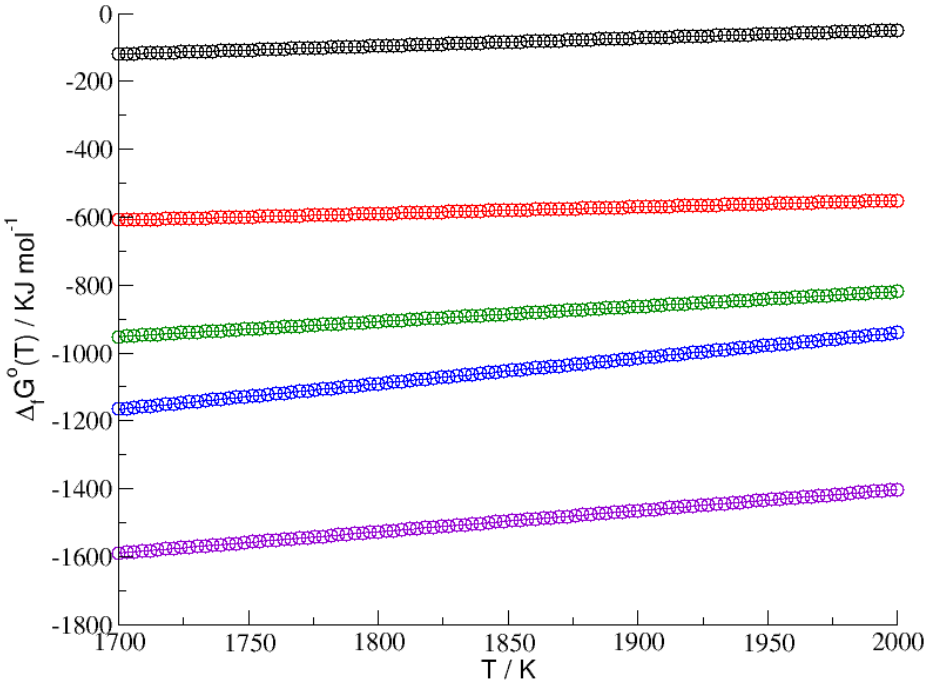


**(a)**

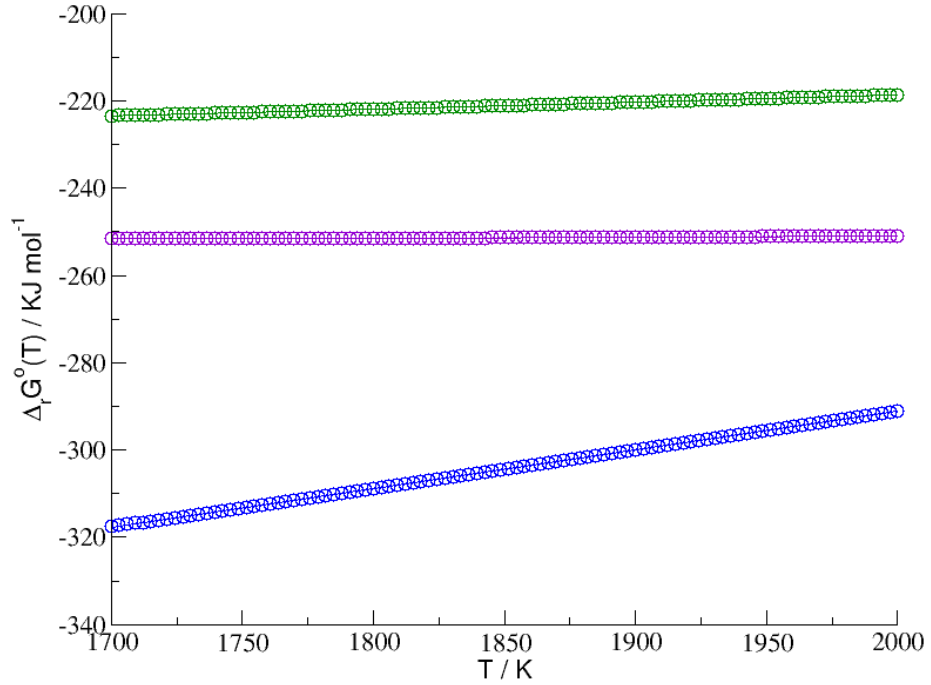


**(b)**

**Figure 5.2**: Temperature dependence of **(a)** free energy of formation and of **(b)** free enthalpy of formation of all oxides present inside the glassy material. The color lines represent the different oxides in the glassy material: black is $Na_2O$, red is $SiO_2$, green is $Na_2SiO_3$, blue is $Na_4SiO_4$, violet is $Na_2SiO_5$.

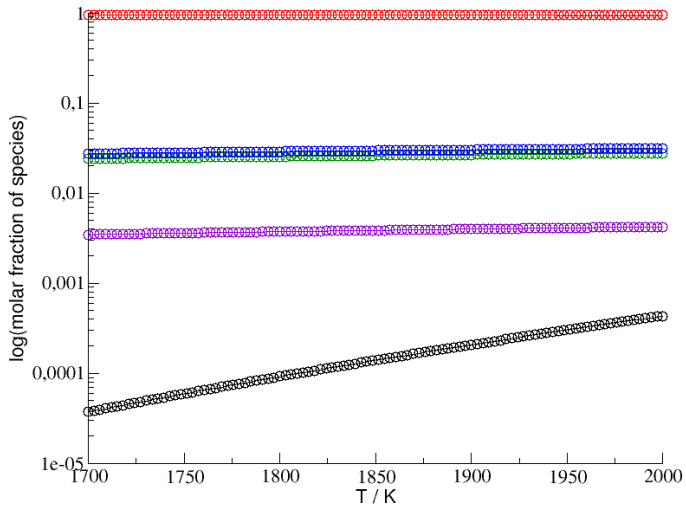


**(a)**

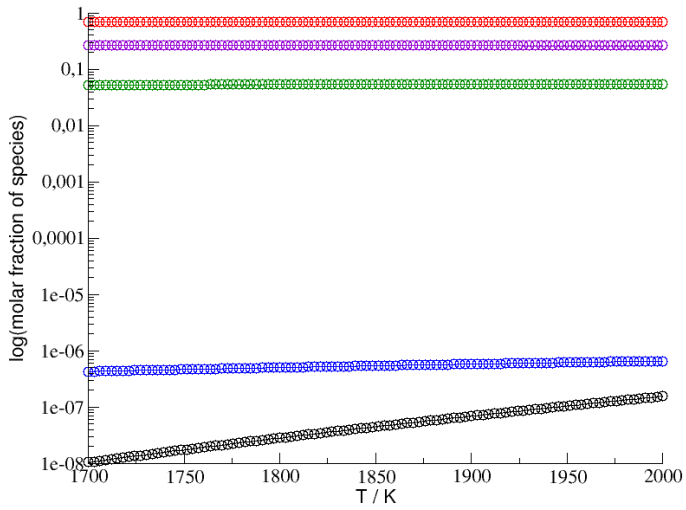


**(b)**

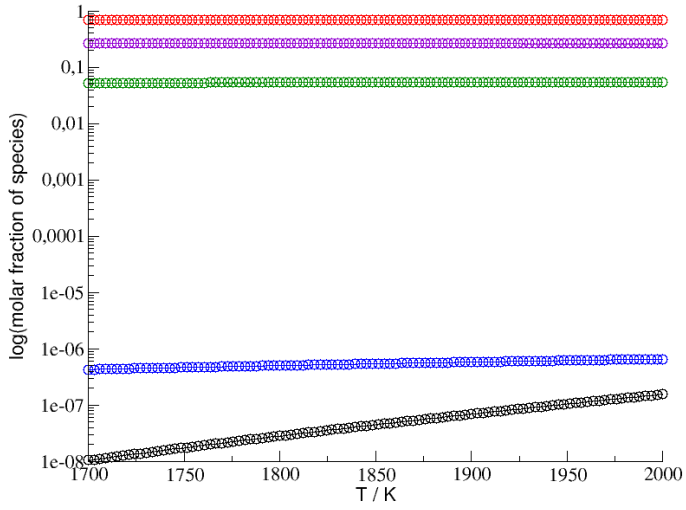


**(e)**

**Figure 5.3**: Temperature dependence of composition of glass expressed by molar fration for **(a)** Test1, for **(b)** Test2 and for (c) Test3. The color lines represent the different oxide species in the glassy material: black is $Na_2O$, red is $SiO_2$, green is $Na_2SiO_3$, blue is $Na_4SiO_4$, violet is $Na_2SiO_5$.

# CONCLUSIONS

In this PhD we presented a new MD protocol to study the influence of PCE superplasticizers on the evolution of cement during early hydration. The study was focused on the simulation of the interaction of a comb-shaped polymer unit model, PCE-(23-7-1), on a $C_3A$ and $C_3S$ surface.

The MD protocol described well the behaviour of the systems and the results of the simulations showed that the mobility of the polymer was due primarily to the dynamics of the side-chain. In particular, the polymer with the largest number of methacrylic units near the surface of $C_3A$ and $C_3S$ displayed a limited degree of mobility: it remained attached to the surface and it was less flexible than the free one.

This is, to our knowledge, the first example of accurate MD atomistic simulations of the interaction of PCE superplasticizers with cement surfaces. Previous MD studies were primarily focused on the structural properties of the cementitious phases, rather than on the intrinsic kinetic aspects of cement hydration: structural and molecular interaction informations generated with these studies could be a valuable input for mesoscopic and macroscopic models.

Although the dimensionality of the system studied here was relatively large (approximately $10^4$ atoms), a standard MD approach is still feasible and remains a valid basis for addressing larger and more realistic systems involved in the hydration process, which may be addressed, for instance, based on coarse-grained methods.

About the work on modelling of Cx26, the results showed that Cx26 (without PTM) was sensitive the presence of $Ca^{2+}$: the channel in physiological conditions was larger. It needs further work to understand the effect of γ-carboxylation on the type mechanism of channel opening-closing.

About the work on modelling of glassy materials, the model interpolated very well thermodynamic NIST-JANAF data and the composition of a glass at different temperatures.

The limitation of the model is given by the presence/absence of thermodynamic data; next step will be the implementation of calculation of transport properties (e.g. viscosity,…), the inclusion of $O_2$ equilibrium inside the molten glass, etc.

# LIST OF PUBLICATIONS

Nicola Fortunati, Vincenzo Russo. In *Molecular Dynamics protocol validation applied to the system PCE/$C_3A$*, Abstract Book, Vol. I, Proceedings of the 14th International Congress on the Chemistry of Cement, Beijing, 13-16 October 2015.

Nicola Fortunati, Gilberto Artioli, Antonino Polimeno, et al *Molecular Dynamics protocol validation applied to the system PCE-$C_3A$/ PCE-$C_3S$*, (In preparation, Part1 & Part 2)

Zonta, F.; Mammano, F.; Torsello, M.; Fortunati, N.; Orian, L.; Polimeno, A. Role of gamma carboxylated Glu47 in connexin 26 hemichannel regulation by extracellular $Ca^{2+}$: Insight from local quantum chemistry study *Biochem. Biophys. Res. Commun.*, **2014**, 445, 10-15.

Mauro Torsello, Nicola Fortunati, Laura Orian, Paolo Calligari, Antonino Polimeno *The $Ca^{2+}$ - promoted gating mechanism in the wild type and the γ-carboxylated connexin 26: a molecular simulation study*, (In preparation).

# REFERENCES


[Aggarwal1972] Aggarwal, S.; Gard, G. A.; Glasser, F. P. Synthesis and properties of dicalcium aluminate *Cem. Concr. Res.*, **1972**, 2, 291-297.

[Anderson2005] Anderson, K. L.; Sinsawat, A.; Vaia, R. A.; Farmer, B. L. Control of Silicate Nanocomposite Morphology in Binary Fluids: Coarse-Grained Molecular Dynamics Simulations *J. Polym. Sci. Part B Polym. Phys.*, **2005**, 43, 1014-1024.

[Barbier1985] Barbier, J.; Hyde, B. G. The structure of the polymorphs of dicalcium silicate, $Ca_2SiO_4$ *Acta Crystallogr., Sect. B: Struct. Sci.*, **1985**, 41, 383-390.

[Bayly1993] Bayly, C. I.; Cieplak, P.; Cornell, W. D.; Kollman, P. A. A Well-Behaved Electrostatic Potential Based Method Using Charge Restraints for Deriving Atomic Charges: The RESP Model *J. Phys. Chem.*, **1993**, 97, 10269-10280.

[Bentz1997] Bentz, D. L. 3-D Computer Simulation of Portland Cement Hydration and Microstructure Development *J. Am. Ceram. Soc.*, **1997**, 80, 3-21.

[Bishnoi2009] Bishnoi, S; Scrivener, K. L. μic: A new platform for modelling the hydration of cements *Cem. Concr. Res.*, **1995**, 25, 319-331.

[Brezovsky2013] Brezovsky, J.; Chovancova, E.; Gora, A.; Pavelka, A.; Biedermannova, L.; Damborsky, J. Software tools for identification, visualization and analysis of protein tunnels and channels *Biotechnol. Adv.*, **2013**, **31**, 38-49.

[Brown1984] Brown, P. W.; Liberman, L. O.; Frohnsdorff, G. Kinetics of the early hydration of tricalcium aluminate in solutions containing calcium-sulfate *J. Am. Ceram. Soc.*, **1984**, 67, 793-795.

[Bullard2007] Bullard, J. W. A 3-dimensional microstructural model of reactions and transport in aqueous mineral systems *Model. Simul. Mater. Sci. Eng.*, **2007**, 15, 711.

[Bullard2008] Bullard, J. W. A Determination of Hydration Mechanisms for Tricalcium Silicate Using a Kinetic Cellular Automaton Model *J. Am. Ceram. Soc.*, **2008**, 91, 2088-2097.

[Bullard2011] Bullard, J. W; Jennings, H. M.; Livingston, R. A. Nonat, A.; Scherer, G. W.; Schweitzer, J. S.; Scrivener, K. L.; Thomas, J. J. Mechanism of cement hydration *Cem. Concr. Res.*, **2011**, 41, 1208-1223.

[Collepardi1978] Collepardi, M.; Baldini, G.; Pauri, M.; Corradi, M. Tricalcium aluminate hydration in presence of lime, gypsum or sodium sulfate *Cem. Concr. Res.*, **1978**, 8, 571-580.

[Colville1972] Colville, A. A.; Geller, S. Crystal structures of $Ca_2Fe_{1.43}Al_{0.57}O_5$ and $Ca_2Fe_{1.28}Al_{0.72}O_5$ *Acta Crystallogr., Sect. B: Struct. Sci.*, **1972**, 28, 3196-3260.

[Conradt2004] Conradt, R. Chemical structure, medium range order, and crystalline reference state of multicomponent oxide liquids and glasses *J. Non-Cryst. Solids*, **2004**, 345&346, 16-23.

[Cornell1993] Cornell, W. D.; Cieplak, P.; Bayly, C. I.; Kollman, P. A. Application of RESP Charges To Calculate Conformational Energies, Hydrogen Bond Energies, and Free Energies of Solvation *J. Am. Chem. Soc.*, **1993**, 115, 9620-9631.

[Cornell1995] Cornell, W. D.; Cieplak, P.; Bayly, C. I.; Gould, I. R.; Merz, K. M. Jr.; Ferguson, D. M.; Spellmeyer, D. C.; Fox, T.; Caldwell, J. W.; Kollman, P. A. A Second Generation Force Field for the Simulation of Proteins, Nucleic Acids, and Organic Molecules *J. Am. Chem. Soc.*, **1995**, 117, 5179-5197.

[Cramer2002] Cramer, C. J. *Essentials of computationa chemistry: theories and models*, **2002**, Chichester, England.: John Wiley & Sons.

[Cygan2004] Cygan, R. T.; Liang, J. J.; Kalinichev, A. G. Molecular Models of Hydroxide, Oxyhydroxide, and Clay Phases and the Development of a General Force Field *J. Phys. Chem. B*, **2004**, 108, 1255-1266.

[DeGennes1987] De Gennes, P. G. Polymers at an interface; a simplified view *Adv. Colloid Interface Sci.*, **1987**, 27, 189-209.

[DeLaTorre2002] De La Torre, A. G.; Bruque, S.; Campo, J.; Aranda, M. A. G. The superstructure of C3S from synchrotron and neutron powder diffraction and its role in quantitative phase analyses *Cem. Concr. Res.*, **2002**, 32, 1347-1356.

[Ding1992] Ding, H. Q.; Karasawa, N.; Goddard III, W. A. Optimal spline cutoffs for Coulomb and van der Waals interactions *Chem. Phys. Lett.*, **1992**, 193, 197-201.

[Dolado2011] Dolado, J. S.; Van Breugel, K. Recent advances in modeling for cementitious materials *Cem. Concr. Comp.*, **2011**, *41*, 711-726.

[Duan2003] Duan, Y.; Wu, C; Chowdhury, S.; Lee, M. C.; Xiong, G.; Zhang, W.; Yang, R.; Cieplak, P.; Luo, R.; Lee, T.; Caldwell, J.; Wang, J.; Kollman, P. A Point-Charge Force Field for Molecular Mechanics Simulations of Proteins Based on Condensed-Phase Quantum Mechanical Calculations *J. Comput. Chem.*, **2003**, 24, 1999-2012.

[Durgun2012] Durgun, E.; Manzano, H.; Pellenq, R. J. M.; Grossman, J. C. Understanding and Controlling the Reactivity of the Calcium Silicate phases from First Principles *Chem. Mater.*, **2012**, *24*, 1262-1267.

[Durgun2014] Durgun, E.; Manzano, H.; Kumar, P. V.; Grossman, J. C. The Characterization, Stability, and Reactivity of Synthetic Calcium Silicate Surfaces from First Principles *J. Phys. Chem. C*, **2014**, 118, 15214-15219.

[Ercolessi1997] Ercolessi, F. *A MOLECULAR DYNAMICS PRIMER*, **1997**, ICTP, Trieste, http://www.fisica.uniud.it/~ercolessi/md/md/

[Feng1994] Feng, X.J.; Min, X. M.; Tao, C. X. Study on the structure and characteristics of dicalcium silicate with quantum chemistry calculations. *Cem. Concr. Res.*, **1994**, 24, 1311-1316.

[Ferrari2010] Ferrari, L.; J. Kaufmann, J.; Winnefeld, F.; Plank, J. Interaction of cement model systems with superplasticizers investigated by atomic force microscopy, zeta potential, and adsorption measurements *J. Colloid Interface Sci.*, **2010,** 347, 15-24.

[Ferrari2011] Ferrari, L.; J. Kaufmann, J.; Winnefeld, F.; Plank, J. Multi-method approach to study influence of superplasticizers on cement suspensions *Cem. Concr. Comp.*, **2011**, 41, 1058-1066.

[Flatt2009] Flatt, R. J.; Schober, I.; Raphael, E.; Plassard, C.; Lesniewska, E. Conformation of Adsorbed Comb Copolymer Dispersants *Langmuir*, **2009**, 25, 845-855.

[Fleishman2004] Fleishman, S.J.; Unger, V. M.; Yeager, M.; Ben-Tal, M. A C alpha model for the transmembrane alpha helices of gap junction intercellular channels *Mol. Cell.*, **2004**, 15, 879-888.

[Fluegel2009] Fluegel, A. Statistical regression modeling of glass properties - a tutorial *Glass. Technol.: Eur. J. Glass. Sci. Technol. A*, **2009**, 50, 1-22.

[Frenkel2001] Frenkel, D.; Smit, B. *Understanding molecular simulation : from algorithms to applications*, **2001**, San Diego: Academic Press, A division of Hancourt Inc.

[Fujii1974] Fujii, K; Kondo, W. Kinetics of hydration of tricalcium silicate *J. Am. Ceram. Soc.*, **1974**, 57, 492-497.

[Gaussian] Gaussian 03, Revision C.02, Frisch, M. J.; Trucks, G. W.; Schlegel, H. B.; Scuseria, G. E.; Robb, M. A.; Cheeseman, J. R.; Montgomery, Jr., J. A.; Vreven, T.; Kudin, K. N.; Burant, J. C.; Millam, J. M.; Iyengar, S. S.; Tomasi, J.; Barone, V.; Mennucci, B.; Cossi, M.; Scalmani, G.; Rega, N.; Petersson, G. A.; Nakatsuji, H.; Hada, M.; Ehara, M.; Toyota, K.; Fukuda, R.; Hasegawa, J.; Ishida, M.; Nakajima,

T.; Honda, Y.; Kitao, O.; Nakai, H.; Klene, M.; Li, X.; Knox, J. E.; Hratchian, H. P.; Cross, J. B.; Bakken, V.; Adamo, C.; Jaramillo, J.; Gomperts, R..

[Gay2001] Gay, C.; Raphaël, E. Comb-like polymers inside nanoscale pores *Adv. Colloid Interface Sci.*, **2001**, 94, 229-236.

[Giorgino2014] Giorgino, T. Computing 1-D atomic densities in macromolecular simulations: The density profile tool for VMD *Comput. Phys. Commun.*, **2014**, 185, 317-322.

[Havlica1993] Havlica, J.; Roztocka, D.; Sahu, S. Hydration kinetics of calcium aluminate phases in the presence of various ratios of $Ca^{2+}$ and $SO_4^{2-}$ ions in liquid phase *Cem. Concr. Res.*, **1993**, 23, 294-300.

[Hohenberg1964] Hohenberg, P; Kohn, W. Inhomogeneous electron gas *Physical Review B*, **1964**, 136, B864-&.

[Holly2006] Holly, R.; Peemoeller, H.; Zhang, M.; Reardon, E.; Hansson, C. M. Magnetic resonance in situ study of tricalcium aluminate hydration in the presence of gypsum *J. Am. Ceram. Soc.*, **2006**, 89, 1022-1027.

[Hoover1986] Hoover, W. G. *Molecular dynamics (Lecture notes in physics)*, **1986**, Berlin, New York: Springer-Verlag, vi, 138; Canonical dynamics: equilibrium phase space distributions *Phys. Rev. A,* **1985**, 31, 1695-1697.

[Hou2014] Hou, D.; Zhu, Y.; Lu, Y.; Li, Z. Mechanical properties of calcium silicate hydrate (C-S-H) at nano-scale: A molecular dynamics study *Mater. Chem. Phys.*, **2014**, 146, 503-511.

[Humphrey1996] Humphrey, W.; Dalke, A.; Schulten, K. VMD - Visual Molecular Dynamics *J. Mol. Graph.*, **1996**, 14, 33-38.

[Jefferey1952] Jeffery, J. W. The crystal structure of tricalcium silicate *Acta Crystallogr.*, **1952**, 5, 26-&.

[Jensen1999] Jensen, F. *Introduction to computational chemistry*, **1999**, Chichester ; New York: Wiley.

[Jensen2007] Jensen, F. *Introduction to computational chemistry*, 2nd ed, **2007**, Chichester, England ; Hoboken, NJ: John Wiley & Sons.

[Jorgensen1983] Jorgensen, W. L.; Chandrasekhar, J.; Madura, J. D.; Impey, R. W.; Klein, M. L. Comparison of simple potential functions for simulating liquid water *J. Chem. Phys.*, **1983**, 79(2), 926-935.

[Knauert2007] Knauert, S. T.; Douglas, J. F.; Starr, F. W. The Effect of Nanoparticle Shape on Polymer-Nanocomposite Rheology and Tensile Strength *J. Polym. Sci. Part B Polym. Phys.*, **2007**, 45, 1882-1897.

[Kumar2002] Kumar, S.; Nussinov, R. Salt Bridges Stability in Monomeric Proteins *Chem. Bio. Chem.,* **1999**, 293, 1241 - 1255.

[Kumar2002*] Kumar, S.; Nussinov, R. Relationship between Ion Pair Geometries and Electrostatic Strenths in Proteins *Biophys. J.*, **2002**, 83, 1595-1612.

[Kumar2002**] Kumar, S.; Nussinov, R. Close - Range Electrostatic Interactions in Proteins *ChemBioChem*, **2002**, 3, 604-617.

[Kwon2011] Kwon, T.; Harris, A. L.; Rossi, A.; Bargiello, T. A. Molecular Dynamics simulations of the Cx26 hemichannel: Evaluation of structural models with Brownian Dynamics *J. Gen. Physiol.*, **2011**, 138, 475-493.

[Lange2012] Lange, A.; Hirata, T.; Plank, J. The role of Non-Adsorbed PCE molecules in Cement Dispersion: Experimental Evidence for a New Dispersion Mechanism. In: Tenth International Conference on Superplasticizers and other Chemical Admixtures, American Concrete Institute SP 288, edited V. M. Malhotra. Prague, Czech Republic, **2012**.

[Leach2001] Leach, A. R. *Molecular Modelling - Principles and Applications - 2nd Ed.* **2001**, Pearson Education Limited.

[Lee1998] Lee, J. Y.; Baljon, A. R. C.; Loring, R. F.; Panagiotopoulos, A. Z. Simulation of polymer melt intercalation in layered nanocomposites, *J. Chem. Phys.*, **1998**, 109, 10321-10330.

[Levine1991] Levine, I. N. Quantum Chemistry, 1991, 4$^{th}$, Englewood Cliffs, N.J.: Prentice Hall.

[Li2005] Li, C. H.; Feng, N. H.; Li, Y. D.; Chen, R. J. Effects of polyethlene oxide chains on the performance of polycarboxylate-type water-reducers *Cem. Concr. Res.*, **2005**, 35, 867-873.

[Li2005] Li, C. H.; Feng, N. H.; Li, Y. D.; Chen, R. J. Effects of polyethlene oxide chains on the performance of polycarboxylate-type water-reducers *Cem. Concr. Res.*, **2005**, 35, 867-873.

[Liu2012] Liu, L.; Jaramillo-Botero, A.; Goddard III, W. A.; Sun, H. Development of a ReaxFF Reactive Force Field for Ettringite and Study of its Mechanical Failure Modes from Reactive Dynamics Simulations *J. Phys. Chem. A*, **2012**, *116*, 3918-3925.

[Locke2009] Locke, D; Bian, S.; Li, H. Harris, A. L. Post-translational modifications of connexin26 revealed by mass spectrometry *Biochem. J.*, **2009**, 424, 385-398.

[Maeda2009] Maeda, S.; Nakagawa, S.; Suga, M.; Yamashita, E.; Oshima, A., Fujiyoshi, Y.; Tsukihara, T. Structure of the connexin 26 gap junction channel at 3.5 Å resolution *Nature*, **2009**, 458 597-602.

[Mahasenan2002] Mahasenan, N.; Smith, S.; Humphreys, K. *The Cement Industry and Global Climate Change: Current and Potential Future Cement Industry $CO_2$ Emissions in Greenhouse gas control technologies. Proceedings of the 6th International Conference on Greenhouse Gas Control Technologies*, 1-4 October **2002**, Kyoto, Japan.

[Mayo1990] Mayo, S. L.; Olafson, B. D.; Goddard III, W. A. DREIDING: A Generic Force Field for Molecular simulations *J. Phys. Chem.*, **1990**, 94, 8897-8909.

[Manzano2009] Manzano, H. *Atomistic Simulation studies of the Cement Paste Components*, PhD Thesis, **2009**, Universidad del País Vasco.

[Manzano2011] Manzano, H.; Durgun, E.; Qomi, M. J. A., Ulm, F.; Pellenq, R. J. M., Grossman, J. C. Impact of the Chemical Impurities on the Crystalline Cement Clinker Phases determined by Atomistic Simulation *Cryst. Growth Des.*, **2011**, 11, 2964-2972.

[Marinho1984] Marinho, M. B.; Glasser, F. P. Polymorphism and phase changes in the ferrite phase of cements induced by titanium substitution *Cem. Concr. Res.*, **1984**, 14, 360-368.

[Martin2004] Martin, R. M. *Electronic Structure, basic theory and practical methods*, **2004**, Cambridge: Cambridge University Press.

[Martínez2009] Martínez, L.; Andrade, R.; Birgin, E. G.; Martínez, J. M. Packmol: A package for building initial configurations for molecular dynamics simulations *J. Comput. Chem.*, **2009**, 30, 2157-2164.

[Mayo1990] Mayo, S. L.; Olafson, B. D.; Goddard III, W. A. DREIDING: A Generic Force Field for Molecular simulations *J. Phys. Chem.*, **1990**, 94, 8897-8909.

[Minard2007] Minard, H.; Garrault, S.; Regnaud, L.; Nonat, A. Mechanisms and parameters controlling the tricalcium aluminate reactivity in the presence of gypsum *Cem. Concr. Res.*, **2007**, 37, 1418-1426.

[Mollah2000] Mollah, M. Y. H; Adams, W. J.; Schennach, R.; Cocke, D. L. A review of cement–superplasticizer interactions and their models *Adv. Cem. Res.*, **2000**, 12, 153-161.

[Mondal1975] Mondal, P; Jeffery, J. W. Crystal structure of tricalcium aluminate $Ca_3Al_2O_6$ *Acta Crystallogr., Sect. B: Struct. Sci.*, **1975**, 31, 8-&.

[Moranville1992] Moranville-Regourd, M.; Boikova, A. I. Chemistry, structure, properties and quality of clinker. in 9th International Congress on the Chemistry of Cement, **1992**, New Delhi.

[Mumme1995] Mumme, W. G. Crystal structure of tricalcium silicate from a Portland cement clinker and its application to quantitative XRD analysis *Neues Jahrb. Mineral.* **1995**, 4, 145-160.

[Nelson1990] Nelson, E. B. *Well Cementing*, **1990**, Houston, Texas: Schlumberger Educational Services

[Nishi1984] Nishi, F.; Takeuchi, Y. The rhombohedral structure of tricalcium silicate at 1200ºC *Z. Kristallogr.*, **1984**, 168, 197-212.

[Nishi1985] Nishi, F.; Takeuchi, Y; Maki, I. Tricalcium silicate $Ca_3O(SiO_4)$: the monoclinic superestructure *Z. Kristallogr.*, **1985**, 172, 297-314.

[Odler1979] Odler, I; Dorr, H. Early hydration of tricalcium silicate. 1. Kinetics of the hydration process and the stoichoimetry of the hydration products *Cem. Concr. Res.*, **1979**, 9, 239-248; Early hydration of tricalcium silicate. 2. Induction period. *Cem. Concr. Res.*, **1979**, 9, 277-284.

[Oshima2007] Oshima, A.; Tani, K.; Hiroaki, Y.; Fujiyoshi, Y.; Sosinsky, G. E. Three-dimensional structure of a human connexin26 gap junction channel reveals a plug in the vestibule *Proc. Natl. Acad. Sci. USA*, **2007**, 104, 10034-10039.

[Parrot1984] Parrot, L. J.; Killoh, D. C. Prediction of cement hydration, *Brit. Ceram. Proc.*, **1984**, 35, 41-53.

[Pellenq2009] Pellenq, R. J. M.; Kushima, A.; Shahsavari, R.; Van Vliet, K. J.; Buehler, M. J.; Yip, S.; Ulm, F. J. A realistic molecular model of cement hydrates *Proc. Natl. Acad. Sci. U.S.A.*, **2009**, 106, 16102-16107.

[Perdew1986] Perdew, J. P.; Ernzerhof, M. Burke, K. Rationale for mixing exact exchange with density functional approximations *J. Chem. Phys.*, **1986**, 105, 9982-9985.

[Peterson2006] Peterson, V. K.; Neumann, D. A.; Livingston, R. A. Hydration of cement: The application of quasielastic and inelastic neutron scattering. Physica B: Cond. Matter, **2006**, 385, 481-486.

[Plank2008] Plank, J.; Pöllmann, K.; Zouaoui, N.; Andres, P. R.; Schaefer, C. Synthesis and performance of methacrylic ester based polycarboxylate

superplasticizers possessing hydroxy terminated poly(ethylene glycol) side chains *Cem. Concr. Res.*, **2008**, 38, 1210-1216.

[Plimpton1995] Plimpton, S. Fast Parallel Algorithms for Short-Range Molecular Dynamics *J. Comput. Phys.*, **1995**, 117, 1-19.

[Priven2004] Priven, A. I. General method for calculating the properties of oxide glasses and glass forming melts from their composition and temperature *Glass. Technol.*, **2004**, 45, 244-54.

[Ramachandran1997] Ramachandran, V. S. *Concrete Admixtures Handbook: Properties, Science and Technology*, II Ed., **1997**, Park Ridge, New Jersey, U.S.A., Noyes Publications.

[Rapaport1995] Rapaport, D. C. *The art of molecular dynamics simulation*, **1995**, Cambridge, New York: Cambridge University Press.

[Richardson1992] Richardson, I. G.; Groves, G. W. Models for the composition and structure of calcium silicate hydrate (C-S-H) gel in hardened tricalcium silicate pastes *Cem. Concr. Res.*, **1992**, 22, 1001-1010.

[Richardson1993] Richardson, I. G.; Groves, G. W. Micro structure and micro analysis of hardened ordinary portland cement pastes *J. Mater. Sci.*, **1993**, 28, 265-277.

[Richardson2000] Richardson, I. G. The nature of the hydration products in hardened cement pastes *Cem. Concr. Compos.*, **2000**, 22, 97-113.

[Richardson2004] Richardson, I. G. , Tobermorite/jennite- and tobermorite/calcium hydroxidebased models for the structure of C-S-H: applicability to hardened pastes of tricalcium silicate, beta-dicalcium silicate, Portland cement, and blends of Portland cement with blast-fumace slag, metakaolin, or silica fume *Cem. Concr. Res.*, **2004**, 34, 1733-1777.

[Ridi2012] Ridi, F.; Fratini, E.; Luciani, P.; Winnefeld, F.; Baglioni, P. Tricalcium Silicate Hydration Reaction in the Presence of Comb-Shaped Superplasticizers: Boundary Nucleation and Growth Model Applied to Polymer-Modified Pastes *J. Phys. Chem. C*, **2012**, 116, 10887−10895.

[Roothaan1951] Roothaan, C. C. J. New developements in molecular orbital theory *Rev. Mod. Phys.*, **1951**, 23, 69-89.

[Ryckaert1977] Ryckaert, J. P.; Ciccotti, G.; Berendsen, H. J. C. Numerical Integration of the Cartesian Equations of Motion of a System with constraints: Molecular Dynamics of n-alkanes *J. Comput. Phys.*, **1977**, 23, 327-341.

[Sanchez2008] Sanchez, F.; Zhang, L. Molecular dynamics modeling of the interface between surface functionalized graphitic structures and calcium–silicate–hydrate: Interaction energies, structure, and dynamics *J. Colloid Interface Sci.*, **2008,** 323, 349-358.

[Scherer2014] Scherer, G. W.; Zhang, J.; Thomas, J. J. Nucleation and growth models for hydration of cement *Cem. Concr. Res.*, **2012**, 17, 982-993.

[Schlick2010] Schlick, T. Molecular Modeling and Simulation, 2nd Ed., **2010**, Springer Science+Business Media, LLC.

[Seppälä2013] Seppälä, A. *Molecular dynamics of the absorption of water into the interlayers of Na-montmorillonite*, Master's Thesis, **2013**, University of Helsinki.

[Shahsavari2011] Shahsavari, R.; Pellenq, R. J. M.; Ulm, F. J. Empirical force fields for complex hydrated calcio-silicate layered materials *Phys. Chem. Chem. Phys.*, **2011**, 13, 1002-1011.

[Smart1996] Smart, O. S.; Neduvelil, J. G.; Wang, X.; Wallace, B. A.; Sansom, M. S. P. HOLE: A program for the analysis of the pore dimensions of ion channel structural models *J. Mol. Graph.*, **1996**, 14, 354-360.

[Smith1965] Smith, D. K.; Majumdar, A.; Ordway, F. Crystal structure of $\gamma$-$C_2S$ *Acta Crystallogr.*, **1965**, 18, 787-&.

[Steele1929] Steele, F. A.; Davey, W. P. The crystal structure of tricalcium aluminate *J. Am. Chem. Soc.*, **1929**, 51, 8, 2283-2293.

[Stendardo2010] Stendardo, E.; Pedone, A.; Cimino, P.; Menziani, M. C.; Crescenzi, O.; Barone, V. Extension of the AMBER force-field for the study of large nitroxides in condensed phases: an *ab initio* parameterization *Phys. Chem. Chem. Phys.*, **2010**, 12, 11697-11709.

[Stephan2006] Stephan, D.; Wistuba, S. Crystal structure refinement and hydration behaviour of doped tricalcium aluminate *Cem. Concr. Res.*, **2006**, 36, 2011-2020.

[Sujata1992] Sujata, K.; Jennings, H. M. Formation of a protective layer during the hydration of cement *J. Am. Ceram. Soc.*, **1992**, 75, 1669-1673.

[Suter2009] Suter, J. L.; Anderson, R. L; Greenwell, H. C.; Coveney, P. V. Recent advances in large-scale atomistic and coarse-grained molecular dynamics simulation of clay minerals *J. Mater. Chem.*, **2009**, 19, 2482-2493.

[Takeuchi1980] Takeuchi, Y.; Nishi, F.; Maki, I. Crystal-chemical characterization of the $3CaO$-$Al_2O_3$-$Na_2O$ solid solution series *Z. Kristallogr.*, **1980**, 152, 259-307.

[Taylor1986] Taylor, H. F. W. Proposed structure for calcium silicate hydrate gel *J. Am. Ceram. Soc.*, **1986**, 69, 464-467.

[Taylor1990] Taylor, H. F. *Cement Chemistry 1 ed.*, **1997**, London: Thomas Telford Publishing.

[Thomas1981] Thomas, N.L. and D.D. Double, Calcium and silicon concentrations in solution during the early hydration of portland cement and tricalcium silicate *Cem. Concr. Res.*, **1981**, 11, 675-687.

[Thomas2007] Thomas, J. J. A New Approach to Modeling the Nucleation and Growth Kinetics of Tricalcium Silicate Hydration *J. Am. Ceram. Soc.*, **2007**, 90, 3282-3288.

[Thomas2011] Thomas, J. J.; Biernacki, J. J.; Bullard, J. W.; Bishnoi, S.; Dolado, J. S.; Scherer, G. W; Luttge, A. Modeling and simulation of cement hydration kinetics and microstructure development *Cem. Concr. Comp.*, **2011**, *41*, 1257-1278.

[Unger1999] Unger, V. M.; Kumar, N. M.; Gilula, N. B.; Yeager., M. Three-dimensional structure of a recombinant gap junction membrane channel *Science*, **1999**, 283, 1176-1180.

[Valentini2014] Valentini, L; Parisatto, M.; Russo, V.; Ferrari, G.; Bullard, J. W.; Angel, R. J.; Dalconi, M. C.; Artioli, G. Simulation of the hydration kinetics and elastic moduli of cement mortars by microstructural modelling *Cem. Concr. Comp.*, **2014**, 52, 54-63.

[vanBreugel1995] van Breugel, K. Numerical simulation of hydration and microstructural development in hardening cement-based materials (I) theory *Cem. Concr. Res.*, **1995**, 25, 319-331.

[vanOss2011] van Oss, H. G. U.S. Geological Survey, Mineral Commodity Summaries, **2011**, http://minerals.usgs.gov/minerals/pubs/commodity/cement/mcs-2011-cemen.pdf

[Verlet1967] Verlet, L. Computer experiments on classical fluids. I. Thermodynamical properties of lennard-jones molecules *Phys. Rev.*, **1967**, 159, 98.

[Wang2000] Wang, J.; Cieplak, P.; Kollman, P. A. How Well Does a Restrained Electrostatic Potential (RESP) Model Perform in Calculating Conformational Energies of Organic and Biological Molecules? *J. Comput. Chem.*, **2000**, 12, 1049-1074.

[Weiner1984] Weiner, S. J.; Kollman, P. A.; Case, D. A.; Singh, U. C.; Ghio, C.; Alagona, G.; Profeta, S.; Weiner, J; Winer, P. A New Force Field for Molecular

Mechanical Simulation of Nucleic Acids and Proteins *J. Am. Chem. Soc.*, **1984**, 106, 765-784.

[Shahsavari2009] Wick, C. D.; Dang, L. X. Investigating Hydroxide Anion Interfacial Activity by Classical and Multistate Empirical Valence Bond Molecular Dynamics Simulations *J. Phys. Chem.*, **2009**, 113, 6356-6364.

[Winnefeld2007] Winnefeld, F.; Becker, S.; Pakusch, J.; T. Götz, T. Effects of the molecular architecture of comb-shaped superplasticizers on their performance in cementitious systems *Cem. Concr. Comp.*, **2007**, 29, 251-262.

[Wu2011] Wu, W.; Al-Ostaz, A.; Cheng, A. H. D.; Song, C. R. Computation of Elastic Properties of Portland Cement Using Molecular Dynamics *J. Nanomech. Micromech.*, **2011**, *1*, 84-90.

[Yoon2013] Yoon, S.; Monteiro, P. J. M. Molecular Dynamics Study of Water Molecules in Interlayer of 14 Å Tobermorite *J. Adv. Concrete Tech.*, **2013**, *11*, 180-188.

[Young1972] Young, J. F. A review of the mechanism s of set-retardation in Portland cement pastes containing organic admixtures *Cem. Concr. Res.*, **1972**, 2, 415-433.

[Zonta2012] Zonta, F.; Polles, G.; Zanotti, G.; Mammano, F. Permeation Pathway of Homomeric Connexin 26 and Connexin 30 Channels Investigated by Molecular Dynamics *J. Biomol. Struct. Dyn.*, **2002**, 29, 985-998.

[Zonta2013] Zonta, F.; Polles, G.; Sanasi, M. F.; Bortolozzi, M.; Mammano, F. The 3.5 Å X−ray structure of the human connexin26 gap junction channel is unlikely that of a fully open channel *Cell. Commun. Signal.*, **2013**, 11, 15**.**

[Zonta2014] Zonta, F.; Mammano, F.; Torsello, M.; Fortunati, N.; Orian, L.; Polimeno, A. Role of gamma carboxylated Glu47 in connexin 26 hemichannel regulation by extracellular $Ca^{2+}$: Insight from local quantum chemistry study *Biochem. Biophys. Res. Commun.*, **2014**, 445, 10-15.

[Zonta2014*] Zonta, F.; Buratto, D.; Cassini, C.; Bortolozzi, M.; Mammano, F. Molecular dynamics simulations highlight structural and functional alterations in deafness–related M34T mutation of connexin 26 *Front. Physiol.*, **2014**, 5, 85, 1-9.

[Zonta2015] Zonta, F.; Girotto, G.; Buratto, D.; Crispino, G.; Morgan, A.; Abdulhadi, K.; Alkowari, M.; Badii, R.; Gasparini, P.; Mammano, F. The p.Cys169Tyr variant of connexin 26 is not a polymorphism *Hum. Mol. Gen.*, **2015**, 24, 2641-2648.

[Zingg2008] Zingg, A.; Winnefeld, F.; Holzer, L.; Pakusch, J.; Becker, S.; Gauckler, L. Adsorption of polyelectrolytes and its influence on the rheology, zeta potential, and microstructure of various cement and hydrate phases *J. Colloid Interface Sci.*, **2008**, 323, 301-312.

[Zingg2009] Zingg, A.; Winnefeld, F.; Holzer, L.; Pakusch, J.; Becker, S.; Gauckler, L.; Figi, R.; Gauckler, L. Interaction of polycarboxylate-based superplasticizers with cements containing different $C_3A$ amounts *Cem. Concr. Comp.*, **2009**, *31*, 153-162.

**Acknowledgments**

*Firstly I would like to thanks my Supervisor, Prof. Antonino Polimeno, for his support during all my PhD.*

*I would to thank Prof. Gilberto Artioli, Luca Valentini, their research group CIRCe at the Dipartimento di Geoscienze, Vincenzo Russo and Giorgio Ferrari of Mapei Spa Staff for their strong expertise in the field of PCE superplasticizers and for the pretty stimulating experience in Beijing.*

*A special thank to Dr. Laura Orian for the wonderful collaboration work, for the coffees and for the common passion for the mountains.*

*My thanks to all my friends and colleagues of Theoretical Chemistry Group, Mirco and Paolo, and in particular Mauro, Maurizio and Marco, my fellow PhDs, for all funny moments.*

*I say thank you to ing. Gianpietro Sella for his great support with all C3P high performance computing facility of DISC.*

*Finally, I would like to thank the people dearest to me: my parents, Morena and Roberto, and my girl friend Francesca, to whom this work is dedicated.*